REVIEW

Check for updates

Optoelectronic MXene quantum dots: frontiers in sensor technology for next-generation diagnostics and environmental monitoring

Ankur Singh, [ID] [a] Supratim Mahapatra, [ID] [a] Rajendra Prasad, [ID] [b] Sumit Kumar Singh [ID] [c] and Pranjal Chandra [ID] *[a]

MXene QDs have garnered the attention of established as well as budding researchers as a new class of nanomaterial due to their exceptional properties and wide applicability. Advancements in nanotechnology and materials science have led the discovery of these, and explorations of their exceptional physico-chemical characteristics have positioned them as a cutting-edge nanomaterial with immense potential for future innovation. This review explores the different aspects of MXene QDs, including fundamentals, functionalization, and the doping of precursors. The unique properties, including structural, electronic, optical properties, and biocompatibility, making these promising candidates for use in optoelectronic devices have been thoroughly discussed. The different methods used to formulate MXene QDs into functional versions, including ball milling, pyrolysis, molten salt, hydrothermal, and solvothermal synthesis, and ultrasonication have been elaborated on with suitable examples. This article also includes precise yet insightful discussion on the MXene-QD-based sensing of different molecular categories, *viz.* small molecules, macromolecules, and environmental pollutants. Additionally, this paper provides insightful discussion on sensor fabrication strategies, limits of detection (LODs), linear detection ranges (LDRs), synthetic routes, and real sample detection, along with the detection techniques involved in sensor development in various studies. This article brings fundamental insights ranging from the synthesis of MXene QDs to their deployment to real-time applications in order to understand the overall research scope along with translational bottlenecks from the perspective of future development.

[a]Laboratory of Bio-Physio Sensors and Nano bioengineering, School of Biochemical Engineering, Indian Institute of Technology (BHU) Varanasi, Uttar Pradesh 221005, India
[b]Interventational Theranostics & Molecular Imaging Lab, School of Biochemical Engineering, Indian Institute of Technology (BHU) Varanasi, Uttar Pradesh 221005, India
[c]Laboratory of Engineered Therapeutics, School of Biochemical Engineering, Indian Institute of Technology (BHU) Varanasi, Uttar Pradesh 221005, India

1. Introduction

In nanoscience, the prefix 'nano' comes from a Greek word that means 'dwarf' or something very tiny, and these materials have been deployed as sensing probes in miniaturized platforms.[1,2] The Nobel laureate and American physicist Richard Phillips Feynman laid down the concept of nanotechnology in 1959 and is known as the father of nanotechnology.[3,4] In 1974 a Japanese scientist Norio Taniguchi coined the term and defined nanotechnology.[5] After Feynman and Taniguchi, nanotechnology attracted the attention of other researchers which enabled a plethora of possibili-
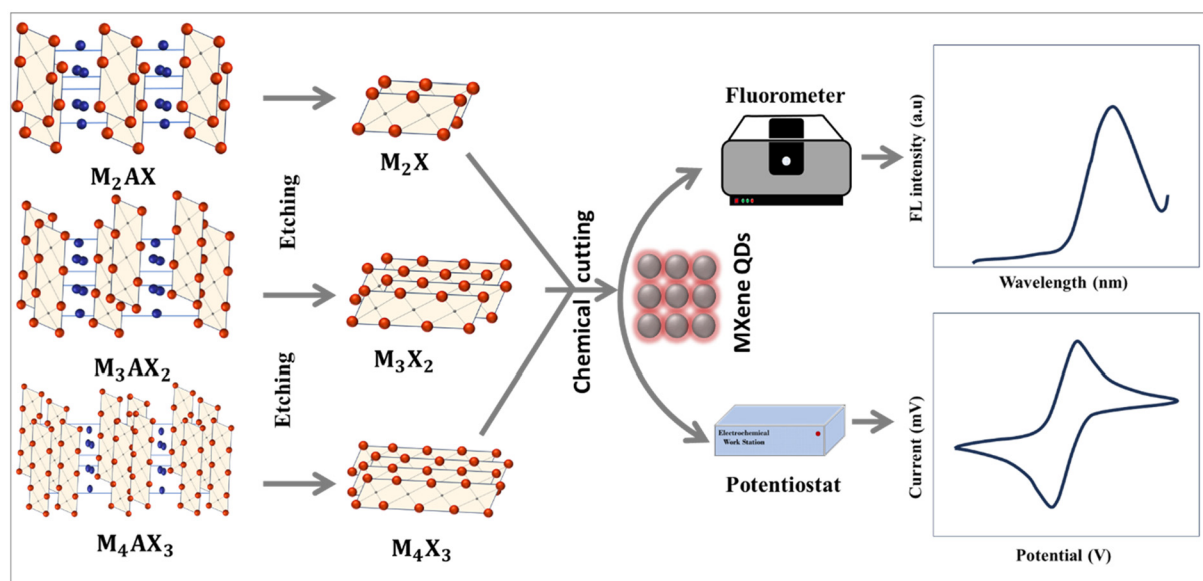
ties for the exploration of newer nanomaterials for a wide range of applications. Recent advancements in nanoscience and nanotechnology replaced bulk materials with powerful and efficient nanoconfined materials comprising 0D, 1D, 2D, and 3D morphology. Due to their superior physicochemical properties over bulk materials, they were deployed as bioelectronic interfaces for miniaturized diagnostics setups. Nanoconfined 0D materials, also described as quantum dots, were introduced by Alexei Ekimov during the late 1970s to early 1980s while working on copper chloride nanocrystals. A further milestone in the wet chemistry of QDs emerged in 1993 when Christopher Murray, David Norris, and Moungi Bawendi published ground-breaking findings following the established concept of Michael L. Steigerwald. This attracted attention after the 2023 Nobel Prize in Chemistry was awarded for QD research, exhilarating the colloidal science community worldwide.[6,7]

Bio-electronic interfaces, robotic prostheses, and sensors are predicted to undergo booming development in the upcoming years, affecting societal and human health. The discovery of graphene in 2006 and its diverse range of applications led

Scheme 1 A general schematic representation of MXene QD synthesis and their deployment in sensing. A potentiostat device is used for electrochemical measurements and a fluorometer is used for FL measurements.

to a tremendously upsurge in the exploration of newer 2D material to meet future needs.[8] In 2011 the Gogotsi group synthesized MXene as a new class of 2D metal carbides/nitrides/carbonitrides from the MAX phase.[9] Here, "M" symbolizes a transition metal, offering the intriguing advantage of an array of choices for the element, including titanium (Ti), vanadium (V), chromium (Cr), yttrium (Y), zirconium (Zr), niobium (Nb), molybdenum (Mo), hafnium (Hf), tantalum (Ta), and tungsten (W). The "A" symbolizes the IIIA/IVA group elements, of which each one has its own unique chemistry and properties in the MAX phase.[10] Finally, "X" symbolizes C and/or N.[11] A MXene is represented by the general formula $M_{n+1}X_nT_x$ (n = 1–3, T_x represents surface termination group such as –O, –F, and –OH).[12] The wide elemental choice has led to the foundation of different categories of MXene, including M_4C_3 ($V_4C_3T_x$), M_3C_2 ($Ti_3C_2T_x$), M_2C (V_2CT_x), M_4N_3 ($Ti_4N_3T_x$), M_2N (Nb_2NT_x), M_3CN (Ti_3CNT_x), and M_2CN (Nb_2CNT_x).[13,14] In addition, these researchers have explored double transition metal MXenes such as $Mo_2TiC_2T_x$ and $Cr_2TiC_2T_x$, enabling enhanced optoelectronic properties. This new class of 2D materials has widely been employed in various fields, including supercapacitors, catalysis, biomedicine, and sensor development, due to the unique physical and chemical properties, such as conductivity, hydrophilicity, photothermal stability, and tunable surface properties (Scheme 1). Layered materials (like 2D MXenes) have very unique features, being able to lodge various ions and molecules in their interlayer microenvironment; this phenomenon is described as intercalation. The electrochemical intercalation of Li ions was carried out by Naguib *et al.* in a newly explored 2D Ti_2C MXene, which had an oxidized surface after carrying out Al (aluminum) etching using HF from Ti_2AlC.[15] After Gogotsi's remarkable contribution, the MAX phase opened a newer route for QD synthesis

and applications. MXene QDs (0D) derived from a MXene block (2D) were synthesized for the first time by Xue and coworkers in 2017 and explored as an optoelectronic interface for sensor development.[16] This serves as an effective link between biology and optoelectronics in terms of the overall performance and unique electronic and optical properties. Compared to a MXene block, these QDs offer a high specific surface area, more tunable surface properties, better hybridization abilities, good biocompatibility, and a bigger window for doping or functionalization.[17] Quantum confinement and edge effects further add unique electronic, optical, and fluorescence properties, which make MXene QDs superior to their parent 2D MXene blocks.[18] Due to their high dielectric constants and extinction coefficients, MXene QDs can be easily separated into electrons and holes.[19] Edge and confinement effects also add excellent light-quenching properties, which enable the conversion of light to heat.[20,21] The cytotoxicity of MXene QDs is very much lower than the parent material so they are more biocompatible compared to other more cytotoxic materials like MXene 2D nanosheets.[22,23] Recently Lim *et al.* provided a summary report on the cytotoxicity of MXene-based materials, presenting MXene QDs as less cytotoxic compared with other nanomaterials.[24] Another study by Lin *et al.* proposed less phototoxic MXene-derived nanomaterials intended for the *in vivo* treatment of tumors.[25] MXene QDs also harbor tunable photoluminescence (PL), size dependence and long-term stability, opening up broader prospects for optical-based sensing applications.[26,27] Looking to the 21st century, the world is witnessing a population of more than 8 billion, placing immense pressure on health care systems, the provision of clean air, water, food safety and security, and energy infrastructure, which all ultimately impact human health. To overcome such challenges, researchers are continuously

exploring MXene QDs for a diverse range of applications, including next-generation diagnostics. The unique properties of MXene QDs make them promising candidates for deployment in electrochemiluminescence (ECL), photoluminescence (PL), and fluorescence (FL) sensors. A typical biosensor comprises an analyte, sensor matrix, biorecognition element, transducer, amplifier, processor, and, finally, a digital output.

Fig. 1 illustrates the publication trend for "MXene quantum dot-based sensors" retrieved from the online database "Scopus". The upward trajectory highlights the growing interest in this emerging class of zero-dimensional nanomaterials, showing an apparent need for a comprehensive and integrative review that offers an in-depth perspective on MXene QDs, particularly from an optoelectronic material interface standpoint. Despite the tremendous exploration of MXene QDs with unique properties, critical holistic consolidations of advancements remain scarce. There have been numerous recent individual studies and brief reviews that have explored MXene QDs from the perspective of sensors. They often addressed these QDs both in isolation and under the broader umbrella category of QDs. There are a few recent brief reviews highlighting MXene QDs in detail; however, there is an immense research gap to be bridged regarding a holistic understanding of MXene QDs as optoelectronic interfaces.[28,29] This manuscript covers synthesis, distinctive properties, and integration into next-generation diagnostics for the detection of clinically and environmentally significant molecules. Another key gap lies in the lack of in-depth analysis of synthesis–property–function correlation. We have tried to present a focused article introducing not only consolidated resources but also a new framework for understanding this area from an optoelectronics perspective. Additionally, future research directions and existing limit-ations are discussed in detail to stimulate further advancements in this field.

The research interest in MXene QDs has increased significantly and continues to grow due to their unique physico-chemical properties, enabling a wide scope. The optical, electronic, and catalytic properties of MXene quantum dots are significantly influenced by several factors, including functional groups, size, and dopants. The precise adjustment of these factors is crucial for achieving MXene QDs with the desired properties for effective application. Nanosheets derived from the MAX phase can be further employed in the synthesis of MXene QDs, retaining a significant number of terminal functional groups from their parent counterparts.[30] These nanosheets can be rapidly oxidized and degraded upon exposure to air and/or water in a few days, leading to the formation of metal oxides and carbon on the surface.[31,32] Therefore, tuning the surface will improve the stability of the produced MXene QDs with enhanced selectivity, biocompatibility, and catalytic properties.[33,34] The selection of appropriate tuning agents is a crucial step in the synthesis of MXene QDs with desired properties having improved performance.[35] The doping of MXene QDs also helps to improve the properties that enable the wide-ranging applications comprehensively discussed in below.[36,37]

Carbide-, nitride-, or carbonitride-derived MXene QDs without any other contributing chemicals are described as pure MXene QDs. These pure forms do not meet the advanced practical needs for modern sensitive miniaturized deployable sensing probes.[38] Therefore, heteroatom doping is considered as an effective and versatile approach that improves both the chemical and physical properties of the obtained QDs for their real-world application.[39,40] It also affects the intrinsic properties of nanomaterials, like the optical and electronic properties, including surface and local chemistry.[41] The selection of appropriate doping agents is crucial for the synthesis of MXene QDs with the desired properties, and this wide window of tuneability opens further scope for the advancement of next-generation optoelectronic devices. Various doping agents were used to dope MXene QDs for the desired applications. A study by Gou et al. developed nitrogen-doped MXene QDs that showed very high antioxidizing properties due to their ability to react with strong oxidizers.[42] It revealed that doping with electron-rich functional groups facilitates strong antioxidant abilities. Another study by Rajapriya et al. reported nitrogen-doped MXene QDs obtained through a hydrothermal synthetic route that harbor unique physicochemical properties and were deployed for dopamine sensing.[43]

Global challenges, such as the burden of emerging diseases, antibiotic resistance, and environmental pollution, have created a growing niche for highly selective, sensitive, miniaturized platforms.[44] Here, sensor technology is playing a pivotal role in next-generation disease diagnosis and environmental monitoring, enabling the accurate, rapid, and real-time detection of a diverse range of biological and environmentally important molecules.[45] Owing to their tunable and excellent optoelectronic properties, MXene QDs have been used in
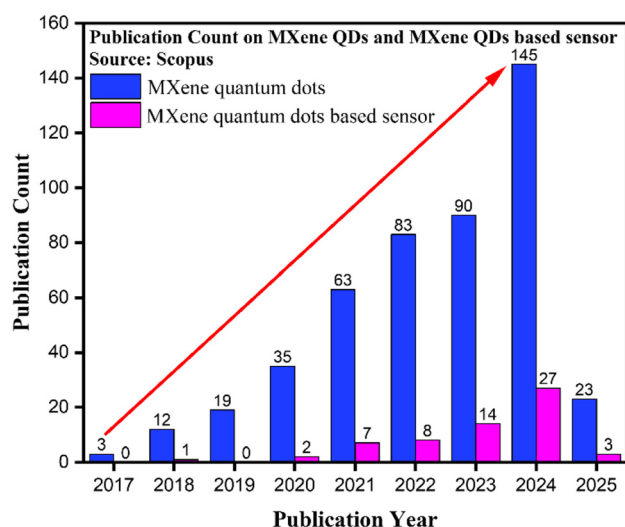

Fig. 1 A graphical representation of recently published research on MXene quantum dots and MXene quantum dot-based sensors, as per the online database "Scopus" using the keywords MXene quantum dots and MXene quantum dots-based sensor (as accessed on 10.01.2025).

sensor probes, enabling ultra-low LODs covering the clinically relevant range, allowing multiplex analysis of complex biological matrices, and showing robust performance in real-world conditions.[46–48] Recently Mohkam *et al.* summarized the potential and safety of MXene QDs for the diagnosis of allergies.[49] Nanosized MXene QDs, which are responsible for useful optical and electronic properties, can also lead to high surface energy and high surface-to-volume ratios, and these may affect the aggregation.[50,51] The fabrication of MXene QDs combined with other nanomaterials can enhance the optoelectronic properties and stability, opening up further scope for advanced diagnostics.[52] A study by Guo *et al.* reported a nanocomposite structure comprising MXene QDs and nickel in a flower-like hybrid material, which exhibited outstanding catalytic properties and was employed for chromium ion reduction.[53] Another study by Cheng *et al.* reported a nanocomposite comprised of MXene QDs and copper that exhibited synergistically enhanced electrocatalytic nitrogen reduction activity compared to pure MXene QDs.[54] These chemical tuning methods play a pivotal role in MXene QD functionalization for desired applications. The functionalization of QDs is carried out at different stages, depending on the synthetic route, tuning agents, and intended applications. Exceptional electrical conductivity, optical characteristics, rich surface chemistry/terminations, tunable functional groups, intrinsic hydrophilicity, and superior biocompatibility make these superior candidates compared with the other nanomaterials such as carbon QDs and metallic nanoparticles.[55] Based on the starting materials, the mechanisms of MXene QD synthesis can be classified into different categories of which a few important ones are described here. These include ball milling, pyrolysis, molten salt, hydrothermal, and solvothermal synthesis, and ultrasonication methods, which are comprehensively discussed below.

2. Methods of MXene QD synthesis

The method of MXene QD synthesis is a very crucial factor that plays an important role in determining size, thickness, and the edge configuration of QDs.[56,57] In this overall synthesis procedure for these QDs, the starting material, *viz.* the MAX phase—a unique class of layered ternary carbide, nitride, and carbonitride, plays a very important role. Researchers have explored different synthetic routes for MAX phase incorporation, including high-temperature synthesis, spark plasma sintering, hot isostatic pressing, and self-propagating high-temperature synthesis.[58] High-temperature synthesis from binary compounds or element precursors is common due to its low-cost, simplicity, and scalability. A study by Zhou *et al.* developed a MAX phase from precursors, elemental powder of Ti, activated C, and Al, and then densified the mixture by a spark plasma sintering process at a temperature of 1250 °C and under pressure of 22 MPa.[59] In another report, Gao *et al.* prepared the MAX phase Ti_3AlC_2 by the *in situ* reaction of precursors of Ti–Al–C through a sintering method, as illustrated in Fig. 2(I).[60] A study by Wang *et al.* proposed a solid–liquid reac-

tion followed by simultaneous *in situ* hot pressing for Ti_3AlC_2 MAX phase synthesis, exhibiting a sheet-like structure and polycrystalline nature.[61] A different study by Deysher *et al.* proposed novel Mo_4VAlC_4 MAX phase synthesis through self-propagation at a high temperature of 1650 °C.[62]

Following the synthesis of the MAX phase precursor, it is treated with an etching agent (*ex situ* or *in situ*) to remove the sandwiched "A" element, leading to the formation of multilayer accordion-like 2D MXene nanosheets. In an *ex situ* etching process, highly concentrated HF is directly used in a chemical treatment, while in an *in situ* etching process HF is formed during the chemical reaction, and this is involved in the etching of Al from the MAX phase. After this delamination process was carried out, the multilayered structure was dispersed into few-layered nanosheets by employing suitable organic solvents. A study by Zong *et al.* proposed the synthesis of Ti_2NT_x coupled with N-MoSe$_2$ for efficient water splitting.[64] The etching and exfoliation of the MXene precursors is depicted in Fig. 2(IIb), while Fig. 2(IIc) shows the delamination of multilayered MXenes into few- or single-layer $Ti_3C_2T_x$ sheets, emphasizing their two-dimensional morphology and terminal functional groups. Alternatively, few-layered nanosheets can be utilized for MXene QD synthesis through a chemical cutting route. Chemical cutting can be done through hydrothermal, solvothermal, or microwave-assisted methods. In the above approach, 3D bulk materials were etched, delaminated and/or exfoliated into few-layered 2D nanosheets and then further fragmentized into smaller 0D quantum dots.[65,66] In this section, we comprehensively discuss the following methods: ball milling, pyrolysis, molten salt, hydrothermal, and solvothermal synthesis, and ultrasonication, covering suitable examples and translational bottlenecks.

2.1. Ball milling

Ball milling is a cost-effective, scalable, and mechanical approach used to produce MXene QDs.[67,68] It involves using mechanical force to break down bulk material through exfoliation and fragmentation into nanoscale QDs with desirable characteristics.[66] It is employed for downsizing the MAX phase from multilayered to few-layered nanosheets. In addition, mechanical forces produced during the collision of the grinding balls progressively downsize the lateral dimensions and thickness of the 2D sheets, producing 0D MXene QDs.[69,70] It may be carried out using a solvent that acts as a mild etchant, like HF, to achieve peeling effects which facilitate exfoliation and lead to the formation of "accordion"-like 2D sheets. Here, the milling time and speed play crucial roles in determining the size and functionality. A higher speed and prolonged exposure can enhance energy transfer and accelerate the fragmentation of layered sheets into finer QDs. However, the use of an excessive milling speed and time may cause structural damage or aggregation. A study by Zhang *et al.* reported MXene QD synthesis through a ball-milling synthesis route, and employed them as an anode material for sodium-ion batteries; this high-energy ball milling not only downsized the lateral dimensions but also introduced edge defects, as shown
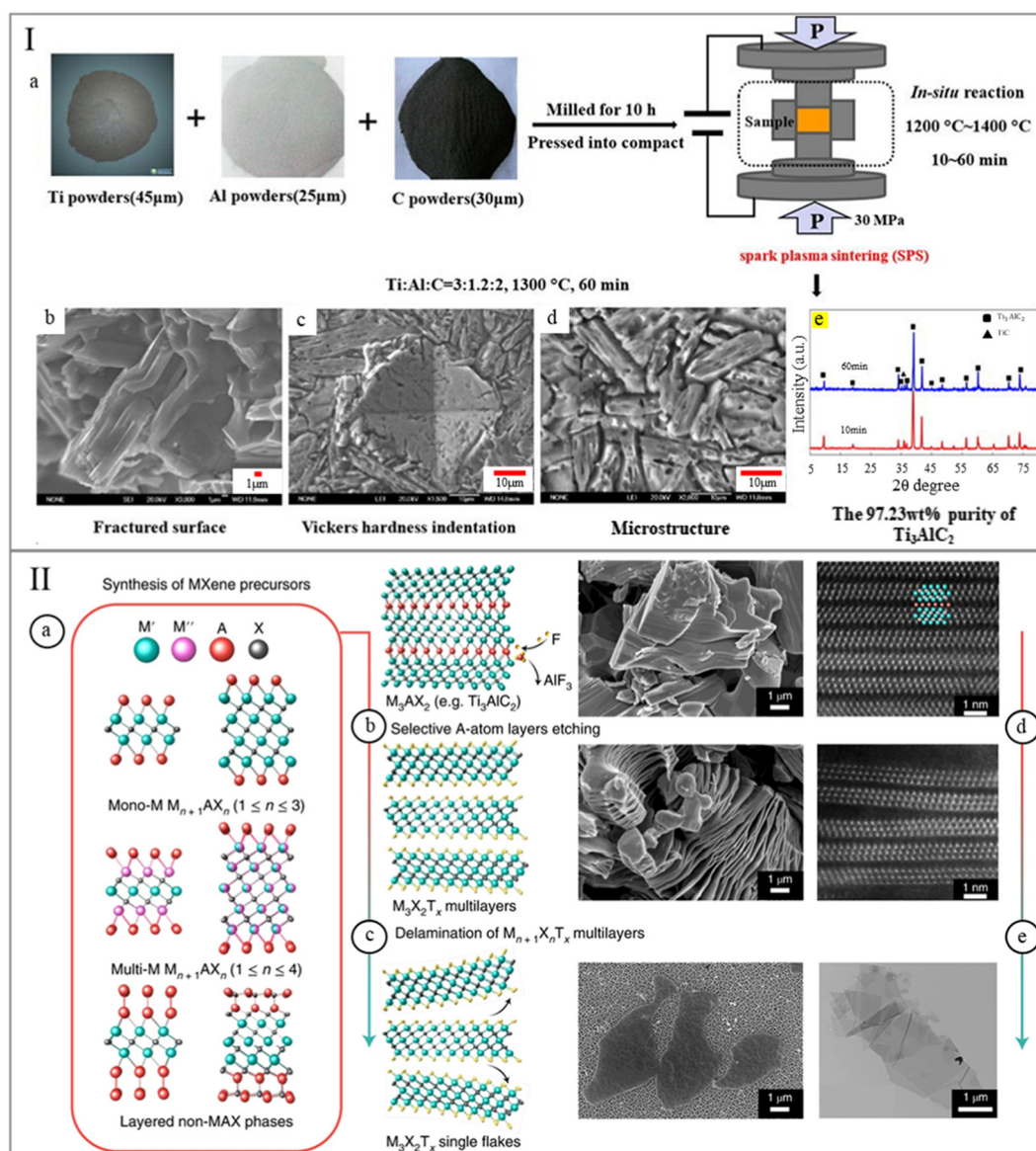
Fig. 2 (I) A schematic illustration and analysis of the *in situ* reaction process and mechanical behavior during MAX phase synthesis: (a) the *in situ* synthesis of the MAX phase from elemental precursors (Ti, Al, and C); (b) SEM micrographs of the fractured surface of the MAX phase (Ti_3AlC_2); (c) the microstructure of the Vickers hardness indentation on the MAX phase sample; (d) an SEM image of the as-synthesized Ti_3AlC_2 sample; and (e) XRD patterns of the as-synthesized Ti_3AlC_2 and TiC samples. Reproduced with permission from ref. 60; copyright 2020, ELSEVIER. (II) A schematic representation of the synthesis of the MAX phase (and non-MAX phase) and MXene nanosheets: (a) illustrations of the formation of the MAX phase (Ti_3AlC_2) and non-MAX layered materials; (b) etching and exfoliation of MXene precursors; (c) delamination into single-layer MXenes; (d) SEM and STEM characterization of the MAX phase (Ti_3AlC_2), with SEM (left) and atomic-resolution cross-sectional STEM (right) images; and (e) SEM and STEM characterization of multilayer $Ti_3C_2T_x$ MXenes, with SEM (left) and STEM (right) images. Reproduced with permission from ref. 63; copyright 2022, Nature.

in Fig. 3(I).[71] They exfoliated the MAX phase with HF and then subjected it to ball milling with red phosphorus. Following this, the layered material fragmented into QD/red-P composites with a thickness of 2–5 nm and length of about 6 nm that showed a high specific capacity of sodiation $\approx$600 mAh g^{-1} at 100 mA g^{-1}. This study provides a good alternative to produce QDs from 2D MXene. Despite having several advantages, including low cost, the use of inexpensive equipment and suitability for industrial-scale production,[72] this approach also has

certain limitations, including a heterogenous size distribution, the risk that mechanical energy may cause structural damage and that abrasions from the milling equipment may introduce impurities into the QDs, and limited functionalization opportunities; these ultimately constrain the application of the produced MXene QDs.[73] To overcome these hurdles, researchers have explored alternative routes to obtain MXene QDs that offer better control over size, crystallinity, and functionalization compared to ball-milling methods.
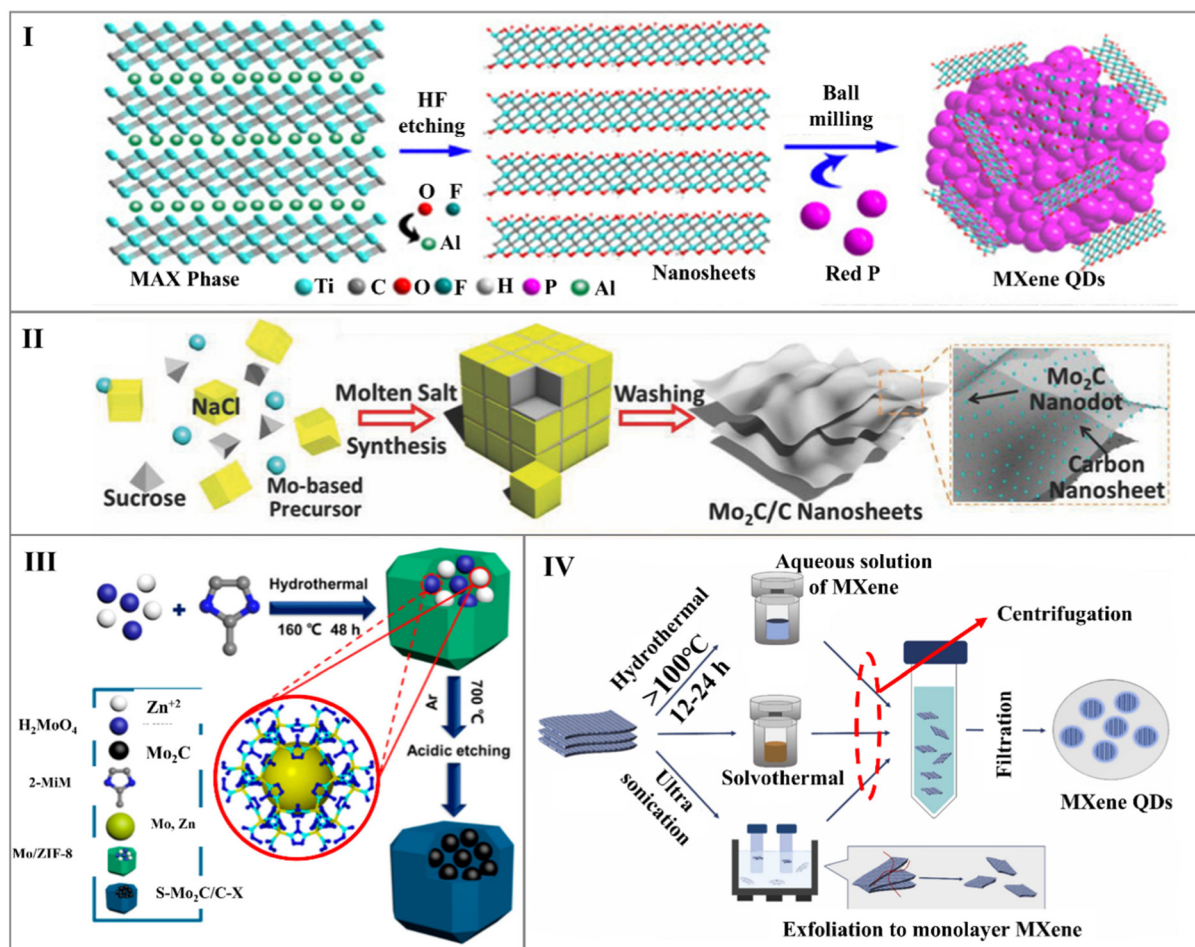
Fig. 3 Schematic illustrations of different synthesis methods for MXene QDs. (I) A schematic representation of the ball-milling method used for red-P-assisted MXene QD synthesis showing chemical etching and the mechanical size reduction process facilitated by red P. Reproduced with permission from ref. 71; copyright 2017, Wiley. (II) A schematic representation of the molten salt synthesis method used to obtain Mo₂C nanodots embedded over ultrathin carbon nanosheets, employing high-temperature salt-assisted etching and chemical cutting. Reproduced with permission from ref. 74; copyright 2018, Wiley. (III) A schematic representation of the pyrolysis method used for Mo₂C (MXene)-decorated polyhedron synthesis demonstrating *in situ* MXene nanostructure growth. Reproduced with permission from ref. 75; copyright 2018, ACS Publications. (IV) A general schematic representation of hydrothermal, solvothermal, and ultrasonication synthetic routes used for MXene QDs, highlighting the thermal decomposition, solvent-driven cutting, and ultrasonic fragmentation. Reproduced with permission from ref. 56; copyright 2023, ELSEVIER.

2.2. Molten salt synthesis

Molten salt synthesis is a rapid, straightforward, and established approach for the synthesis of MXene-derived materials including MXene QDs.[76,77] It involves the utilization of molten salts having a lower melting point than the reactant, which act as the reaction medium and serve as a solvent. It includes the use of chlorides, fluorides, and or eutectic mixtures that provide highly ionic environments and favor the unified diffusion and reaction of precursors.[78] It is carried out at elevated temperatures that promote the self-assembly of precursor materials under an inert atmosphere that minimizes oxidation processes. The ionic nature of the molten salt enables precise control over the size and uniformity of QDs, supporting desirable properties. A study by Cheng *et al.* proposed MXene QD synthesis through a molten salt route, as shown in Fig. 3(II).[74] They prepared QDs by uniformly mixing a molybdenum-containing precursor and sucrose in NaCl.

Following this, nanocubic crystals of NaCl formed through continuous precipitation and stacking. Then, the molybdenum-containing precursor and sucrose were confined in the interstices of the crystals. Then, the material was subjected to heat treatment to obtain Mo₂C/C nanosheets embedded with nanodots. Besides this, various researchers utilized a combination of different methods to obtain superior QDs. These molten salt synthesis methods require corrosive salts and high temperatures for reactions, which limits the synthesis of MXene QDs. To overcome these hurdles, researchers employed hydrothermal methods employing water as the medium and using low temperatures compared with molten salt synthesis methods.

2.3. Pyrolysis

Pyrolysis is a high-temperature thermal decomposition method employed in the absence of oxygen.[79] It involves the

use of precursors of MXene QDs including inorganic or organic compounds containing Ti, C, N, or other transition metals. These act as building blocks that incorporate the individual components with the prime goal of producing QDs with desirable properties. It is carried out at very high temperatures (with a gradual heating rate) and depends on the thermal stability and decomposition properties of the precursors to ensure uniformity.[80] The oxygen-free reaction environment retains the structural integrity by minimizing oxidation. A study by Wang *et al.* proposed the incorporation of Mo_2C nanoparticles *via* a pyrolysis route, decorated them with carbon polyhedrons and employed them for enhanced microwave absorption, as illustrated in Fig. 3(III).[75] They used Mo-substituted ZIF-8 as a self-sacrificing precursor material which was subjected to direct pyrolysis under inert atmospheric conditions. The obtained composite inherits a polyhedral profile from the precursor and also promises a highly uniform distribution. Despite having several advantages, as explained above, it requires specialized equipment with a controlled atmosphere and very high energy for pyrolysis, which may promote particle agglomeration that limits the overall synthesis and application of the produced MXene QDs.[81] To overcome this, researchers explored newer synthetic routes to obtain MXene QDs that offer precise control over morphology and size, with low temperature reactions and wider surface functionalization compared to pyrolysis methods.

2.4. Hydrothermal synthesis

The hydrothermal synthesis mechanism is one of the simplest and most popular approaches for synthesizing MXene QDs with a homogenous particle size distribution and outright crystal form.[19,82] This approach involves the etching of aluminum from the MAX phase followed by the exfoliation of the multilayered material into few-layered MXene nanosheets ($Ti_nC_{n-1}T_x$).[83,84] Then, the heterogeneous chemical reaction of 2D MXene sheets in an aqueous environment under high pressure (>1 bar) and at high temperature (>80 °C) was carried out within a PTFE-lined sealed autoclave in an oven.[85,86] In general, the MXene QD synthesis environment was kept slightly alkaline/slightly acidic or neutral (pH 6–8 or 9) and the temperature was kept in the range of 80 °C to 150 °C. The reaction conditions used in the system may influence the density of water and the dielectric constant, which can further affect the morphology and reaction rate. This approach offers better control over the size of the produced MXene QDs.[87] In the last few decades, MXene QDs have captivated researchers worldwide, owing to their unique electronic and optical properties and exceptional stability across a wide range of conditions. Researchers produced colloidal MXene QDs with different morphologies and strong quantum confinement effects by treating 2D sheets at different temperatures through this route.[88] In a report, Kong *et al.* proposed the synthesis of titanium carbonitride through a one-step hydrothermal method, exhibiting excellent fluorescence activity.[89] A study by Xue *et al.* proposed that upon increasing the hydrothermal temperature, the crystallinity of the produced MXene QDs

decreases, which may modify the surface composition and successively affect the optical and electronic properties.[90] Another study by Ai *et al.* proposed a hydrothermal route for MXene QD synthesis, and they functionalized them with amino groups to develop a photoluminescent sensor probe for histidine detection, reporting a LOD of 3.52 nm.[91] This developed probe showed high sensitivity and selectivity in the presence of other interferents. These MXene QDs displayed vibrant blue fluorescence, which was attributed to surface defects and quantum confinement effects. A different study by Li *et al.* reported MXene QDs for the hydrogen evolution reaction.[92] They employed a hydrothermal route and combined it with a g-C_3N_4 nanostructure to develop MXene QDs@ g-C_3N_4 that was further employed in the photocatalytic H_2 evolution reaction. Fig. 3(IV) illustrates the hydrothermal method of MXene QD synthesis. It is very important to understand that hydrothermal reactions are carried out in the presence of water only, which limits any precise control over surface functionalities and requires very high temperatures for the chemical cutting of MXene nanosheets. To overcome such hurdles, researchers have employed solvothermal approaches for MXene QD synthesis that are explained in detail below.

2.5. Solvothermal synthesis

The solvothermal method is an effective and versatile approach employed for MXene QD synthesis, offering precise control over the shape, size, and surface functionality.[93] It involves the chemical treatment of the MXene under moderate to high temperatures and pressures in a sealed autoclave employing organic solvents, such as DMF, and ethanol as reaction media.[94] This synthetic route leverages the solubility of MXene precursors in organic solvents under high pressure and temperature to produce high-quality MXene QDs through the oxidative cutting of layered materials. These solvents play a dual role: they serve as the reaction medium and provide functional groups to the final QDs, and they also facilitate uniform fragmentation and functionalization with unique optical and electronic properties compared to their counterparts.[95,96] The organic solvent's interaction with the MXene nanosheets facilitates stabilization and prevents aggregation while its reducing or oxidizing properties may introduce specific functional groups to the QDs.[97,98] Therefore, the choice of solvent profoundly impacts the properties of the resulting QDs. Solvents with a high boiling point help to achieve stable environmental conditions at high temperatures while the polarity of the solvents and their chemical reactivity can influence the degree of exfoliation and functionalization of the MXene precursors.[99,100] The solvothermal temperature and pressure are vital in determining the fragmentation efficiency and size distribution.[101] In broad terms, an elevated temperature contributes to sharp fragmentation, producing finer QDs that exhibit higher quantum confinement effects. However, extreme temperatures may lead to undesirable agglomeration or over-oxidation. Besides this, reaction time is another important parameter that affects the extent of surface functionalization and the degree of fragmentation. A short reaction time may

produce wider QDs while a prolonged reaction time may produce finer QDs with superior functionalization. However, the optimization of different parameters, including reaction time, is necessary to obtain smaller MXene QDs with ideal structural integrity. A study by Feng *et al.* proposed a MXene-QD-based fluorescent probe for the detection of copper ions.[102] They exfoliated MXene sheets employing a DMF-solvent-aided sonication approach to obtain few-layered MXene nanosheets. Subsequently, through a solvothermal chemical cutting approach involving treatment with three different doses of amine, three different types of QDs were obtained. Another intriguing study by Siya Lu *et al.* proposed the synthesis of MXene QDs that exhibit outstanding two-photon white fluorescence and also explored the changes in the color of emitted light at various pressures.[103] Here, they etched the MAX phase to obtain MXene nanosheets, which were further treated by a two-step solvothermal process that sliced the sheets to obtain functionalized MXene QDs. Fig. 3 (IV) represents the solvothermal method used for QD synthesis, employing high temperature and pressure. Despite having several advantages, as explained, the use of slightly longer reaction times and high-pressure conditions can make it challenging to scale this approach for industrial production. To overcome such challenges, researchers explored alternative methods to the above-described methods, such as ultrasonication, which relies on high-frequency sound waves for rapid exfoliation and chemical cutting.

2.6. Ultrasonication

Ultrasonication is a simpler approach for synthesizing MXene QDs, employing high energy ultrasonic waves with the prime goal of obtaining a high surface area/pore ratio.[104,105] In this approach, mechanical energy produced by ultrasonic vibrations is used to slice the layered MXene nanosheets, leading to the formation of QDs. In this approach, MXene nanosheets were dispersed in a suitable solvent, typically ethanol, water, or other polar solvents, to obtain a stable suspension.[106,107] Then, ultrasonic vibrations were applied to this dispersion, employing an ultrasonic bath. The produced high-frequency waves create localized low-pressure and high-pressure zones in the solvent, leading to the formation of cavitation bubbles.[108] The collapse of these bubbles generates intense shock waves and high shear forces that break down the layered MXene nanosheets into nanoscale MXene QDs. The ultrasonication time, power, intensity, and solvent selection are critical parameters that significantly influence the size, quality, and surface functionalities of the produced MXene QDs. This approach offers an energy-conserving alternative to the high-energy-consuming alternative approaches explained above. Fig. 3(IV) illustrates the ultrasonication method of QD synthesis. A study by Zhang *et al.* proposed fluorescent MXene QDs that were synthesized through a one-step ultrasonication route and deployed for the detection of iron.[109] The etching of the MAX phase was carried out over an ice-water bath using HF and stirred at 45 °C for 24 h; then, the obtained 2D sheets were dispersed in DMSO

and further stirred for 24 h. Then, the reaction mixture was centrifuged and washed multiple times to remove DMSO from the supernatant. Following this, it was subjected to sonication for 10 h, and then centrifugation, and the obtained supernatant was filtered with a 220 nm membrane; the obtained filtrate was MXene QDs. It was mixed with 20 μL of iron at different concentrations; following this, the fluorescence intensity was recorded under 380 nm excitation and a LOD of 310 nM was proposed.

Each synthesis method explained above has its own advantages and disadvantages. The selection of the appropriate synthetic route depends on the desired properties and intended applications. The obtained QDs can be employed as sensing probes for the development of miniaturized optoelectronic devices, finding application in sensing a diverse range of molecules. In this study, we covered the sensing of small molecules, macromolecules, and environmental pollutants, and this is discussed in detail below.

3. Properties of MXene QDs

The 2D MXene nanosheets harbor numerous excellent properties and allow the formation of 0D QDs through chemical cutting treatment. Therefore, these QDs will not only inherit the properties of their parent 2D MXene nanosheets but will also harbor numerous unique properties due to quantum confinement effects. In this paper, we comprehensively discuss the unique properties of MXene QDs, including structural, optical, electronic, and biocompatibility properties, that make these QDs very unique in the zero-dimensional nanomaterial category.

3.1. Structural properties

Research on the structure of MXene QDs is very crucial to reveal their unique properties and unlock their full potential for diverse applications. Structural properties include the electronic structure, crystal structure (crystallinity), size, morphology, symmetry, unit cell parameters, and surface functional groups, which can significantly influence the physical, chemical, and optical behavior of QDs.[22] Gaining a fundamental understanding of all these parameters provides critical insights into how these QDs interact with the environment and also enables the precise tuning of their properties for the desired applications.[110,111] These QDs have hexagonal symmetry as per their parent MAX phase and crystalline core region, which can be confirmed through the SAED pattern.[82] The 2D nanosheets ($M_{n+1}X_nT_x$) comprise $2n + 1$ layers, where layer "X" is sandwiched by "M" layers with a coordination number of six (usually) that implies that the transition metals "M" in MXenes make six chemical bonds with neighboring "X" atoms.[112,113] The topological height of a single MXene nanosheet is generally <1 nm, having dominant [002] crystal plane orientation corresponding to the stacking of 2D sheets.[114] MXene QDs exhibit an ultrasmall quasi-spherical nanostructure, with lateral dimensions of <10 nm and a thick-

ness of ~1–3 nm; the uniformity depends on the exfoliation and chemical cutting routes used. HRTEM can be used to deduce the lattice fringes that correspond to the (002), (100), or (110) crystalline domains of individual MXene QDs.[115] The unit cell dimensions rely on the nature of the transition metal (M), the number of atomic layers (n), and the extent of surface terminations.[30] Furthermore, the chemical etching of the MAX phase induces numerous surface terminations (including –F, –OH, and –O), as reported in numerous literature studies, which can be confirmed by XPS and FTIR analysis of QDs.[116,117] These surface terminations play a crucial role in determining the structural stability, interfacial chemistry, electronic coupling, bond-length variations, and stabilization of the quantum-confined structure by preventing aggregation, ensuring colloidal stability.[98] Multiple washing cycles after etching can readily switch out –F groups partially or completely. A study by Lie *et al.* proposed that very high temperatures may oxidize the MXene nanosheets, which converts –OH surface terminations into –O groups.[118] Fig. 4(I–VIII) illustrates the structural properties of MXene QDs, highlighting their morphology, crystallinity, and atomic arrangements, which are revealed through corresponding characterization techniques. Recent studies suggest that the position of surface termination groups is more complex than previously predicted. Studies have exhibited three feasible positions for surface terminations in MXenes and derivatives, such as: (a) placed on the roof of "M" atoms, (b) placed on the hollow position I between three adjacent "X" atoms below the "M" atoms, and (c) placed on hollow position II on the roof of "X" atoms, as illustrated in the top view of QDs depicted in Fig. 4(XII). DFT analysis suggested that surface terminations placed at position I on the two sides of the MXene were the most stable due to less steric hindrance. Position II becomes favorable for MXenes where "M" atoms cannot facilitate enough electron transfer for both "X" atoms and surface groups. –OH and –F terminations require one electron at the adsorption sites and are inclined towards position I, while –O surface terminations require two electrons from the "M" atoms, so low-valence "M" components shifts their locations towards position II.[119,120] The accurate positioning of surface terminations depends on both the composition and type of MXene, and further investigations are required to explore more fundamentals of structural properties.

3.2. Electronic properties

The electronic properties of MXene QDs are very crucial and depend on numerous parameters, including quantum confinement effects and surface terminations. A high electron density in "M" atoms (d–e^-) close to the Fermi level (E_F) provides metallic conductivity to QDs.[127] This can be tuned through the composition and surface terminations of the QDs and it is reported that resistance is enhanced by the number of layers and, thus, nanosized QDs show better electron transfer compared to their stacked counterparts. In an organized double "M" sandwich-like structure, the outer "M" layer has more effects on the electronic properties compared to the inner "M"

layer.[128,129] This "M" layers pertains to MXenes in general, and is not exclusive to MXene QDs. In a study, Zeng *et al.* proposed elevated photo/electrocatalytic activity in MXene QDs due to their excellent electrical conductivity, dramatically facilitating charge transfer and enhancing active sites.[130] Compared to MXene carbides, MXene nitrides and carbonitrides exhibit overall higher densities of states (DOS) due to more robust "M"–N bonds (in relation to "M"–C bonds), and additional nitrogen electrons provide enhanced electrical conductivity.[131] DFT can be used for the investigation of DOS and energy band structures (EBS), where the DOS are projected on the "M"-d and "X"-p states and the EBS are drawn along the high symmetry points of the hexagonal BZ.[129] Fig. 4(IX, X, and XI) illustrates DOS obtained *via* DFT calculations and Fig. 4(XIII) illustrates the spin density of MXene QDs. Surface terminations could significantly alter the electronic properties; this may be due to the formation of new bands below E_F. Therefore, E_F decreases, thus reducing the DOS, raising the -d band up above E_F and generating an energy gap (E_g), especially for O-terminated MXenes, including Ti_2CO_2, $ZrCO_2$, $HfCO_2$, $ScCF_2$, $ScC(OH)_2$, and Sc_2CO_2 with E_g values of 0.24, 0.88, 1.0, 1.03, 0.45, and 1.8 eV, respectively. All these MXenes, except $ScC(OH)_2$, are recognized as indirect band-gap semiconductor materials, while $ScC(OH)_2$ is recognized as a direct band-gap semiconductor material.[132–134] This may due to hybridization between the d-orbitals of the "M" atoms and the p-orbitals of surface terminations. Besides this, the work function (WF) of MXenes can also be obtained by DFT analysis, which suggests an order of O- > F- ≥ bare > OH-terminated MXenes; the E_F value is shifted lower, thus increasing the WF of O- and F-terminated MXenes. MXene QDs prepared through laser ablation in suspension showed band gaps of 2.2, 2.12, 1.98, and 1.94 eV for Ti_2C QDs, V_2C QDs, Nb_2C QDs, and Ti_3C_2 QDs, significantly broadened compared to their parent nanosheets. This broadening in bandgap arises from the quantum confinements of charge carriers within nanoscale dimensions. As these lateral dimensions lead to confinement with discrete energy forms, this causes the separation of the conduction band from the valence band, similar to the cases of graphene and other semiconductor QDs. This semiconducting nature with appropriate band gaps enables their applicability in fluorescence imaging, photocatalysis, and optoelectronic devices.[135]

3.3. Optical properties

The MXene QDs exhibit remarkable optical characteristics, including light absorption, photoluminescence (PL), and electrochemiluminescence (ECL). The optical characteristics of these QDs differ from their bulk counterparts and are primarily governed by synergistic effects from quantum confinement (size effects), surface terminations, and edge defects. These can be tuned by changing the reaction conditions, including the solvent, temperature, pH, and functional modifiers.[136–138] The tunable energy band structure, unique electronic transitions, and surface terminations allow MXene QDs to show remarkable light absorptivity ranging from UV to near-infrared
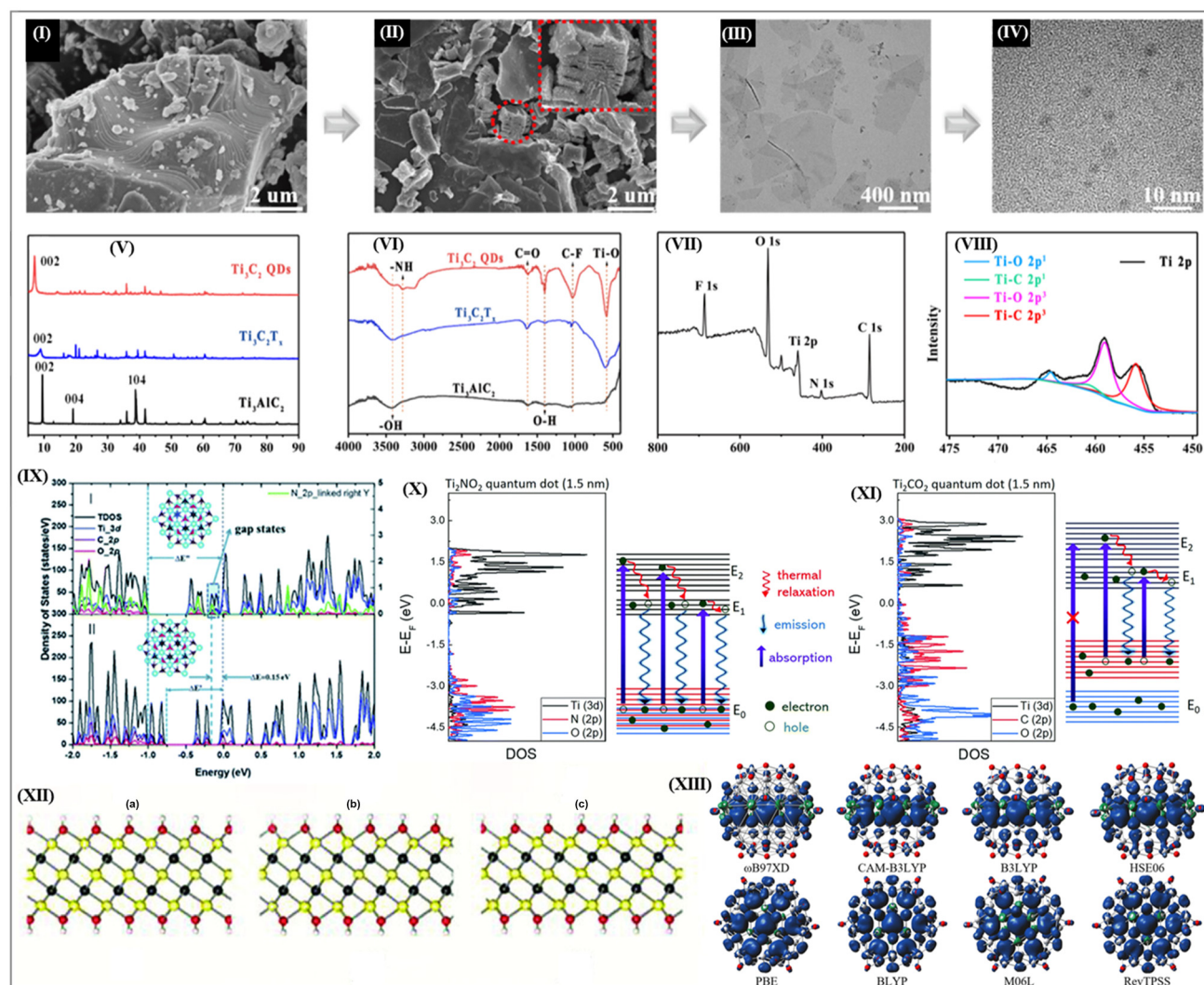
Fig. 4 (I) An SEM image of a MAX phase showing the typical accordion-like layered structure; (II) an SEM image of multilayered $Ti_3C_2T_x$ nanosheets after the selective etching of "Al", showing the slightly dispersed layered structure; (III) a TEM image of few- or mono-layered $Ti_3C_2T_x$ nanosheets; and (IV) a TEM image of $Ti_3C_2T_x$ QDs showing the uniform and small QD structure. Reproduced with permission from ref. 121; copyright 2022, MDPI. (V) The XRD spectra of the MAX phase, $Ti_3C_2T_x$ nanosheets, and Ti_3C_2 QDs; (VI) FTIR spectra of the MAX phase, $Ti_3C_2T_x$ nanosheets, and Ti_3C_2 QDs, highlighting changes in surface chemistry after each step through the presence of characteristic functional groups; (VII) the full-scan XPS spectrum of Ti_3C_2 QDs; and (VIII) the high-resolution Ti 2p XPS spectrum for Ti_3C_2 QDs representing the phase transformation and loss of long-range order upon QD formation. Reproduced with permission from ref. 122; copyright 2021, ACS Publications. (IX) A representation of the density of states (DOS) obtained from DFT calculations for (I) N-doped Ti_3C_2 quantum dots (QDs) and (II) pristine Ti_3C_2 QDs. The introduction of nitrogen dopants alters the electronic structure, as evidenced by the changes in the density near the Fermi level, indicating enhanced electronic conductivity and potential active sites. Reproduced with permission from ref. 123; copyright 2018, RSC. The DFT-calculated electronic structures of 1.5 nm (X) Ti_2NO_2 and (XI) Ti_2CO_2 MXene QDs. The energy levels corresponding to the valence band (E_0), conduction band (E_1), and higher-energy conduction band (E_2) are indicated. Distinct differences in band alignment and energy separation suggest tuneable electronic properties based on the surface termination chemistry. Reproduced with permission from ref. 124; copyright 2022, RSC. (XII) A top view of MXene QDs where surface terminations are (a) placed on the roof of "M" atoms, (b) placed on the hollow position I between three adjacent "X" atoms below the "M" atoms, and (c) placed on hollow position II on the roof of "X" atoms. Reproduced with permission from ref. 125; copyright 2018, WILEY. (XIII) The spin density of the quintet state ($m = 4\mu_B$) for QD1 calculated using various density functionals. Titanium, carbon, and oxygen atoms are shown in light grey, dark grey, and red, respectively. The isosurface value is set at 0.002 e bohr^{-3}; blue and green represent positive and negative spin densities, respectively. Reproduced with permission from ref. 126; copyright 2023, RSC.

(NIR), as illustrated in Fig. 5(I). These QDs are capable of converting absorbed light energy into other energy forms, including thermal energy and chemical energy.[139–141] Photoluminescence (PL) is one of the crucial optical features of MXene QDs, which typically show excitation-dependent photoluminescence, which is attributed to surface states, the size distribution, and heterogenous surface terminations.[142] Upon excitation with UV or visible light, they show a broad
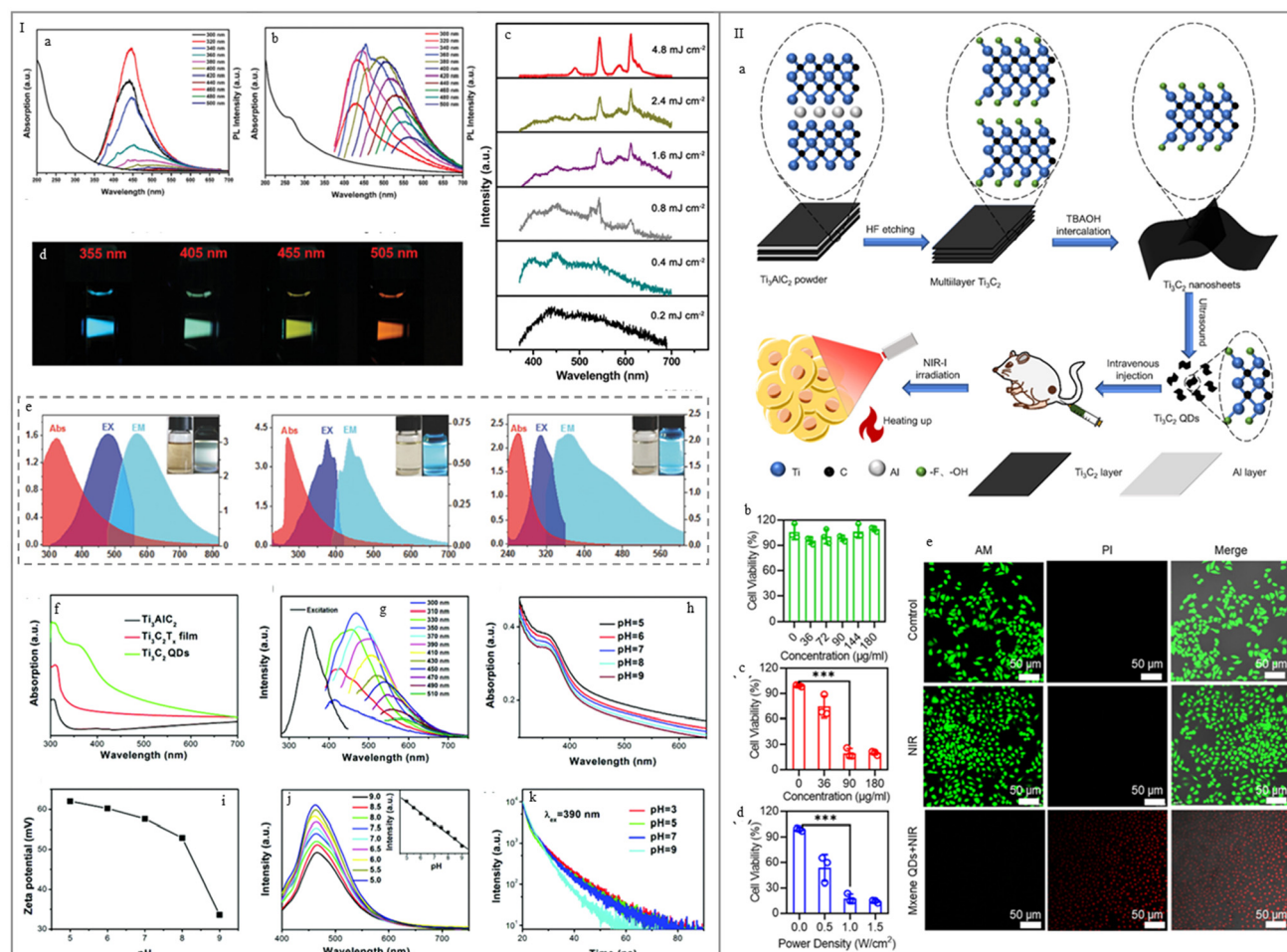
Fig. 5 (I) The optical characteristics of MXene QDs: (a) UV-vis absorption (left) and photoluminescence (PL) spectra of V$_2$C MQDs without passivation in aqueous solution. (b) UV-vis absorption (left) and PL spectra of V$_2$C MQDs with passivation treatment. (c) Emission spectra of a V$_2$C MQD colloid at varying pump fluences. The corresponding peak intensity and linewidth evolution indicate the lasing threshold behavior. (d) Photographs of V$_2$C MQDs at different excitation wavelengths using a xenon lamp. Reproduced with permission from ref. 160; copyright 2019, WILEY. (e) The respective UV-vis absorption, maximum excitation (EX), and emission (EM) spectra peaks of the QDs; insets: photographs of the QD dispersions under 365 nm UV irradiation. Reproduced with permission from ref. 161; copyright 2018, WILEY. (f) UV-vis absorption spectra of Ti$_3$AlC$_2$, Ti$_3$C$_2$T$_x$ film, and Ti$_3$C$_2$ Mxene QDs. (g) Excitation and emission spectra of Ti$_3$C$_2$ QDs in aqueous solution. (h) pH-Dependent UV-vis absorption spectra of Ti$_3$C$_2$ QDs. (i) Zeta potentials of Ti$_3$C$_2$ QDs in buffer solutions of varying pH. (j) Emission spectra at different pH values (λ_{ex} = 350 nm). (k) Photoluminescence decay curves at 460 nm under 390 nm excitation at 25 °C at different pH levels. Reproduced with permission from ref. 162; copyright 2018, RSC. (II) MXene QD based photothermal anti-cancer therapy and the relative cell viability of HepG2 hepatocellular carcinoma cells after 24 h of incubation with varying concentrations of MXene QDs (0, 36, 72, 90, 144, and 180 ppm), demonstrating dose-dependent cytotoxicity: (a) a schematic illustration of MXene-QD-based anticancer therapy; (b) and (c) cell viability of HepG2 cells incubated with MXene QDs (0, 36, 90, and 180 ppm) for 4 h followed by 808 nm laser irradiation (1.0 W cm^{-2}, 5 min); (d) cell viability of HepG2 cells treated with 90 ppm MXene QDs and exposed to different laser power densities (0.5, 1.0, and 1.5 W cm^{-2}), indicating power-dependent photothermal effects; and (e) confocal laser scanning microscopy images of treated cells stained with calcein-magnesium (AM, live cells) and PI (dead cells) at the end of exposure, illustrating photothermal-therapy-induced cell death. Reproduced with permission from ref. 163; copyright 2024, ACS Publications.

emission spectrum, covering the visible range, having emission maxima that can be tuned based on the excitation wavelength. MXene QDs achieve strong PL emission compared to parent 2D MXene nanosheets, although the mechanism is still less well known. There are two universally accepted opinions, namely related to surface defects and size defects.[143–145] The PL behavior of MXene QDs has often been investigated through three main parameters, including PL lifetimes (PLLTs), PL color, and PL quantum yields (PLQYs). The PL

spectra of QDs at different excitation wavelengths suggested that these QDs show excitation-dependent fluorescence emission.[136,146,147] In addition to this, the PL behavior of the QDs can be tuned by changing various parameters, including the temperature, pH, solvent, size of the QDs, and doping agents.[142,148,149] A study by Xu *et al.* proposed MXene QDs using different solvents including DMSO (s-QDs), ethanol (e-QDs), and DMF (f-QDs).[146] Upon exposure to 365 nm UV light, these QDs showed different PL colors and these were

white (DMSO) and blue (DMF and ethanol). The PLLTs were proposed to be 4.7 ns, 25 ns, and 2.1 ns and the PLQYs were 4.1%, 10.7%, and 6.9%. Fig. 5(Id) illustrates the interaction of photons with MXene QDs, leading to electronic transitions and the emission of photoluminescence (PL) with different colors. The excitation of electrons from the valence band to the conduction band followed by radiative recombination results in distinct PL emission depending on the QD properties and excitation wavelength. Along with PL, ECL is also considered as a crucial optical property that may be used to assess MXene QD capabilities and help in broadening their scope.[150] ECL involves a mechanism that transforms electrical energy into a measurable fluorescence signal. It involves the generation of excited states *via* electrochemical reactions and a return to ground states as light is emitted. It involves features from both electrochemistry and chemiluminescence that make it a more effective analytical tool with minimum background interference.[151,152] The high conductivity and large surface area of QDs promote electron transfer and enhance the ECL efficiency. However, while these MXene QDs are well known for their optical and electronic properties, their ECL characteristics still remain underexplored.[153] Most of the research on MXene QDs has largely focused on their photothermal, photocatalytic and photoluminescence properties due to their apparent applicability to bioimaging, sensing, and energy applications. These QDs are prone to oxidation which limits their applications in the electrochemical environments that are necessary for ECL studies. Despite these challenges, these QDs have immense potential for ECL applications due to their unique electrical conductivity, tunable surface terminations, and high surface area. Substantial research is required to unlock the full potential and gain the fundamental understanding of these QDs that may open possibilities for innovative applications such as ECL-based devices for use in miniaturized wearable technology. In addition to this, the UV-visible absorption spectra of MXenes are typically broad, ranging from the ultraviolet to the visible region. They show a strong absorption peak at 200–300 nm, corresponding to the π–π^* transitions of C=C bonds in the carbon framework of MXene QDs. The weaker absorption tails that may be observed in the visible region (300–500 nm) can be attributed to the n–π^* transitions of C=O or C–N functional groups, or d–d transitions in transition-metal centers.[154,155] The absorption behavior of these MXene QDs can be tuned through intercalation, heteroatom doping, or heterojunction formation with other nanomaterials. However, due to strong nanoscale quantum confinement effects, they show a larger band gap compared to their parent counterparts, which varies based on size and composition. Tuning these properties can significantly influence the optoelectronic properties. The optical band gap can be estimated using UV-vis absorption data through Tauc plot analysis methods, revealing a methodical blue shift upon reducing the particle size.[156] Furthermore, dopants can be used to modulate the electronic structure and density of states, which may tune the band gap of MXene QDs. Besides all these factors, MXene QDs also show remarkable fluorescence quenching phenomena that make them highly suitable optical sensing probes employing fluorescence "turn-off" and "turn-on" principles. These include static quenching, where ground-state complex formation occurs between MXene QDs and the analyte, while in some cases they show dynamic quenching where QDs interact with the analyte through collisions.[157] In the case of photoinduced electron transfer, analyte molecules accept electrons from MXene QDs, and in Förster resonance energy transfer (FRET), MXene QDs behave as energy donors or acceptors due to spectral overlapping and nanoscale size confinement. These properties enable applicability for detecting a wide range of analytes including biomolecules and environmental pollutants. Recently researchers unveiled the non-linear optical behavior of MXene QDs, including simultaneous two-photon absorption arising from quantum confinement, mainly depending on the nature of the transition metal and surface terminations.[158,159]

These unique optical properties of MXene QDs open countless opportunities for innovative applications in biomedicine, catalysis, optoelectronic devices, *etc.*

3.4. Biocompatibility and cytotoxicity of MXene QDs

MXene QDs derived from MAX phases harbor promising biomedical applications due to their unique physicochemical characteristics.[164] However, their real-world application in biological systems requires a comprehensive understanding of their biocompatibility and potential toxicity.[165–167] These QDs in general exhibit considerable biocompatibility, especially when appropriately functionalized or synthesized under controlled conditions. Surface terminations, typically hydroxyl (–OH) and oxygen (–O), may interact favorably with biological systems. Further functionalization (surface passivation) with biocompatible polymers or molecules (PEG, amino acids, or proteins) significantly enhances their biocompatibility with cells and tissue.[168–170] The ultrasmall size of MXene QDs may allow interactions at the cellular and sub-cellular level often without significant mechanical damage to membranes. *In vitro* evaluation of MXene QD cytotoxicity has been extensively carried out using MTT and cell counting kit-8 (CCK-8) assays across different species, including zebra fish, microorganisms, and mammalian cell lines (such as A549 and A375 cancerous cell lines, 3T3 murein fibroblast cancer cells, and HEK293 cells).[171,172] A study by Hu *et al.* proposed using the photothermal performance of MXene QDs for cancer treatment.[163] Fig. 5(II) illustrates the design and therapeutic evaluation of degradable MXene QDs for photothermal anti-cancer treatment under 808 nm near-infrared (NIR) laser irradiation. They demonstrated that MXene QDs showed great potential for the photothermal treatment of cancer, showing 62.5% photothermal conversion efficiency. They have proved the potent inhibitory effects of MXene-mediated PTT towards tumor cells both *in vivo* and *in vitro*, showing minimal harm to exposed mice. From such studies, we can conclude that MXene QDs offer significant promise for various clinical applications.

Despite having a promising role, there are certain factors that can also influence the potential toxicity of MXene QDs. MXene QDs show dose-dependent cytotoxicity, including ROS

generation, mitochondrial dysfunction, and apoptotic cell death.[173,174] Owing to their high surface reactivity, they cause oxidative stress in cells and lead to lipid peroxidation, protein denaturation, and DNA damage. In some cases, MXene QDs may release transition metals that potentially cause toxicity. There are different strategies that can be chosen to mitigate the potential toxicity of MXene QDs and enhance the biocompatibility, such as surface passivation, as explained above, the use of green synthesis routes, and functionalization with specific ligands for target delivery to reduce off-target interactions and systemic exposure. Numerous and well-explored short-term studies have shown favorable results, but there is a research gap relating to long-term *in vivo* effects, including biodistribution and potential accumulation in organs.

These unique biocompatible properties of MXene quantum dots (MXene QDs) offer tremendous potential for innovative applications in biomedical fields. These include cellular imaging, wearable biosensing, and targeted drug delivery, where low toxicity and effective cellular interactions are essential.

4. Application of MXene QDs in sensors

Sensors are devices or systems that detect physical, chemical, or biological signals.[175,176] Nanomaterials offer enhanced optoelectronic and catalytic properties compared to bulk materials, and they can be fabricated into sensors for enhanced sensitivity, stability, and selectivity. These exceptional properties have attracted the scientific communities towards their application in point-of-care diagnostic setup development.[177–179] These devices play a pivotal role in the early diagnosis of diseases (prevention) and/or in affecting the outcome of diseases (prognosis).[180,181] Due to their integrated miniaturized setup, portability and short processing times, it is thought that they could fulfill numerous unmet needs in the diagnostics and healthcare sectors.[182,183] The discovery of MXene in 2011 led researchers to explore other MXene-derived nanomaterials like 0D MXene QDs, 1D MXene nanoribbons, 2D nanosheets, and 3D nanoflower-like structures; these materials have superior optoelectronic properties compared with their parent bulk materials.[184–186] In this article we have comprehensively discussed 0D MXene QDs and their applications.

The excellent physical, chemical, and optoelectronic properties of MXene QDs and their extensive functionalization and tunability windows have drawn researchers attention for exploring their application in next-generation diagnostics.[22,187] They can be utilized as optoelectronic probes for sensor development, ensuring the well-being of humans and allowing significant improvements in the healthcare sector *via* disease diagnosis at an early stage.[22] MXene-QD-based sensors can be divided into different categories including electrochemiluminescence (ECL), photoluminescence (PL), and fluorescence (FL) sensors.

An electrochemiluminescence (ECL) sensor works by utilizing the chemiluminescence properties of luminophores (a luminescence system) that emit light upon returning to the ground state following electrochemical excitation.[188] ECL can follow two fundamental mechanisms: annihilation and co-reactant.[189] In the annihilation mechanism, both oxidized and reduced luminophore species are generated at the electrode interface. These two species interconvert between each other by generating an excited luminescent intermediate; upon relaxation, it emits photons and returns to the ground state. In the co-reactant mechanism, the oxidation and/or reduction of co-reactant species generates high-energy and highly reactive intermediates facilitating electrochemiluminescence. These reactive intermediates react with the oxidized and reduced luminophore species in solution (material dispersed in solvent) and change to the excited state; as they return to the ground state, they cause luminescence. The co-reactant mechanism is used when either radical-charged ions are not stable for chemiluminescence or, because of a narrow potential window, both radical ions were not formed.[190–192] In a study by Li *et al.*, a MXene-QD-based ECL sensor for the detection of the miRNA-27a-3p analyte was adopted.[193] They used bimetallic MXene-derived QDs (Mo_2TiC_2) and SnS_2 nanosheets/ lipid bilayer, and they deployed this for the sensing of gastric cancer biomarkers, obtaining a LDR of 1 fM–10 nM with a low LOD of 1 fM. Another study by Lu *et al.* proposed a novel sensor probe comprising porphyrin-functionalized GSH-MXene QDs.[194] MXene QDs were synthesized *via* a hydrothermal method, functionalized with glutathione (GSH), and subsequently conjugated with porphyrin ($TMPyP_4$) to enhance the ECL properties. The resulting MXene QDs–$TMPyP_4$ nanocomposite exhibited a strong and selective ECL response, which was efficiently quenched by Cu^{2+} ions. This enabled the construction of a sensitive "signal on–off" ECL biosensor for Cu^{2+} detection, demonstrating a wide LDR of 10 nM to 10 μM with a LOD of 3.22 nM, offering a highly stable and selective probe, as illustrated in Fig. 6(I).

A PL sensor works based on the phenomenon of light emission by photons after excitation as they return to the ground state.[197] Newly explored 0D MXene QDs have very high photoluminescence (PL) properties, aided by surface defects and edge effects. MXene QDs have characteristic fluorescence emission depending on the excitation wavelength and the size of the MXene QDs. They emit different colors such as green, blue, red, white, yellow, brown, or black based on the composition and synthesis method, and they can also be tuned further based on the synthesis conditions (like pH, temperature, and solvent), size of the QDs, the doping agents used, *etc*.[198–200] In a study by Lu *et al.*, a dual-emission photoluminescence sensor for hydrogen peroxide and xanthine sensing was reported.[201] They synthesized N-doped MXene QDs through solvothermal methods, using DAP (2,3-diaminophenazine) to obtain a functionalized nanocomposite probe. It acts as a dual-emission reverse-change sensor based on the photoinduced electron transfer effect, where MXene QDs act as the donor and DAP acts as the acceptor. They reported LODs
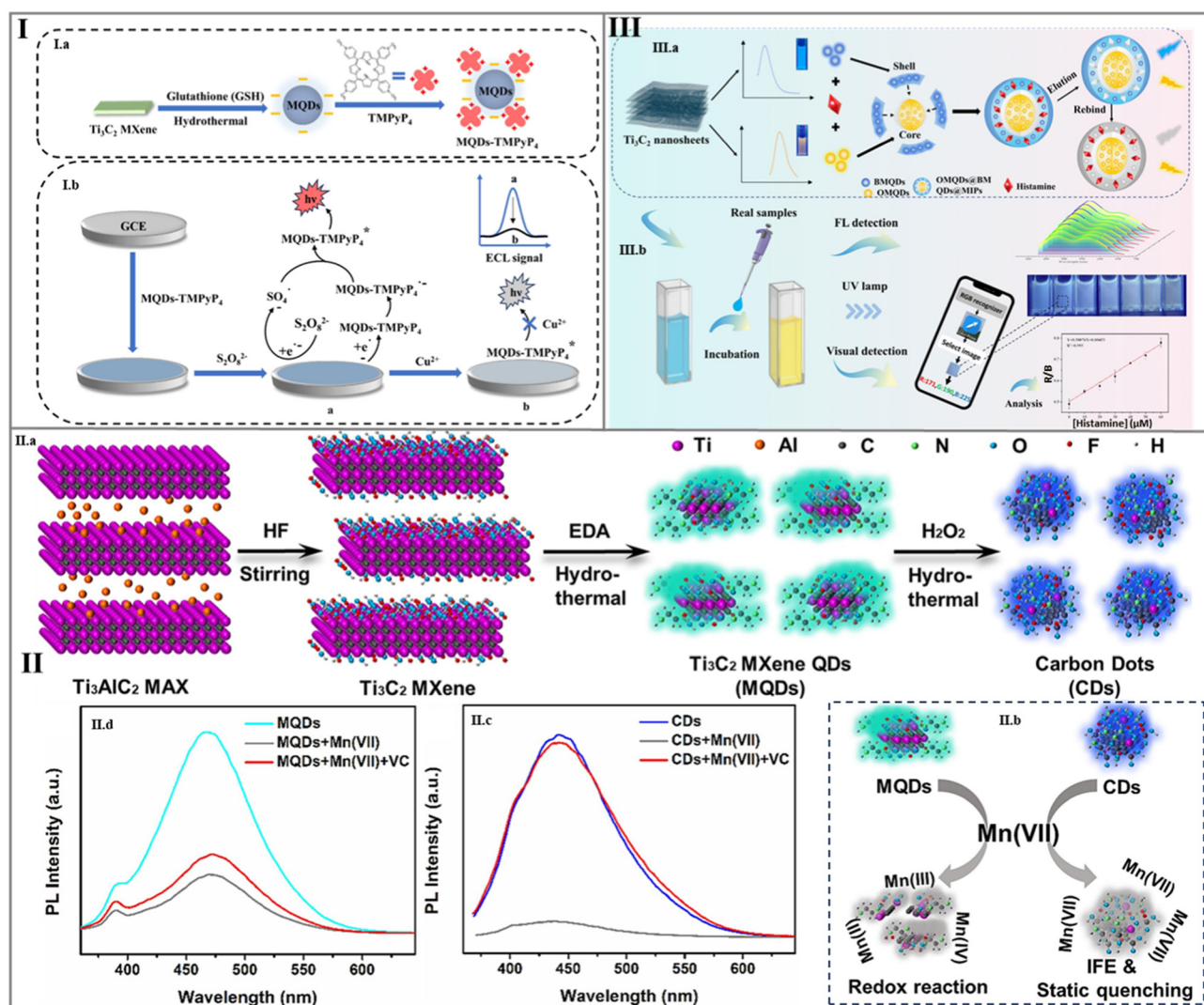
Fig. 6 (Ia) A schematic illustration of the construction process of a MQD–TMPyP$_4$ composite material; and (Ib) a schematic representation of an ECL biosensor based on the MQDs–TMPyP$_4$ composite for selective Cu^{2+} detection, depicting the sensing strategy and the underlying electrochemiluminescence (ECL) mechanism. Reproduced with permission from ref. 194; copyright 2024, ELSEVIER. (IIa) A schematic illustration of MXene QDs and carbon dots (CDs) obtained from MAX phase powder (Ti$_3$AlC$_2$) through sequential etching and hydrothermal treatment processes; (IIb) a pictorial representation of the detection mechanism for Mn(VII) based on the fluorescence response of MXene QDs and CDs, highlighting their interaction and fluorescence quenching behavior in the presence of Mn(VII) ions; (IIc) photoluminescence (PL) emission spectra of CDs, CDs + Mn(VII), and CDs + Mn(VII) + ascorbic acid (AA) under 350 nm excitation, demonstrating the fluorescence quenching by Mn(VII) and its subsequent recovery upon the addition of AA; and (IId) photoluminescence (PL) emission spectra of MXene QDs, MXene QDs + Mn(VII), and MXene QDs + Mn(VII) + ascorbic acid (AA) under 320 nm excitation. The lack of fluorescence recovery after AA addition indicates irreversible damage to the MXene QDs, caused by Mn(VII). Reproduced with permission from ref. 195; copyright 2023, ELSEVIER. (IIIa) A schematic illustration of a dual-emission MXene QD-based molecularly imprinted ratiometric fluorescence sensor, depicting the design strategy, fluorescence detection mechanism, and a visual representation of the detection process for selective and sensitive analyte recognition; and (IIIb) the integration of the developed ratiometric sensor with a mobile phone for rapid, on-site, and quantitative detection. The system demonstrates high selectivity, sensitivity, and real-time analysis capabilities for target molecules in complex real samples. Reproduced with permission from ref. 196; copyright 2024, ELSEVIER.

of 0.57 μM and 0.34 μM for hydrogen peroxide and xanthine, respectively. Another study by Wang *et al.* proposed a smartphone-enabled ratiometric molecularly imprinted fluorescence sensor based on dual-emission blue/orange MXene QDs for the selective detection of histamine.[195] The sensor exhibits a wide linear fluorescence response for histamine ranging from 1–60 μM, with a low LOD of 21.9 nM for fluorescence and 92.2 nM for visual detection. The platform enables rapid, on-site

analysis using a smartphone, with excellent recovery rates (96.52%–105.32%) being demonstrated in real food samples. This system highlights the potential of MQDs for portable and visual *in situ* food safety monitoring, as illustrated in Fig. 6(III).

A fluorescence sensor works based on the phenomenon of a fluorescence signal arising from the intermolecular interaction of chemicals. These sensors involve simple operation,

low cost, and short detection times, and they have been widely utilized for environmental pollutant monitoring. The fluorescence signal of the sensor is based on factors such as the movement of characteristic fluorescence peak positions, fluorescence quenching or enhancement, changes in fluorescence polarization, changes in fluorescence lifetimes, *etc*. The fluorescence properties of MXene QDs can be tuned by various factors like dopants and the size of QDs to obtain the desired properties for specific applications. MXene-QD-based fluorescence detection works based on single-wavelength emission data, which can be susceptible to the probe concentration and interference from the microenvironment. These couple of factors have been responsible for irreproducible and inaccurate findings. To overcome these hurdles, researchers combined two phenomena simultaneously and introduced a newer approach to develop fluorometric/colorimetric dual-channel nanoprobes. Recently Bai *et al.* reported a highly sensitive and selective dual-channel sensing nanoprobe (N,P-Ti$_3$C$_2$ MXene QDs).[202] The fluorescence properties of this dual probe were quenched by a 1,10-phenanthroline-Fe^{2+} complex (Phen Fe(II)) due to the inner filter effect (IFE) that partially or completely blocks the excitation/emission light of the fluorophore (QDs). As nitrite ions (NO^{2-}) were added, they were reduced by Phen-Fe(II) complexes, which diminished the IFE and finally led to fluorescence recovery and a gradual color change. These MXene QDs were also utilized by researchers as a deployable nanoprobe sensor in a biomedical sensor setup. Another study by Gu *et al.* proposed the dual-function application of Ti$_3$C$_2$ MXene QDs and derived carbon dots (CDs) for Mn(VII) detection and scavenging.[196] MXene QDs were prepared *via* hydrothermal methods using Ti$_3$C$_2$ nanosheets in the presence of ethylenediamine, followed by oxidation with H$_2$O$_2$ to obtain CDs. Both MXene QDs and CDs exhibit excellent dispersibility, fluorescence, and stability with nanoscale dimensions. MXene QDs demonstrate ultrasensitive fluorescence quenching, allowing Mn(VII) detection with a LOD of 5.2 nM due to their inherent reducibility and redox interactions with Mn(VII). In contrast, CDs—lacking reducibility—exhibit a selective Mn(VII) response *via* a synergistic inner-filter effect (IFE) and static quenching mechanism, with a LOD of 230 nM. The MXene QDs also effectively scavenge Mn(VII) from plant leaves, offering a dual-mode sensing and remediation platform. This comparative study presents the potential of MXene QDs for environmental and biological applications, as illustrated in Fig. 6(II).

The ever increasing population of the world poses an immense health-security burden, especially in developing countries like India and China which have a combined population of more than 2 billion.[203,204] This continuously increasing population creates an increasing demand for affordable and miniaturized diagnostic devices. The development and management of traditional diagnostic devices for such a huge population is a big hurdle because of the high cost, dedicated space requirements, *etc*.

Here, sensing platforms are utilized as efficient and advanced deployable sensing probes for the detection of numerous clinically and environmentally important molecules. The successful utilization of MXene QDs as detection probes offers a low-cost, high selectivity, and high sensitivity solution with a wide dynamic range and, most importantly, offers affordable alternatives for low- and middle-income individuals. Compared with the other QDs (like graphene and carbon QDs) MXene QDs show lower toxicity and higher biocompatibility which makes them a better prospect for clinical applications.[205] Due to their unique optoelectronic properties, they can be deployed for the development of biomedical sensors for the real-time monitoring of human health.

Currently, MXene-QD-based biosensors are widely used for the sensing of different categories of molecules, including micro-molecules, macro-molecules, and environmental pollutants; this is discussed in detail below.

4.1. Sensing of small molecules

Small molecules often serve as biomarkers for various physiological conditions and play a critical role in clinical diagnosis.[206,207] Significant changes in the concentrations of small molecules provide insights into disease progression or treatment response. They also facilitate the early detection of disease, often before symptoms arise.[208,209] Molecules including antibiotics, biogenic amines, uric acids, glutathione and low-molecular-weight peptides (*e.g.*, <900 Da) are considered part of the small-molecule category.[210] Expired and residual products from the pharmaceutical industry and hospitals lead to tonnes of pharmaceutical waste every year that is filled with an array of small molecules, which is a global menace as per the WHO.[211] This waste potentially leaks into natural resources, including food and water supplies, contaminating them to concerning levels. This creates a niche for developing a small, portable, low-cost, affordable sensing platform for small molecules. There is a plethora of small molecules for which MXene-QD-based sensors have been developed, some of which are described here, including antibiotics, uric acid, GSH, histidine, and tetracycline. Others are shown in Table 1 which covers sensor fabrication strategies, limits of detection (LODs), linear detection ranges (LDRs), synthetic routes, real sample detection, and the detection techniques involved in sensor development in those studies.

4.1.1. MXene-based uric acid sensors.

Uric acid is a heterocyclic compound that is produced as a byproduct of nucleotide degradation pathways and it behaves as a weak organic acid.[220] Its deposition leads to the painful rheumatic disease commonly known as gout.[221] Therefore, the detection of uric acid is essential for its management in the human body. In a study by Liu *et al.*, a MXene-QD-based colorimetric and fluorescence probe was developed that was employed in uric acid detection.[222] It was synthesized using 1.0 g of Ti$_3$AlC$_2$ in 16 mL of HF solution, which was stirred for 24 h at 40 °C. The obtained mixture was washed with distilled water till it reached pH 7 and the pellet was dried at 60 °C under vacuum conditions for 12 h. Then, it was dissolved in 10 mL of distilled water in a N$_2$ environment and sonicated for 5 h in a bath sonicator. The mixture was further centrifuged and a homogenous dispersion

Table 1 A comprehensive overview of sensor fabrication, LDRs and LODs with real sample considerations for small-molecule detection

| No.	Target	Probe composition	Detection technique	Fabrication method	LDR	LOD	Real sample	Ref.
Small molecules								
1	Quercetin (QC)	MXene-QDs	Fluorescence	It was synthesized through exfoliation and a hydrothermal chemical cutting method. Then, 1.5 mL of QD suspension was added to 1.5 mL of 0.01 M PBS (pH: 7.5), followed by the mixing of QC into the above solution. After this, the obtained mixture was excited at 365 nm and the emission spectral response was recorded from 390 to 600 nm	25–600 nM	1.35 nM	Food samples	212
2	Dopamine (DA)	N-MXene QDs	Fluorescence	These QDs were synthesized through a two-step acid refluxing and hydrothermal method. For dopamine sensing assays, 100 μL of N-MXene QD suspension (1 mg mL^{-1}) was mixed thoroughly with 900 μL of PBS (pH: 7.4). Then the fluorescence intensity was recorded. The developed probe showed high sensitivity and selectivity	20–100 nM	18 nM	NA	213
3	Ascorbic acid (AA)	N-MXene QDs	Fluorescence	These QDs were synthesized through exfoliation and chemical cutting, employing a solvothermal route. Then, different concentrations of AA solution were mixed with 0.6 mM of Ce^{4+} in Tris-HCl buffer (0.1 M, pH: 7.0) and incubated at 37 °C for 30 min. After this, 0.5 mM of o-PD was added to the above mixture, followed by mixing with 0.15 mg mL^{-1} N-MXene QDs. After incubation, the mixture was subjected to fluorescence measurements at an excitation wavelength of 380 nm	2–240 μM	0.82 μM	Human serum	214
4	Ascorbic acid	N-MXene QDs	Fluorescence	These QDs were synthesized employing an exfoliation and solvothermal approach. For the fluorescence determination of AA, 0.5 mM Cr(iv) was mixed with PBS (10 mM, pH: 6), and then 0.1 mg mL^{-1} N-MXene QDs was introduced to the above solution. This nanoprobe was deployed for fluorescence measurements from 380–600 nm with an excitation wavelength of 360 nm	0.1–500 μM	0.02 μM	Vitamin C tablets and lemon juice	215
5	Hypochlorite	MXene QDs	Dual-channel naked-eye colorimetry and fluorescence	These MXene QDs were synthesized through HF exfoliation and ultrasonication chemical cutting methods. For ClO$^-$ determination, MXene QDs were mixed with 1 mM curcumin and different concentrations of ClO$^-$ and diluted to 2 mL. Then fluorescence measurements were carried out at an excitation wavelength of 330 nm	25–150 μM	5 μM	NA	216
6	Curcumin	MXene QDs	Fluorescence	These MXene QDs were synthesized through HF exfoliation and ultrasonication chemical cutting methods. For sensing, different concentrations of curcumin (0.05–10 μM) were mixed with MXene QDs (1 mg mL^{-1}, 200 μL) and diluted to 2 mL with deionized water. Then fluorescence spectra were recorded at an excitation wavelength of 330 nm	0.05–10 μM	20 nM	NA	216
7	Alizarin Red (ARS)	N-MXene QDs	Fluorescence	N-MXene QDs were synthesized through HF exfoliation and solvothermal treatment, employing o-phenylenediamine as a doping agent. The obtained powder was mixed with methanol for further use. In a typical sensing procedure, 200 μL of N-MXene QD suspension was mixed with different volumes of ARS (2 × 10^{-3} mol L^{-1}) and then diluted to 10 mL with Tris buffer. Finally, the fluorescence response of the probe was recorded at an excitation wavelength of 420 nm	0–80 μM	1.21 μM	Water samples	217

Table 1 (Contd.)

No.	Target	Probe composition	Detection technique	Fabrication method	LDR	LOD	Real sample	Ref.
8	Xanthine	N-MXene-QDs@DAP	Photoluminescence	These QDs were synthesized through exfoliation with DMF, ultrasonication, and hydrothermal treatment at 120 °C for 6 h. For typical sensing, 150 μL of different concentrations of xanthine was added to a previously prepared mixture containing 200 μL of PBS (10 mM, pH: 7.4), 190 μL of 40 mM o-PD, 10 μL of xanthine oxidase (100 μg mL^{-1}), and 10 μL of HRP (8 U mL^{-1}). Then, the fluorescence of the final probe was recorded	1–50 μM	0.34 μM	Human serum	218
9	H$_2$O$_2$			In a typical sensing procedure, different concentrations of H$_2$O$_2$ (10 μL) were added to a previously prepared mixture containing 10 μL of HRP (8 U mL^{-1}), 190 μL of 40 mM o-PD, and 50 μL of PBS (10 mM, pH: 7.4), with incubation for 50 min at 37 °C. Then 40 μL of N-MXene QDs was added to obtain the N-MXene QDs@DAP probe. Then it was deployed for fluorescence measurements	2–50 μM	0.57 μM	Human serum	218
10	D-Penicillamine (D-PA)	N-MXene QDs	Fluorescence	These MXene QDs were synthesized through a hydrothermal method. In a typical sensing procedure, different concentrations of D-PA were added to 300 μM Cu^{2+} solution and 0.1 M Tris-HCl buffer (pH: 7). Then 50 mM o-PD and 15 μL of N-MXene QDs were dropped into the above mixture. Following this, the fluorescence signal of the final sensor probe was measured at an excitation wavelength of 380 nm	0.34–670 μM	6.9 nM	D-PA tablets	219

of Ti$_3$C$_2$ NPs was observed in the supernatant. Then, 2 mL of Ti$_3$C$_2$ NPs was taken in a Teflon-lined stainless-steel autoclave with 25 mL of distilled water, 50 mg of GSH was added to the above mixture, and the pH was set to 8 by adding NaOH. Finally, the hydrothermal reaction was carried out at 120 °C for 12 h in an oven. The resulting black suspension was removed using a 0.22 μm porous membrane. The obtained colloidal suspension was further dialyzed through a 500 Da dialysis bag for 24 h to obtain GSH-MXene QDs. The obtained mixture was treated with a rotatory evaporator and vacuum dried at 60 °C for 12 h, and then the final GSH-MXene QD powder was obtained; it was stored at 2–8 °C for further use. The analytes were detected by using these GSH-MXene QDs. Here, different concentrations of uric acid were mixed with a constant volume of uricase enzyme and then stabilized for 30 min at 37 °C. Then, aliquots of a GSH-MXene QD (100 μL; 0.5 mg mL^{-1}) suspension, o-phenylenediamine (OPD), and horseradish peroxidase were added to the mixture; after this, 2 mL of PBS (10 mM, pH 7.2–7.4) was added into each and they were properly mixed at 37 °C. Following this, fluorescence emission spectra were recorded, and it was observed that with increasing uric acid concentration, the emission at 430 nm from GSH-MXene QDs was quenched progressively and emission from oxOPD at 568 nm increased progressively. This probe was used to distinguish the color change and a LOD of 125 nm was reported with an LDR of 1.2–75 μm; this is commonly known as a "naked-eye" colorimetric and ratiometric fluorescence sensor, as illustrated in Fig. 7. Another study by Karimi et al. proposed a MXene-QD-based novel sensor probe for uric acid detection.[223] They synthesized it through a combination of sonication and hydrothermal methods. Employing the chemiluminescence properties of the produced QDs, they proposed a LDR of 0.15–2.5 μM with a LOD of 0.093 μM.

4.1.2. MXene-based glutathione acid sensors. Glutathione is a free-radical scavenger, and it is categorized as an important antioxidant which plays a vital role in the maintenance of cellular activity.[224] An abnormal concentration of GSH in cells may contribute to various diseases or conditions, like cardiovascular disease, Alzheimer's, cancer, and aging.[225,226] Therefore, its detection becomes essential for the assessment of cell condition and overall health. A study by Luo et al. proposed N-doped MXene QDs for glutathione detection.[227] They synthesized them through traditional chemical exfoliation following a previously reported method. For N-doping, 0.1 g of 2D MXene sheets was mixed with 20 mL of ultra-pure water and this was centrifuged for several hours. Then, 2 mL of ethylenediamine was added to the above mixture and it was transferred to a Teflon-lined stainless-steel autoclave. The reaction was carried out at 160 °C for 12 h in an oven. Finally, the obtained mixture was filtered with a 220 nm membrane to get N-doped MXene QDs. Then, for the detection of GSH, a 200 μg mL^{-1} N-doped MXene QD stock suspension and 200 μM Fe^{3+} stock solution was prepared. Then, 800 μL of N-doped MXene QDs and 200 μL of Fe^{3+} were taken from the prepared stock solution and used to probe different prepared concentrations of GSH. Emission spectra at an excitation wavelength of
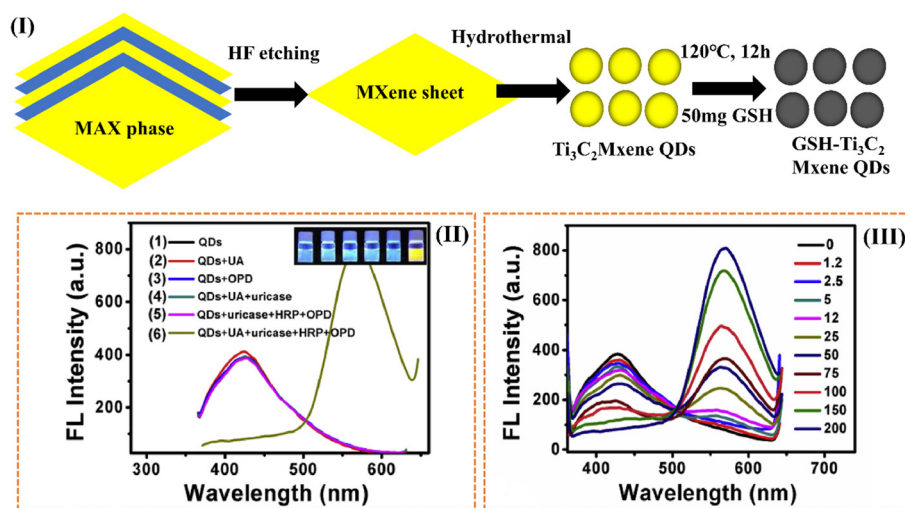
Fig. 7 (I) A schematic representation of GSH-MXene QD synthesis employing etching and hydrothermal treatment, highlighting the surface-functionalized photoluminescent MXene QDs. (II) Fluorescence spectra of GSH-Ti$_3$C$_2$ MXene QDs demonstrating the stepwise response of the (1) QDs, (2) QDs with uric acid (UA), (3) QDs with o-phenylenediamine (OPD), (4) QDs with UA and uricase, (5) QDs with uricase, horseradish peroxidase (HRP), and OPD, and (6) QDs with UA, uricase, HRP, and OPD, where the full enzymatic cascade highlights the characteristic fluorescence enhancement. (III) Fluorescence spectra of GSH-Ti$_3$C$_2$ MXene QDs in the presence of UA at concentrations ranging from 0–200 μM, showing the concentration-dependent increase in fluorescence over a wide range. Reproduced with permission from ref. 222; copyright 2020, ELSEVIER.

350 nm were recorded using a fluorometer and a wide LDR of 0.5–100 μM was reported with a LOD of 0.17 μM, as illustrated in Fig. 8. Another study by Yang *et al.* proposed a novel sensor based on a MXene QDs–MnO$_2$ nanocomposite for the detection of glutathione.[228] They mixed 50 μL of QDs with 150 μL of MnO$_2$ nanostructures in 25 mM HEPES [[(4-2-hydroxyethyl)
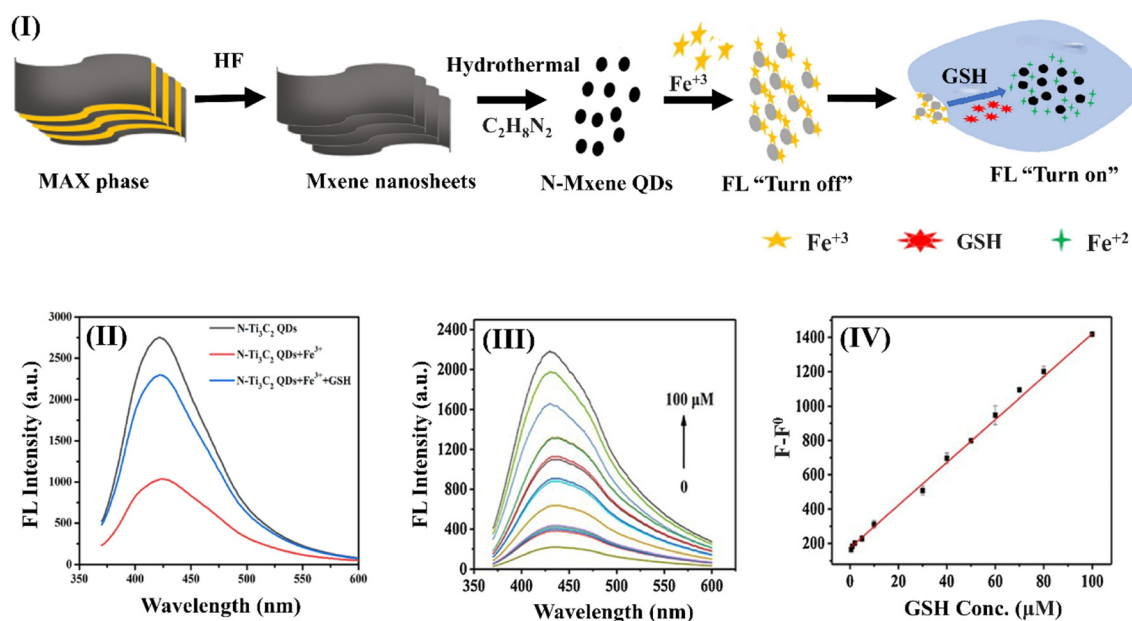
Fig. 8 Schematic illustrations of MXene QD synthesis and their fabrication into a sensor setup. (I) A schematic representation of the development of an N-MXene QDs + Fe^{3+} fluorescence sensor probe for GSH detection; the probe was constructed using the coordination interactions between N-MXene QDs and Fe^{3+}, offering fluorescence quenching. The introduction of GSH potentially disrupts the coordination interactions between N-MXene QDs and Fe^{3+}, restoring the fluorescence quenching due to strong chelation between GSH and Fe^{3+}, enabling a turn-on sensing mechanism. (II) Fluorescence spectra of N-MXene QDs (black line), N-MXene QDs + Fe^{3+} (blue line), and N-MXene QDs + Fe^{3+} + GSH at an excitation wavelength of 350 nm, highlighting the fluorescence recovery of the sensor probe in the presence of GSH. (III) Fluorescence spectra of N-MXene QDs/Fe^{3+} with different concentrations of GSH from 0–100 μM, demonstrating the concentration-dependent fluorescence recovery. (IV) Linear fitting of the fluorescence intensity $F - F_0$ *versus* GSH concentration (0.5–100 μM), showing quantitative detection and the high sensitivity of the sensor probe with a good LDR. Reproduced with permission from ref. 227; copyright 2021, ELSEVIER.

piperazine-1-ethane sulphonic acid] buffer. Then, different amounts of GSH standard solution were added into the above mixture and reacted for 30 min at room temperature. Then fluorescence spectrum of each sample was recorded at a wavelength of 330 nm, and a highly sensitive sensor with a LOD of 20 nM was proposed.

4.1.3. MXene-based histidine sensors. Histidine is considered among the nutritionally essential amino acid precursors for several hormones (like thyrotropin-releasing hormones) and key catalytic residues in many enzymes.[229,230] It also acts as an antioxidant, anti-inflammatory, and antisecretory agent.[231] Therefore, it is required in appropriate quantities for normal function, and any irregularities in its metabolism can lead to various disorders related to the lungs, liver, kidneys, blood, and skin. Its real-time monitoring is crucial for human health. For this, Ai et al. developed a novel MXene-QD-based sensor probe for the detection of histidine employing fluorescence methods.[91] They mixed 10 mL of 40% HF with Ti_3AlC_2 powder and mixed this thoroughly at 60 °C for 24 h using a magnetic stirrer. The obtained mixture was washed multiple times till the pH reached 6–7 and then the pellet was dried at 80 °C for 24 h. This powder was mixed with 10 mL of distilled water in a N_2-protected environment and sonicated for 30 min, and then 10 mL of $NH_3 \cdot H_2O$ was added to the above mixture. The entire mixture was transferred into a Teflon-lined stainless-steel autoclave and the reaction was carried out at 120 °C for 6 h. After this, the reaction mixture was dialyzed (M_w: 2000 Da) for 1 h to remove surplus ammonia. Then, this obtained mixture was centrifuged at 12 000 rpm for 30 min, the pellet was discarded, and the supernatant was filtered with a 100 nm membrane to obtain MXene QDs. For the detection of histidine, they developed a Ni-based MXene QD sensing probe. First, they measured the changes in the FL intensity for the entire system over time. They observed a sudden remarkable change after adding Ni; within 30 s, the FL of the MXene QDs was quenched rapidly and it became stable in about 10 min. When the suspension stabilized completely, they added histidine, and the fluorescence of MXene QDs recovered instantly and stabilized within 15 min. They concluded that the addition of different substances results in a change in the FL of MXene QDs, moving from quenching to recovery. They also reported the FL intensity recovery of MXene QDs upon increasing the concentration from 100–1000 nM, with a histidine detection limit of 2.1 nM, as shown in Fig. 9. They examined the fluorescence lifetime, the sensor response to different concentrations of histidine, and the response in the presence of potential interfering molecules, showing the importance of the sensor for monitoring different diseases.

4.1.4. MXene-based sensors for tetracycline. Tetracycline is a broad-spectrum antibiotic widely employed in human healthcare and veterinary medicine, owing to its broad-spectrum antibacterial effects, moderate price, and hypotoxicity.[232,233] However, the casual use of these antibiotics may lead to their accumulation in the environment.[234] Through interconnected ecological food chains, it may enter

the human body and have adverse effects on human health, including gastrointestinal damage, allergic reactions, and antibiotic resistance.[235] To ensure public health safety, researchers have explored newer approaches for the sensitive and efficient detection of tetracycline. Recently Bai et al. developed a B,N-doped MXene QD-based novel fluorescence sensing probe for the point-of-care detection of tetracycline.[236] They synthesized 2D MXene sheets through HF treatment followed by the chemical cutting and chopping of these nanosheets via one-step hydrothermal treatment at 100 °C for 12 h. Then, a 220 nm microporous membrane was used to filter the supernatant, and the final powder was obtained through a freeze-drying method and stored at 2–8 °C for further use. Then, after drying, they loaded N,B-doped MXene QDs (0.5 mg mL^{-1}) onto small paper strips using 2–3 cycles. Then they made mixtures of 30 µL of $EuCl_3 \cdot 6H_2O$ (2 mM) and different concentrations of tetracycline (0–20 µM); after this, 20 µL of these mixtures were applied to different strips. These sensor strips were deployed for the detection of tetracycline at 365 nm and a LOD of 20 nM was reported. Another study by Nguyen et al. proposed a novel nitrogen-doped MXene QD-based sensor probe for the ultrasensitive detection of tetracycline.[237] They mixed 900 µL of 5 µg mL^{-1} MXene QDs with 100 µL of tetracycline solution at different concentrations and then fluorescence detection was carried out at an excitation wavelength of 310 nm; a LDR of 0.50–300 µM and a LOD of 24 nM were proposed.

4.2. Sensing of macromolecules

Macromolecules like nucleic acids, lipids, proteins, and carbohydrates are categorized as the building blocks of living beings. They play a vital role in the maintenance of the structure and function of living cells, as they are required in appropriate concentrations; any significant deviation may cause severe malfunctioning.[238] This creates a niche for developing miniaturized, portable, and affordable sensing platforms for the detection of these molecules. There are numerous large molecules for which MXene-QD-based sensors have been developed, some of which are described here, including TNBC, MUC1, polynucleotide kinase, and alkaline phosphatase. Others are discussed in Table 2, which covers sensor fabrication strategies, limits of detection (LODs), linear detection ranges (LDRs), synthetic routes, real sample use, and the detection techniques involved in sensor development in those studies.

4.2.1. MXene-based sensors for triple-negative breast cancer. Triple-negative breast cancer (TNBC) is a heterogenous sub-type of breast cancer.[244] Based on immunohistochemistry, TNBC is a progesterone receptor, an estrogen receptor, and human epidermal growth factor receptor 2 (HER2) negative.[245] It accounts for more than 10% of the total breast cancer cases and predisposes adverse outcomes with reduced survival rates.[246] In this complicated disease, several biomarkers can be beneficial from a clinical perspective and can be employed for early detection. A study by Nie et al. constructed a sensing platform for the detection of TNBC employing a MXene QDs
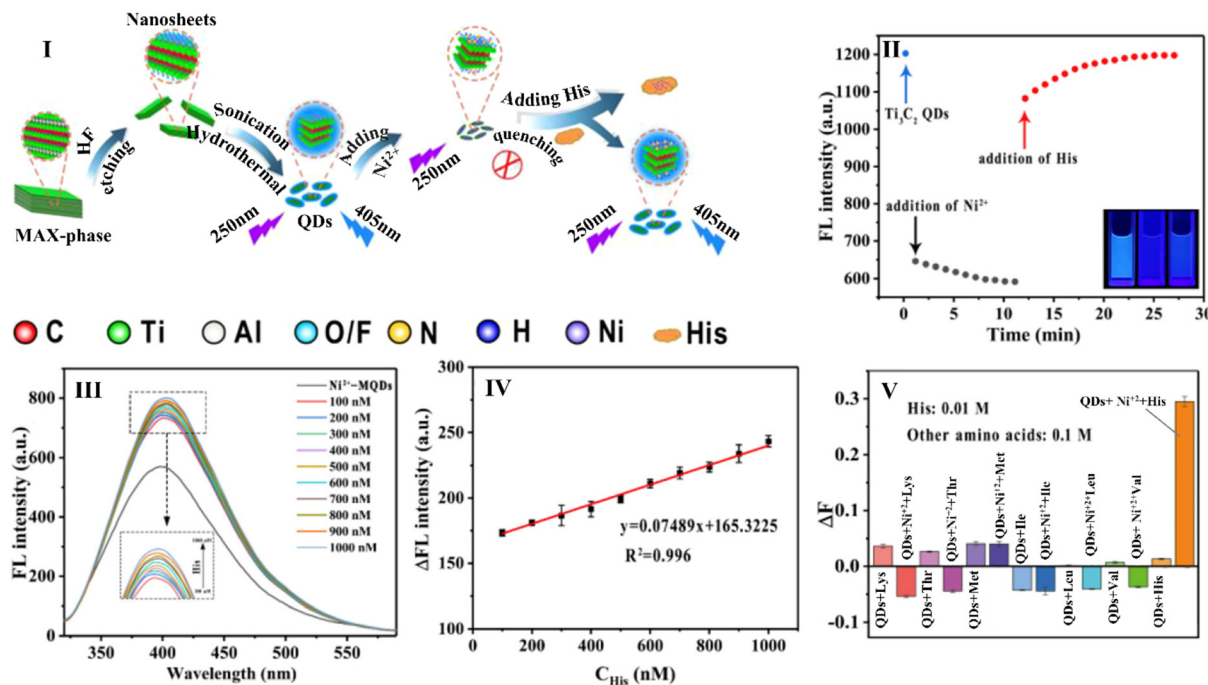
Fig. 9 Schematic representations of MXene QD synthesis and their deployment for histidine detection. (I) A schematic illustration of MXene QD synthesis and the signal transduction mechanism when employing the Ni^{2+}-modulated Ti_3C_2 QD-based photoluminescence sensor for histidine detection, where Ni^{2+} coordinates with the surface terminations of MXene QDs causing fluorescence quenching. Fluorescence can be restored upon the introduction of histidine to the sensor probe due to the disruption of coordination between MXene QDs and Ni^{2+}, resulting in a fluorescence recovery (turn-on) sensing mechanism. (II) Time-dependent FL intensity of MQDs upon addition of Ni^{2+} and histidine at 410 nm; in the inset MQDs, Ni^{2+}–MQDs, and His@Ni^{2+}–MQDs solution under 365 nm is represented from left to right. (III) The fluorescence response of MXene QDs to different concentrations of histidine (100–1000 nM). (IV) The ΔFL calibration curve of the MQD solution *versus* the concentration of histidine, indicating the sensitive and stable response of the sensor probe. (V) The ΔF values at 410 nm for the MXene QDs in the presence of various metal ions, confirming that the sensor probe showed a highly selective response. Reproduced with permission from ref. 91; copyright 2021, ACS Publications.

@gold nanobones (AuNBs) heterostructure.[241] For this, Ti_3AlC_2 powder (300 mg) and NaOH (15 M) solution were mixed properly and then transferred to a microwave for further reaction at 180 °C for 1 h. Then the reaction mixture was centrifuged and washed with distilled water till the pH reached 7. The obtained pellet was mixed with tetramethylammonium hydroxide (TMAOH, 25%) and stirred at room temperature (RT) for 2 days. The reaction mixture was centrifuged and the obtained green supernatant was collected and placed again into a microwave at 110 °C for 1 h. Following this, it was further centrifuged to remove larger particles, and then the solution was placed at 200 °C to remove TMAOH. The obtained MXene QDs and AuNBs were mixed to obtain the MXene QDs@AuNBs heterostructure. Then it was fabricated over an amino-functionalized MnO_2 nanosheet-modified GCE surface. This sensor probe was deployed for the sensing of miRNA-26a and a wide LDR of 5 fM–10 nM was reported with a very low LOD of 1.7 fM. Another study by Li *et al.* proposed a novel GSH-capped MXene QD-based ECL sensor for the detection of miRNA-221 in TNBC.[247] They synthesized GSH-MXene QDs using microwaves and biomimetic magnetic vesicles-hairpin DNA over a magnetic glassy carbon electrode. Then this biomimetic magnetic vesicles-hairpin DNA was incubated with

different concentrations of miRNA221 (6 μL) at 37 °C for 30 min. Following this, the ECL signal was recorded in the range of 0 to −1.6 V and a LDR of 10 fM–10 nM and LOD of 10 fM were proposed, as illustrated in Fig. 10.

4.2.2. MXene-based sensors for MUC1. MUC1 is a heavily glycosylated high-molecular-weight protein.[248] It is a membrane-associated glycoprotein abnormally overexpressed in the majority of adenocarcinomas, *e.g.* in most lung, prostate, pancreatic, and epithelial ovarian cancers.[249] It has been heavily explored as a potential biomarker for the diagnosis of human cancers.[250] A study by Jiang *et al.* synthesized N-doped MXene QDs using Ti_3AlC_2 based on their previously reported work.[242] Then, AgPt nanospheres were synthesized and resuspended in 10 mL of distilled water. Further, 1 mL of these nanospheres was poured onto different concentrations of N-doped MXene QDs, and a reaction was carried out at room temperature for 24 h to obtain AgPt@N-MXene QDs. Then the reaction mixtures were centrifuged and pellets were resuspended in 1 mL of distilled water, before being further mixed with 150 μL of anti-MUC1 followed by overnight stirring at 4 °C. This led to the formation of the AgPt@N-MXene QDs–anti MUC1 probe (having Ag–N and Pt–N bonds), which was then mixed with 100 μL of BSA (1%) solution and stirred for 2 h to block all

Table 2 A comprehensive overview of sensor fabrication methods, LDRs and LODs with real sample consideration for macromolecule detection

| No.	Target	Probe composition	Detection technique	Fabrication method	LDR	LOD	Real sample	Ref.
Macromolecules								
1	Cytochrome-c	ε-Poly-L-lysine (PLL) decorated MXene QDs	Fluorescence	MXene QDs were synthesized through HF exfoliation and ultrasonication. Then they were decorated with PLL employing a hydrothermal method. For sensing, different concentrations of Cyt-c (0.2–40 μM) were mixed with 100 μL of PLL-decorated MXene QDs (1 mg mL^{-1}) and the solution was diluted to 2 mL with deionized water. After this, fluorescence spectra were recorded at excitation and emission wavelengths of 330 nm and 415 nm, respectively	0.2–40 μM	20.5 nM	Human serum sample	239
2	Trypsin	ε-Poly-L-lysine (PLL) decorated MXene QDs	Fluorescence	MXene QDs were synthesized through HF exfoliation and ultrasonication routes. Then they were decorated with PLL employing a hydrothermal method. To sense trypsin, 0.4 mL of Cyt-c (200 μM) was mixed with different concentrations of trypsin and then 0.1 mL of tris-HCl (10 nM, pH: 8) was added to each mixture before dilution to 2 mL. The fluorescence spectra from the final probe were recorded with excitation and emission wavelengths of 330 nm and 415 nm, respectively	0.5–80 μg mL^{-1}	0.1 μg mL^{-1}	Human serum sample	239
3	Alkaline phosphatase (ALP)	MXene QDs	Fluorescence	MXene QDs were synthesized through exfoliation and hydrothermal chemical cutting. For a typical sensing procedure, ALP with activity ranging from 0–50 U L^{-1} was added to 1 mL of a previously prepared reaction mixture (Tris-HCl, 50 mM, pH: 10) containing 200 μM p-NPP and 0.1 μM MgSO$_4$. After 30 min of incubation at 37 °C, fluorescence spectra were recorded at an excitation wavelength of 365 nm	0.1–2 U L^{-1}	0.02 U L^{-1}	Biological sample	240
4	Cancer	MXene QDs@Au nanobones	Electrochemiluminescence	MXene QDs were synthesized through NaOH etching using microwaves. Then, the precipitate was mixed with TMAOH solution and, after incubation, it was placed at 200 °C for its removal. Then, Au-nanobones were mixed with the obtained MXene QDs. Then, MnO$_2$ nanosheets were prepared. For a typical sensor, a MXene QDs@Au nanobones-modified GCE was used for impedance measurements employing miRNA-26a; following this, MnO$_2$ nanosheets were applied to the previously modified GCE. Then impedance signals were measured again and compared with the previous ones to obtain the final values	5 fM–10 nM	1.7 fM	Patient serum sample	241
5	Mucin 1	N-MXene QDs	Electrochemiluminescence	MXene nanosheets were prepared through HF etching followed by nitric acid treatment over an oil bath. Then, the obtained powder was treated hydrothermally to obtain MXene QDs. These QDs were conjugated with silver platinum nanospheres followed by several modifications to obtain AgPt@N-MXene QDs-anti-MUC1-BSA conjugates. Then, a GCE was modified with AuNPs followed by several steps using an ECL platform to develop BSA/anti-MUC1/DpAu/GCE. In a typical sensing procedure, different concentrations of the target MUC1 were drop-casted over the modified electrode; subsequently, the previously prepared conjugate was applied over the modified electrode surface. Finally, the ECL signal was recorded using the final sensor probe	1 fg mL^{-1}–1 ng mL^{-1}	0.31 fg mL^{-1}	Human serum	242
6	SARS-CoV-2	Nb$_2$C-SH QDs	SPR	Nb$_2$C QDs were synthesized through a solvothermal approach, then dropped over a gold chip surface, forming a uniform layer through Au–S bonds via self-assembly interactions. Following this, they were incubated with aptamers for 30 min, and then washed with running buffer to remove unbound aptamers. Then, SPR flow cells were deployed for the sensing of the N-gene of SARS-CoV-2	0.05–100 ng mL^{-1}	4.9 pg mL^{-1}	Human serum and sea water	243
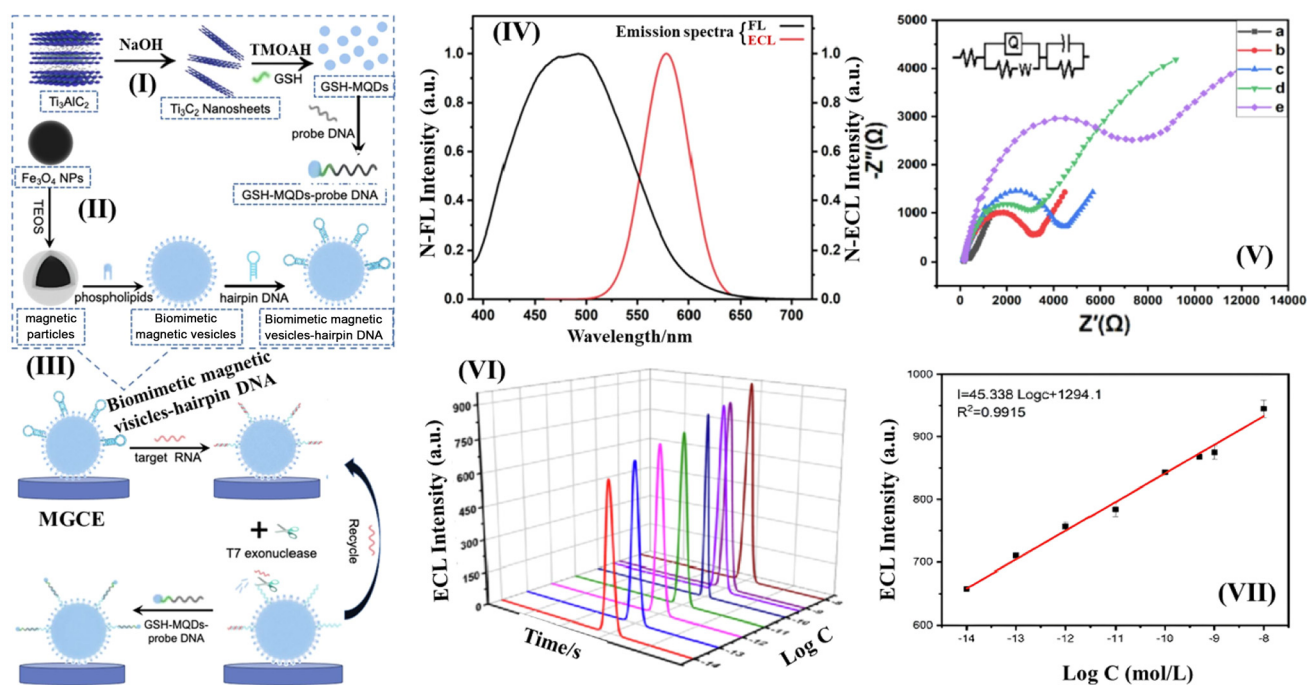
Fig. 10 Schematic illustrations of a GSH-MXene-QD-based sensor for TNBC detection. (I) A schematic representation of GSH-capped MXene QD synthesis and their subsequent combination with probe DNA for targeted nucleic acid recognition. (II) A schematic representation of biomimetic magnetic vesicles for enhanced target capture by mimicking cellular vesicles. (III) The ECL sensing of miRNA-221 employing biomimetic magnetic vesicles with GSH-MXene QD-probe DNA; this assay employs hybridization-triggered T7 exonuclease-assisted signal enhancement, improving the selectivity and sensitivity of the sensor probe. (IV) Optical characterization of the sensor probe (GSH-MXene QDs), showing both FL (black line) and ECL (red line) emission spectra, highlighting the dual-mode signal capabilities of the probe. (V) Electrochemical impedance spectroscopy analysis of (a) a bare GCE, (b) a GCE with biomimetic magnetic vesicles-hairpin DNA, (c) GCE/biomimetic magnetic vesicles-hairpin DNA/miRNA-221, (d) GCE/biomimetic magnetic vesicles-hairpin DNA/miRNA-221/T-7 exonuclease, and (e) GCE/biomimetic magnetic vesicles-hairpin DNA/miRNA-221/T-7 exonuclease/GSH-MXene QDs-probe DNA, confirming the successful functionalization of the surface. (VI) The relationship between ECL intensity and miRNA-221 concentration, highlighting the concentration-dependent ECL signal enhancement. (VII) The corresponding linear fitting for miRNA-221 detection, enabling quantitative detection with high sensitivity. Reproduced with permission from ref. 247; copyright 2022, ELSEVIER.

remaining active sites. Following this, the mixture was centrifuged at 10 000 rpm at 4 °C for 10 min to remove all unreacted species. Then, the finally obtained AgPt@N-MXene QDs–anti MUC1–BSA bioconjugate was dispersed in PBS and stored at 4 °C. An electrochemiluminescence (ECL) sensor was constructed using a sandwich format. Then a polished GCE was dipped in HAuCl$_4$ (2 mL, 1%) solution to synthesize gold nanoparticles on the GCE electrode surface using a potentiostat at −0.2 V (30 s). After this, 20 μL of primary anti-MUC1 was dropcasted on the modified Au/GCE surface (abbreviated as anti-MUC1/Au/GCE) which was then washed thoroughly. Following this, 20 μL of 1% PBS was used for coating and this was dried for 45 min at room temperature. Finally, a BSA/anti-MUC1/AuNPs/GCE sensor probe was obtained. Following this, 20 μL of MUC1 was drop-casted over the previously modified electrode surface, then 20 μL of AgPt@N-MXene QDs–anti MUC1–BSA was drop-casted, followed by 45 min of drying at room temperature, with washing after each fabrication step. This led to the formation of a sandwich-like structure over the electrode surface. Finally, this probe was deployed for sensing, and an electrochemiluminescence signal was recorded using an ECL analyzer in 2 mL of PBS containing 10 mM S$_2$O$_8$$^{2-}$ by applying

a potential from −2 V to 0 V. Through this experiment, they concluded that as the concentration of MUC1 increases, the ECL signal also increases. They reported a LDR of 1 fg mL^{-1}–1 ng mL^{-1} and a LOD of 0.31 fg mL^{-1}. As the MUC1 concentration increased, binding to AgPt@N-MXene QDs–anti MUC1–BSA bioconjugates immobilized on the electrode surface also increased, which caused the increase in the ECL signal, as illustrated in Fig. 11.

4.2.3. MXene-based sensors for polynucleotide kinase. Polynucleotide kinase (PNK) acts as a catalytic agent, and it is essential for ligation-based DNA repair.[251] PNK transfers the γ-phosphate residue to the 5′-end and it is replaced by 5′-OH from the damaged DNA. It plays a very essential role in phosphorylation-dependent DNA repair and is critical for nucleic acid metabolism.[252] As it plays a very essential role, any abnormality in the synthesis and expression of PNK may lead to irregularities in the DNA damage repair system which will lead to the development of various diseases and conditions related to the central nervous system, cardiovascular system, *etc.*[253,254] Therefore, the detection of PNK is very important from a clinical perspective. A study by Zhang *et al.* reported a highly sensitive and selective probe for the detection of
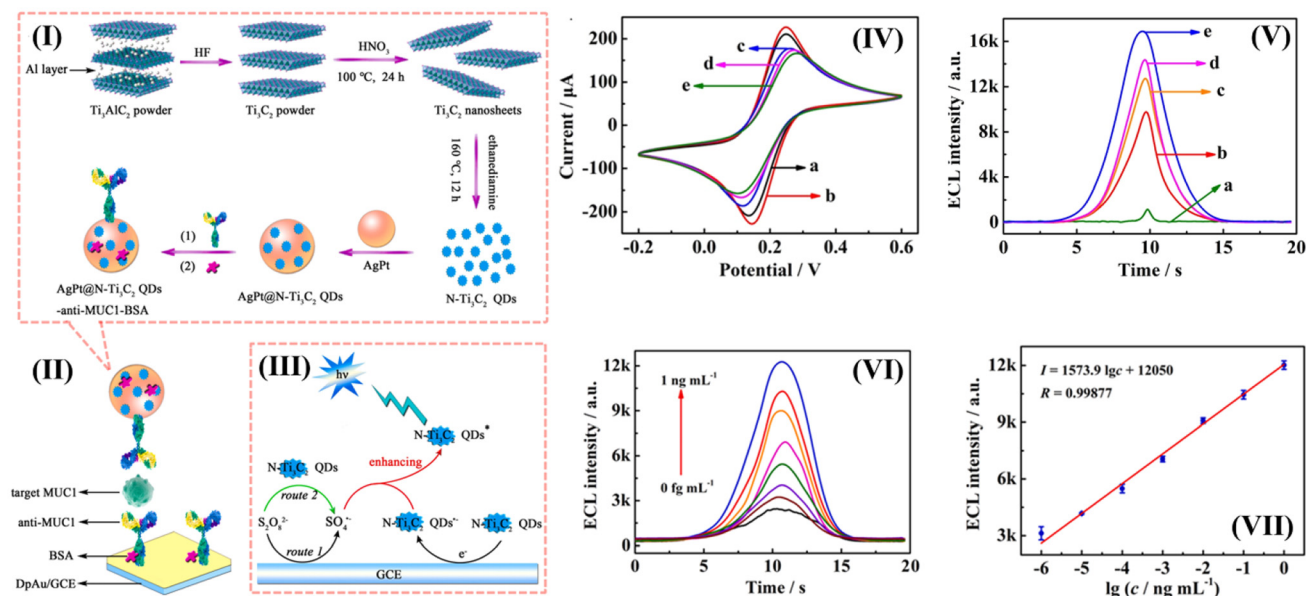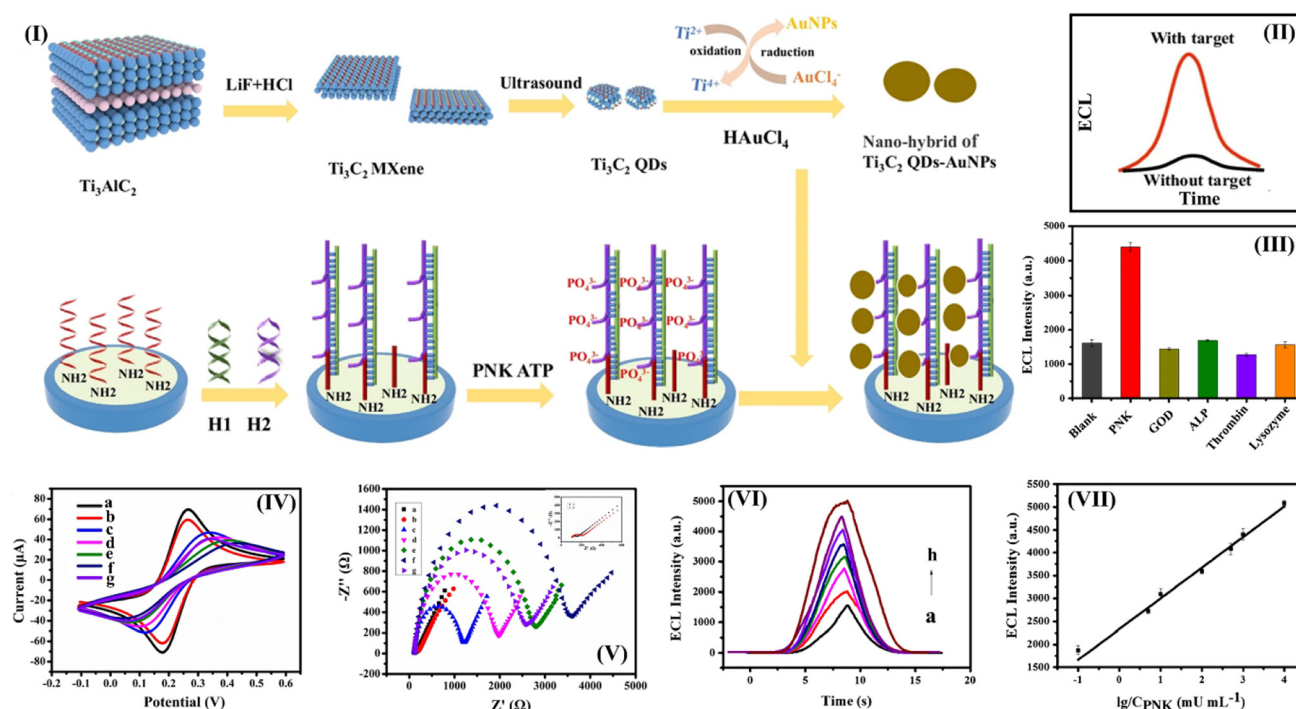
Fig. 11 Schematic representations of a MXene-QD-based ECL sensor probe for MUC1 detection. (I) The synthesis of AgPt@N-MXene QDs-anti-MUC1-BSA bioconjugates, where N-MXene QDs are combined with bimetallic AgPt nanoparticles and then conjugated with anti-MUC1 antibodies to obtain a highly selective ECL sensor probe. (II) The development of the ECL immunosensor. (III) The possible ECL mechanism of the N-MXene QDs/$S_2O_8^{2-}$ system; here MXene QDs act as luminophores in the presence of the co-reactant potassium persulphate, producing significantly enhanced luminescence *via* intermediate generation. (IV) The CV response of each modified electrode: a bare GCE (a), DpAu/GCE (b), anti-MUC1/DpAu/GCE (c), BSA/anti-MUC1/DpAu/GCE (d), and MUC1/BSA/anti-MUC1/DpAu/GCE (e), confirming the step-by-step modification of the sensor probe. (V) A comparison of ECL responses after each modification of the sensor showing the ECL intensities of (a) N-Ti$_3$C$_2$ QDs in PBS solution, (b) N-Ti$_3$C$_2$ QDs in $S_2O_8^{2-}$ solution, (c) N-Ti$_3$C$_2$ QDs in $S_2O_8^{2-}$ solution with Ag nanoparticles, (d) N-Ti$_3$C$_2$ QDs in $S_2O_8^{2-}$ solution with Pt nanoparticles, and (e) N-Ti$_3$C$_2$ QDs in $S_2O_8^{2-}$ solution with AgPt nanoparticles, which demonstrates the highest ECL response due to the synergistic effect of bi-metallic AgPt nanoparticles. (VI) The ECL responses of the fabricated immunosensor to various concentrations of MUC1, highlighting the concentration-dependent increase in the ECL signal due to antigen−antibody interactions. (VII) The calibration plot of the developed sensor for MUC1 detection, representing the sensitivity and stability of the sensor probe. Reproduced with permission from ref. 242; copyright 2022, ELSEVIER.

PNK.[255] They synthesized MXene QDs employing an *in situ* method using 0.8 g of LiF and 10 mL of HCl (9 mol L^{-1}), which was stirred for 5 min; then 0.5 g of Ti$_3$AlC$_2$ was added slowly and this was stirred for 24 h at 37 °C. Then the reaction mixture was centrifuged at 1280 RCF for 5 min and then several times at 3740 RCF for 15 min till the pH reached 6–7. The obtained solid precipitate was mixed with deionized water before further sonication and centrifugation at 1280 RCF for 1 h to get Ti$_3$C$_2$T$_x$ nanosheets in the supernatant. These nanosheets were sonicated for 10 h and centrifuged at 1289 RCF for 1 h, the pellet was discarded, and the supernatant was filtered with a 220 nm membrane to obtain MXene QDs. Following this, 1 mL of MXene QDs was mixed with 125 μL of HAuCl$_4$ and stirred for 15 min to obtain a MXene QDs–AuNPs nano-hybrid. At room temperature, sodium alginate (SA) 6 μL was drop-casted onto a polished GCE surface. Then this SA/GCE was activated at 37 °C with EDC and NHS (800 mM, 400 mM; v/v = 1 : 1) for 1 h, and then incubated in cDNA solution for 2 h at 37 °C. After this, cDNA/SA/GCE was immersed in PBS (37 °C) for 2 h to block all the non-specific sites. Then this cDNA/SA/GCE was modified at 37 °C with H1 (hairpin 1) and H2 (hairpin 2) to obtain H-cDNA/SA/GCE. Then a mixture of various concentrations of PNK and 1 mM ATP (v/v = 1 : 1) was drop-casted over the previously modified GCE surface and

incubated for 2 h at 37 °C. Finally, 40 μL of the MXene QDs–AuNPs nano-hybrid was drop-casted over the modified P-H-cDNA/SA/GCE. After each step, the electrode was cleaned with Tris-HCl and dried in a N$_2$ environment to remove all non-specific adsorbates. Then the ECL signal was measured in PBS (0.1 M, pH 7.4) containing 50 mM K$_2$S$_2$O$_8$. They reported a good LDR of 0.0001–10 U mL^{-1} and LOD of 2.7 × 10^{-5} U mL^{-1}, as illustrated in Fig. 12.

4.2.4. MXene-QD-based sensors for alkaline phosphatases. Alkaline phosphatase (ALP) is categorized among the hydrolases widely distributed in various tissues, including kidneys, liver, and bones.[256] It is an essential protein-based enzyme that catalyses the dephosphorylation of a wide range of substrates and also plays a very important role in bone mineralization and phosphate homeostasis.[257] It was extensively explored as a crucial biomarker for clinical diagnosis. An abnormal level of this enzyme is associated with various diseases and conditions including hepatitis, diabetes, and cancer.[258,259] Furthermore, a high level of ALP was used as a biomarker of pluripotent embryonic stem cells (ESC) in traditional diagnostics. This creates a niche for developing a miniaturized, point-of-care, affordable sensing setup for the clinical assessment of ALP. Guo *et al.* developed a MXene-QD-based fluorescence sensing setup for ALP detection in diverse

Fig. 12 Schematic representations of a MXene-QD-based ECL sensor for PNK detection. (I) The synthesis of the MXene QDs-AuNPs nanohybrid and its subsequent fabrication over an electrode surface; this nanohybrid combines the high electrical conductivity of MXene QDs and catalytic properties of AuNPs to form a robust, sensitive, and stable sensing probe. (II) A comparison of the ECL signals of the modified electrode without the target (black line) and with the target (red line), showing the target-induced ECL response of the sensor probe. (III) An evaluation of the selectivity of the developed biosensor in the presence of different interfering molecules such as 50 μM GOD, 10 U mL^{-1} ALP, 50 μM thrombin, and 50 μM lysozyme, and with the target molecule—1 U mL^{-1} PNK—which confirms that the developed probe was highly selective for PNK in the presence of respective interferant molecules. (IV) and (V) CV and EIS spectra of a bare GCE (a), SA/GCE (b), BSA/DNA/SA/GCE (c), H1 + H2/BSA/DNA/SA/GCE (e), P-H1 + H2/BSA/DNA/SA/GCE (f), and MXene QDs-AuNPs/P-H1 + H2/BSA/DNA/SA/GCE (g) in [Fe(CN)$_6$]$^{3-/4-}$ solution (pH 7.0) containing 0.1 M KCl. The inset of (V) shows EIS spectra of bare GCE (a) and SA/GCE (b). (VI) ECL curves for different concentrations of PNK: (a–h) 0, 0.0001, 0.001, 0.01, 0.1, 0.5, 1.0, and 10.0 U mL^{-1} in 0.1 M PBS (pH 7.4) with 50 mM K$_2$S$_2$O$_8$, which confirm that as the concentration of PNK increases, the ECL signal also increases respectively. (VII) A calibration plot for PNK detection, highlighting the linear relationship between the ECL signal and PNK concentration and demonstrating the high sensitivity and stability of the sensor probe. Reproduced with permission from ref. 255; copyright 2022, SPRINGER NATURE.

matrices.[260] They synthesized MXene 2D nanosheets through exfoliation followed by chemical cutting *via* hydrothermal treatment at 100 °C for 6 h. Then, the obtained reaction mixture was filtered through a 0.22 μm microporous membrane followed by the freeze-drying of the supernatant to finally obtain brown-colored MXene QDs. Then, these were poured into 1 mL of a reaction system containing Tris-HCl (50 mM, pH: 10.0), 200 μM *para*-nitrophenyl phosphate and 0.1 μM MgSO$_4$ and this was then incubated at 37 °C for 30 min. The obtained solution was deployed for the sensing of ALP based on the fluorescence spectra at 365 nm, and it showed a LOD of 0.02 U L^{-1}.

4.3. Sensing of environmental pollutants

The direct or indirect introduction of harmful and hazardous substances into the environment is categorized as environmental pollution. These pollutants have adverse impacts on the ecosystem, including on human and plant health, and they can be classified based on their chemical nature, source or persistence.[261] Exposure to these leads to various health com-

plications in humans and also contributes to a continuous loss of biological diversity over years through soil contamination.[262] Chemicals and pesticides used in or produced as byproducts of industrial processes, wastewater, agriculture, livestock, and petroleum-related industries are the main sources of such contamination.[263] Direct human exposure to such soil may cause short-term health complications, including coughing, chest pain, and irritation, headaches, and it can indirectly enter humans through absorption by plants and the interconnected ecological food cycle.[264] Environmental pollutants include a diverse range of molecules; however, in this section we comprehensively discuss MXene-QD-based sensors for heavy metals, metal ions, and pesticides.[265,266] Heavy metals usually include high-density metallic chemical elements that show toxicity or are poisonous at relativity low concentrations, including cadmium, mercury, arsenic, and lead as first-class hazards.[267] Apart from these hazardous metals, these days pesticides are extensively exploited and categorized as a major source of contaminants of emerging concern (CECs). The consumption of pesticides in 2019 was

reported to be 419 million metric tons, of which 1.76 million metric tons was consumed by China alone. Besides these factors, metal ions are also considered as a crucial concern relating to both the environment and health.[268] Metal ions are considered as fundamental and irreplaceable constituents of many critical biochemical pathways.[269,270] Despite their critical role, they have several disadvantages: excessive accumulation may lead to reactions and cause the deactivation of proteins and enzymes, and an absence of metal ions may lead to the inhibition of some biochemical pathways, ultimately leading to various diseases and conditions.[271,272] These factors are responsible for the categorization of metal ions as harmful substances. This creates a niche market for developing highly sensitive and miniaturized sensors for the real-time monitoring and management of these heavy metals, metal ions, and pesticides. Owing to their good optoelectronic and fluorescence properties, MXene QDs have been employed as a promising platform for sensing these contaminants. Here, we have reported MXene-QD-based sensors for the detection of mercury, copper, iron, cobalt, nitrite ions, and pirimiphos methyl. Others are discussed in Table 3 which covers sensor fabrication strategies, limits of detection (LODs), linear detection ranges (LDRs), synthetic routes, real sample analysis, and the detection techniques involved in sensor development in such studies.

4.3.1. MXene-QD-based sensors for mercury. Mercury is a naturally occurring element, symbolized as Hg, with an atomic number of 80; it is a high-density heavy metal commonly found in the Earth's crust and deposits of coal. As with other elements, there is a reservoir of mercury on the planet that cycles through the deep earth, the atmosphere, various water bodies and terrestrial reservoirs.[279,280] It is extensively used in paint, detonators for explosives, electrical apparatus, caustic soda, chlorine manufacturing, *etc.*, and it enters into the ecological cycle, including drinking water, through a variety of sources, such as atmospheric deposition, industrial discharge, and runoff from land.[281] Due to its hazardous effects, in 2007 the WHO set its threshold limit at 6 μg L^{-1} for drinking water.[282] Exposure or accumulation may cause significant damage to the brain, heart, kidneys, lungs, and immune and reproductive systems of animals, including humans, and high exposure may eventually cause death.[283] Therefore, the detection of mercury is crucial to reduce the health risk to humans. A study by Emami *et al.* developed a MXene-QD-based sensor probe for the detection of mercury ions in water bodies.[284] They synthesized MXene QDs through solvothermal–ultrasonication methods, and then the obtained powder was mixed with polyethyleneimine (PEI) and sonicated for 30 min. Then, the obtained reaction mixture was autoclaved in a PTFE-lined autoclave for 24 h at 120 °C, which wrapped the QDs over the positively charged PEI. Following this, 100 mg of the obtained mixture of MXene QDs–PEI was mixed with 50 mg of a previously prepared covalent organic framework and this was sonicated for 3 h. The obtained mixture was drop-casted over a pencil graphite electrode, leading to the formation of PGE/MXene QDs–PEI/COF for the sensitive detection of mercury.

They employed differential pulse anodic stripping voltametric techniques in 0.1 M HCl with an accumulation potential and time of −0.6 V and 100 s and proposed a LDR of 0.05–35 μM and LOD of 16 nM.

4.3.2. MXene-QD-based sensors for copper. Copper is a trace element and essential mineral that plays a very important role in oxygen transport, enzymatic function, and cellular transport. It is commonly found in environmental, industrial, and biological systems.[285,286] Due to its vital role in various environmental and physiological processes, 1–100 mg of copper are normally required by adults.[287,288] It is required in the body as an important catalytic co-factor, but free Cu ions in the body may damage cellular components. Cu salts are easily available chemicals in many countries. There are different sources of Cu consumption which are sometimes ignored and may lead to severe problems, such as accidental consumption based on contaminated water sources, Cu-salt-containing topical creams, and acidic food cooked in uncoated copper cookware.[289] Therefore, the detection of Cu ions is needed for monitoring and management. For this, MXene QDs have been employed by various researchers. A study by Feng *et al.* proposed novel N-doped MXene QDs for copper detection.[102] They synthesized these QDs using 0.12 g of pristine MXene in 250 mL of DMF followed by 12 h of sonication. Following this, centrifugation, resuspension and drying were carried out under vacuum at 45 °C for 8 h to obtain the final exfoliated MXene. Then different doses of amine were used for N-doping *via* solvothermal treatment, and N-MXene QDs with a size of ~6.2 nm and thickness of ~1 nm and having high fluorescence were synthesized. They were employed for the sensitive and selective detection of copper ions through fluorescence quenching, as illustrated in Fig. 13.

4.3.3. MXene-QD-based sensors for iron. Iron is categorized as an over-the-counter (OTC) multivitamin. Its accidental or intentional ingestion is a common form of poisoning.[290] Especially for children, acute ingestion is hazardous and deadly.[291] Failure to diagnose iron poisoning early may have serious consequences and lead to multi-organ failure and death.[292] This creates urgency for the efficient, accurate, and sensitive detection of iron for diagnostics and management purposes. In a study by Wang *et al.*, $Ti_3C_2T_x$ QDs (MXene QDs) were obtained from the precursor Ti_3AlC_2 *via* HF etching treatment, as per a previously reported method.[293] Following the etching treatment, the pellet was dried at 80 °C overnight. Then, they used an oil-bath reflux system to synthesize MXene QDs. For this, 100 mg of delaminated powder was added to 10 mL of an aqueous solution of 3% TMAOH, then oil-bath reflux was carried out at 120 °C for 72 h. Furthermore, the obtained reaction mixture was centrifuged at 12 000 rpm for 30 min and the pellet was discarded. MXene QD powder was obtained *via* vacuum drying the supernatant at 200 °C overnight. Different concentrations of Fe^{3+} (20 μL) were taken in different containers and then 2 mL of a 0.05 mg mL^{-1} solution of MXene QDs was added to each container. Then, finally, the fluorescence intensity of the sonicated solution was recorded at an excitation wavelength of 320 nm both in the absence of

Table 3 A comprehensive overview of sensor fabrication methods, LDRs, LODs, and real sample considerations for small-molecule detection

| No.	Target	Probe composition	Detection technique	Fabrication method	LDR	LOD	Real sample	Ref.
Environmental pollutants								
1	$Cr(IV)$	N-MXene QDs	Fluorescence	These QDs were synthesized employing exfoliation and solvothermal approaches. For the typical sensing of $Cr(IV)$, 80 μL of N-MXene QD suspension was mixed with 10 mM PBS (pH: 6). Subsequently, the fluorescence intensity was recorded at 440 nm (with an excitation wavelength of 360 nm). This probe showed highly sensitive measurements with a very good LOD	0.1–500 μM	0.012 μM	Water sample	215
2	Cr^{3+}	MXene QDs	Fluorescence	These MXene QDs were synthesized through a lye etching method. For a typical sensor, 100 μL of ionic solution was added dropwise to 2 mL of MXene QD suspension (0.015 mg mL^{-1}) and this was incubated in the dark for 1 min. Then, the fluorescence intensity of the final sensor probe was recorded at an excitation wavelength of 340 nm	NA	30 nM	Sewage disposal	273
3	Cu^{2+}	N,P-MXene QDs	Fluorescence	These nitrogen- and phosphorus-doped MXene QDs were obtained through a two-step stripping method including HF etching and strong acid reflux followed by hydrothermal cutting. For sensing, 300 μL of QDs was diluted to 3 mL with deionized water and the fluorescence intensity (F_0) was recorded. After this, different concentrations of Cu^{2+} were introduced into the above solution. Then, the fluorescence intensity (F_t) was recorded again	2–100 μM	2 μM	NA	274
4	Cu^{2+}	N-MXene QDs	Fluorescence	These QDs were synthesized through a hydrothermal process. For sensing, different concentrations of Cu^{2+} (10 μL) were mixed with o-PD solution (20 μL; 50 mM), and then 15 μL of N-MXene QD suspension was added. The mixture was transferred into Tris-HCl buffer and incubated for 3.5 h at 37 °C. Then fluorescence spectra were recorded	0.05–1000 μM	3 nM	Lake water and tap water	219
5	2,4-TNP	UA-MXene QDs	Fluorescence	Uric acid (UA)-capped MXene QDs were synthesized through a microwave-assisted synthesis route. In a typical sensing procedure, 1 mL of buffer solution of sodium carbonate and sodium bicarbonate (0.1 M) was mixed with different concentrations of TNP (0.01–300 μM) and then 100 μL of UA@MXene QDs (6.48 g L^{-1}) was added to each before dilution to 5 mL with deionized water. Then emission spectra of the final probe were recorded at an excitation wavelength of 360 nm	0.01–40 μM	9.58 nM	Environmental sample	275
6	Prostate-specific antigen (PSA)	MXene QDs	Photothermal	MXene QDs were synthesized through HF exfoliation followed by chemical cutting through ultrasonication. Then these QDs were entrapped in liposomes employing a film hydration method to obtain liposome-encapsulated MXene QDs. Then, these QDs were conjugated with anti-PSA mAb2 to obtain the final sensor probe. For a typical sensing procedure, an ELISA plate strip was coated with PSA-021 (mAb1) in 50 μL of PBST (10 mM PBS containing 0.05% Tween 20, pH: 7.4) and incubated overnight. It was washed with washing buffer and then incubated with blocking buffer. 100 μL of MXene QDs-encapsulated liposomes-linked mAb2 suspension was added to the above mixture which was deployed for photothermal detection	1–50 ng mL^{-1}	0.4 ng mL^{-1}	Human serum	276
7	Zn^{2+}	N-MXene QDs	Fluorescence	N-MXene QDs were obtained through exfoliation and ultrasonication methods. In a typical sensing procedure, 200 μL of N-MXene QDs (0.5 mg mL^{-1}) was mixed with 200 μM $Zn(II)$ (10 mM) in 3.6 mL of ultra-pure distilled[A44]water. After 1 min of incubation, fluorescence spectra were recorded at an excitation wavelength of 360 nm	0–20 μM	0.127 μM	Environmental sample	277

Table 3 (Contd.)

No.	Target	Probe composition	Detection technique	Fabrication method	LDR	LOD	Real sample	Ref.
8	Mn(VII)	MXene QDs	Fluorescence	These MXene QDs were synthesized through a one-pot hydrothermal route. In a typical sensing procedure, 20 μL of MXene QDs was dispersed in ultrapure water followed by the addition of 20 μL of Mn(VII) solution with different concentrations (0–20 μM). Then emission spectra of the probe were recorded at an excitation wavelength of 320 nm	0–1.7 μM	5.2 nM	Tap water	196
9	Ag$^+$	MXene QDs	Fluorescence	These MXene QDs were synthesized through HF etching and ultrasonication treatment. In a typical sensing procedure, different concentrations of Ag$^+$ (10 μL) were added to MXene QD suspensions and incubated at 25 °C for 1 h. Then fluorescence spectra of the probe were recorded	0–80 μM	0.45 μM	Tap water	278
10	Ni^{2+}	MXene QDs		These MXene QDs were synthesized through HF etching followed by hydrothermal cutting. For sensing, 200 μL of MXene QDs was diluted in 1 mL of deionized water. This was followed by the addition of different concentrations of Ni^{2+}. Then the final probe was deployed for fluorescence measurements	6–10 μM	3.52 nM	NA	91

Fe^{3+} (F_0) and in the presence of Fe^{3+} (F). They reported a LOD of 0.1–1.6 μM and a LOD of 2 nM. In another study, Xu *et al.* synthesized Ti$_3$C$_2$T$_x$ MXene nanosheets and the obtained powder was dispersed in 3 different solvents—DMF, ethanol, and DMSO—respectively, in a N$_2$ environment for 30 min to remove all interfering oxygen. Then, the final suspension was transferred into a PTFE-lined autoclave and a solvothermal procedure was carried out at 120 °C for 6 h in an oven. Following this, the obtained reaction mixture was centrifuged for 30 min at 12 000 rpm, then the pellet was discarded and the supernatant was stored as MXene QDs. They exhibit unique optical properties due to the different solvents offering different photoluminescence (PL) responses towards the different metal ions. The different metal ions show unique PL intensities towards the three different MXene QDs. They observed that the addition of iron causes a greater quenching effect on the PL intensity of f-MXene QDs compared to s-MXene QDs and e-MXene QDs. This PL quenching due to Fe occurs due to coordination between Fe and C=O groups on the surface of f-MXene QDs, while there is a low oxygen content in e-MXene QDs and no C=O in s-MXene QDs, as confirmed by XPS spectra. Thus f-MXene QDs are chosen for the sensitive and selective detection of iron, with a reported LOD of 2×10^{-6} M.

4.3.4. MXene-QD-based cobalt sensors. Cobalt and its derivatives are found in large quantities in nature (e-waste industry, mining, diamond industry, *etc.*), and cobalt biologically play an essential role in vitamin B$_{12}$ as a metal constituent.[294,295] Excessive exposure to cobalt may lead to various abnormalities like endocrine dysfunction, *etc.*[296] Therefore, the detection of cobalt is essential for human health. A study by Wang *et al.* synthesized N-doped MXene QDs for the fluorescence detection of cobalt,[297] employing previously reported methods to obtain MXene nanosheets.[298] Then 50 mg of multilayer MXene sheets (Ti$_3$C$_2$) were mixed with 20 mL of 6 M KOH and the solution was sonicated at RT for 3 h and centrifuged for 5 min at 3900 rpm to get thin-layer MXene sheets. Then 48 mg of the obtained powder was mixed with 15 mL of DMF and transferred to a PTFE-lined stainless-steel autoclave, and a reaction was carried out at 140 °C for 12 h. The mixture was centrifuged at 3900 rpm for 5 min to obtain N-doped MXene QDs. Following this, mixtures of different concentrations of cobalt ions were made, from 0.5 μM–2000 μM. Acetate buffer with a concentration of 0.2 M (0.5 mL) was added to each concentration of cobalt solution and then 400 μL of N-doped MXene QDs was added to each; the final solution was made up to 2 mL by adding deionized water. Finally, the solution was reacted for 5 min after this, and emission spectra were recorded at an excitation wavelength of 335 nm; the reported LOD was 0.21 μM, as illustrated in Fig. 14.

4.3.5. MXene-QD-based sensors for nitrite. Nitrite ions are heavily used in the food industry as fertilizers and food preservatives.[299] They pose several health and environmental concerns, as their presence in water and food beyond permissible levels poses significant risks.[300] High levels of nitrite ions may
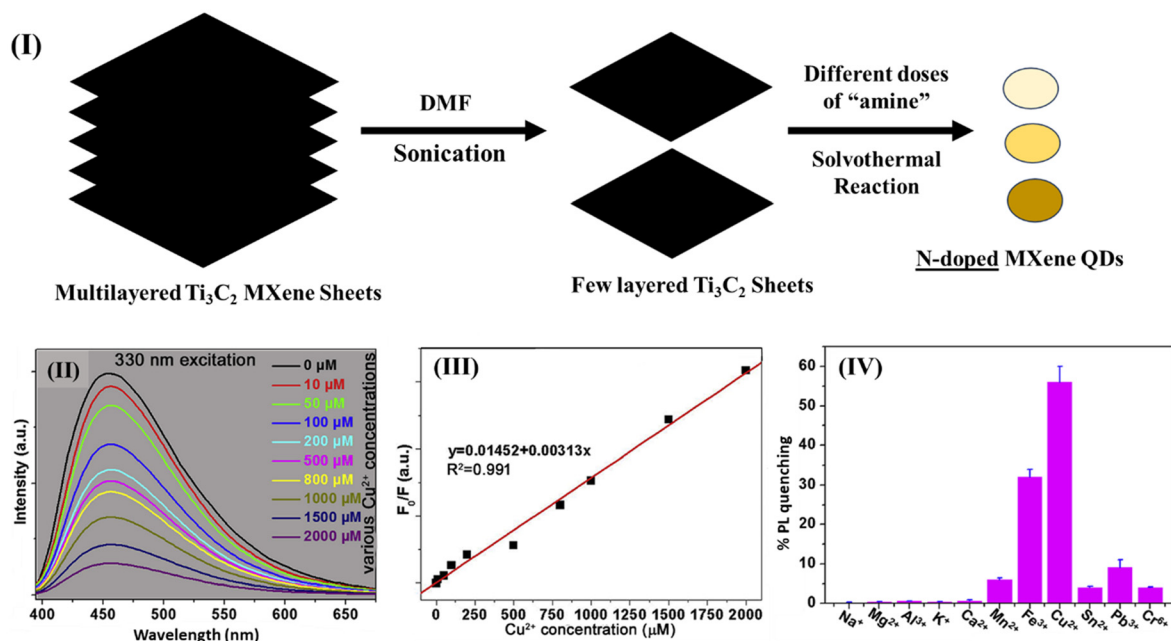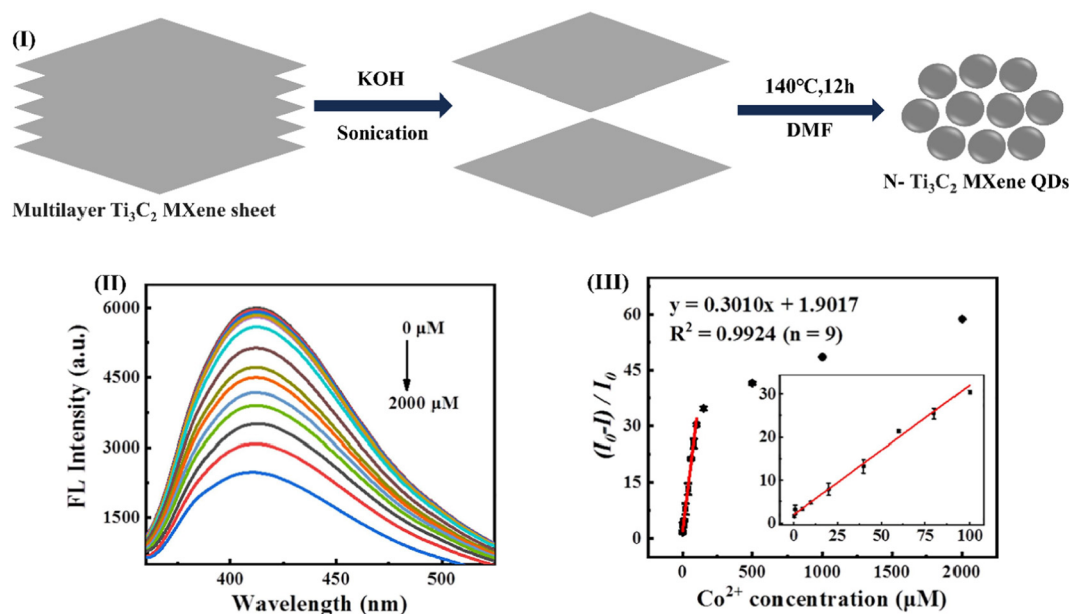
Fig. 13 Schematic illustrations of N-MXene QD synthesis from nanosheets, and their deployment for the sensing of copper in a complex matrix. (I) A schematic representation of the delamination of multilayered MXene into few-layered MXene nanosheets using DMF-aided sonication, and the subsequent synthesis of N-MXene QDs through a solvothermal method using different doses of amine. (II) Fluorescence emission spectra of N-MXene QDs in the presence of different concentrations of Cu^{2+} (0–2000 µM), highlighting the concentration-dependent fluorescence quenching of the sensor probe through copper–ion interactions. (III) F_0/F (F_0: intensity without Cu^{2+}; F: intensity with Cu^{2+}) as a function of the Cu^{2+} concentration, which confirms that as the concentration of metal ions increased, the F_0/F value also increased (black line: measured value; red line: fitted value). (IV) The percentage PL quenching in the presence of different interfering metal ions, which suggests that the developed probe showed the highest quenching for Cu^{2+}, confirming the selectivity of the sensor for copper ions. Reproduced with permission from ref. 102; copyright 2020, ELSEVIER.

potentially lead to serious threats to public health, including muscular paralysis, neurodegenerative illness, potential carcinogenesis, and methemoglobinemia. The International Agency for Research on Cancer of the World Health Organization categorized nitrite ions as a 2A carcinogen.[301] Therefore, exploring newer technologies for their detection needs considerable attention and investigation. For this, researchers explored miniaturized sensor probes employing MXene QDs for the detection of nitrite ions. A study by Bai *et al.* developed a MXene-QD-based colorimetric probe for nitrite assays.[302] They used HF etching treatment for MXene and, subsequently, they finely downsized these 2D sheets to zero-dimensional status through microwave-assisted methods with simultaneous doping with nitrogen and phosphorus. The reaction conditions for curing the 2D MXene were a temperature of 120 °C at a power of 800 W for 25 min. Following this, a 220 nm filter membrane was used to separate out the product from the mixture and then, through rotatory evaporation and vacuum drying, N,P-doped MXene QDs were obtained. These were stored at 6 °C for further use. Then they developed a paper-based colorimetric chip by treating a filter strip with 0.1 mg mL^{-1} doped MXene QDs and 225 µM Phen solution for the detection of nitrite ions in diverse matrices. Following this, previously prepared solutions of 2mMFe^{2+} (75 µL) and 2mM H$^+$ (40 µL) were drop-casted over the chip

and visualized using the naked eye in sunlight, as illustrated in Fig. 15.

4.3.6. MXene-QD-based sensors for pirimiphos-methyl. Pirimiphos-methyl is a broad-spectrum organophosphate that is based on *O,O*-dimethyl *O*-pyrimidin-4-yl phosphorothioate substituted by a methyl moiety at position 6 and a diethyl-amino moiety at position 2.[303] It is an organophosphate and aminopyrimidine that is widely employed in agrochemicals as an acaricide, insecticide, and acetylcholinesterase inhibitor; it is categorized as an environmental contaminant and also used to protect seeds, stored grains and nuts.[304] It can phosphory-late acetylcholinesterase (AChE) enzymes in tissues, causing the accumulation of acetylcholine at neuromuscular junctions and synapses, finally leading to death.[305] In a joint meeting on pesticide residues (JMPR) organized by the Food and Agriculture Organization, the World Health Organization proposed an acceptable daily intake of 0.00–0.03 mg per kg body-weight.[306] Therefore, the detection of pirimiphos-methyl is essential for human health; for this, Ding *et al.* developed a copper-decorated MXene QDs-aerogel based sensor probe.[307] They synthesized MXene QDs through a hydrothermal method at 100 °C for 6 h; following this, the reaction mixture was filtered with a 220 nm filter membrane at room temperature. Then 50 µL of Cu@MXene QDs-aerogel (5 mg mL^{-1}), 50 µL of tetramethylbenzidine (TMB), and 20 µL of H$_2$O$_2$ (30%) were

Fig. 14 Schematic illustrations of MXene QD synthesis from multilayered MXene nanosheets and their subsequent deployment for the detection of cobalt. (I) A schematic representation of N-doped MXene QD synthesis, highlighting the ultrasonic exfoliation and solvothermal chemical cutting of few-layered nanosheets into MXene QDs. (II) FL emission spectra of N-MXene QDs with different concentrations of Co^{2+} (0–2000 μM) at a fixed excitation wavelength, showing a progressive decrease in fluorescence intensity as the cobalt concentration increases. This concentration-dependent quenching phenomenon indicates the potential complexation of cobalt ions with MXene QDs. (III) A plot of $(I_0 - I)/I_0$ versus Co^{2+} concentration. Inset: the linear relationship between $(I_0 - I)/I_0$ and Co^{2+} in the concentration range of 0.5–100 μM. I_0: FL intensity of N-MXene QDs, I: FL intensity of N-MXene QDs in the presence of Co^{2+}. This plot indicates the linear trend of sensor probe quenching versus the concentration of cobalt ions, showing the stability and sensitivity of the sensor. Reproduced with permission from ref. 297; copyright 2022, ELSEVIER.

mixed in acetate buffer solution at pH 4.0 (2 mL) and incubated for 10 min at 40 °C. The sensor showed a distinct absorption peak at 652 nm with a prominent blue color; upon the introduction of pirimiphos-methyl, the catalytic activity diminished and it exhibited a light blue color. This unique property of Cu@MXene QDs-aerogel makes it a promising platform for the colorimetric detection of pirimiphos-methyl and a wide LDR of 100–3200 nM and low LOD of 0.65 nM were reported.

5. Limitations and future scope of MXene QDs

MXene QDs are emerging zero-dimensional nanomaterials that can be deployed in different commercial settings, including sensor setups for the sensitive and selective detection of different categories of molecules, as explained above. Despite the numerous advantages explained above, there are also a few limitations limiting their practical deployment for real-world applications, which are described here.

5.1. Synthesis complexity

The process of MXene QD synthesis is intricate and tedious and requires the selective etching of "A" from the MAX phase through *ex situ* or *in situ* approaches, followed by the chemical cutting of exfoliated nanosheets. The choice of etching agent

and etching time significantly affects the exfoliation process, often leading to incomplete exfoliation or sometimes harsh environments which can introduce unwanted defects. The exfoliated 2D nanosheets show a tendency to aggregate that affects QD formation. These bottlenecks limit the application of these QDs. Different synthetic routes have their own advantages and limitations too which require further research to optimize them for obtaining QDs with the desired properties. This article presents the huge scope for exploring newer synthetic routes that offer high levels of surface functionality and enhanced stability, while minimizing the use of toxic and hazardous chemicals. We have not only highlighted the current state of MXene QD synthesis but this effort also presents the immense opportunities for innovation in synthetic strategies through chemical engineering that can prioritize toxicity reduction, functional-group retention, and dispersion stability.

5.2. Structural and chemical stability

MXenes and their derivatives including MXene QDs exhibit tremendous properties such as high electrical conductivity, excellent photoluminescence properties, tunable surface terminations, and high surface areas. However, in some situations environmental exposure is inevitable, making them more prone to oxidation under atmospheric and aqueous conditions, degrading their quantum properties and limiting the application of these QDs. In some cases, oxidation potentially
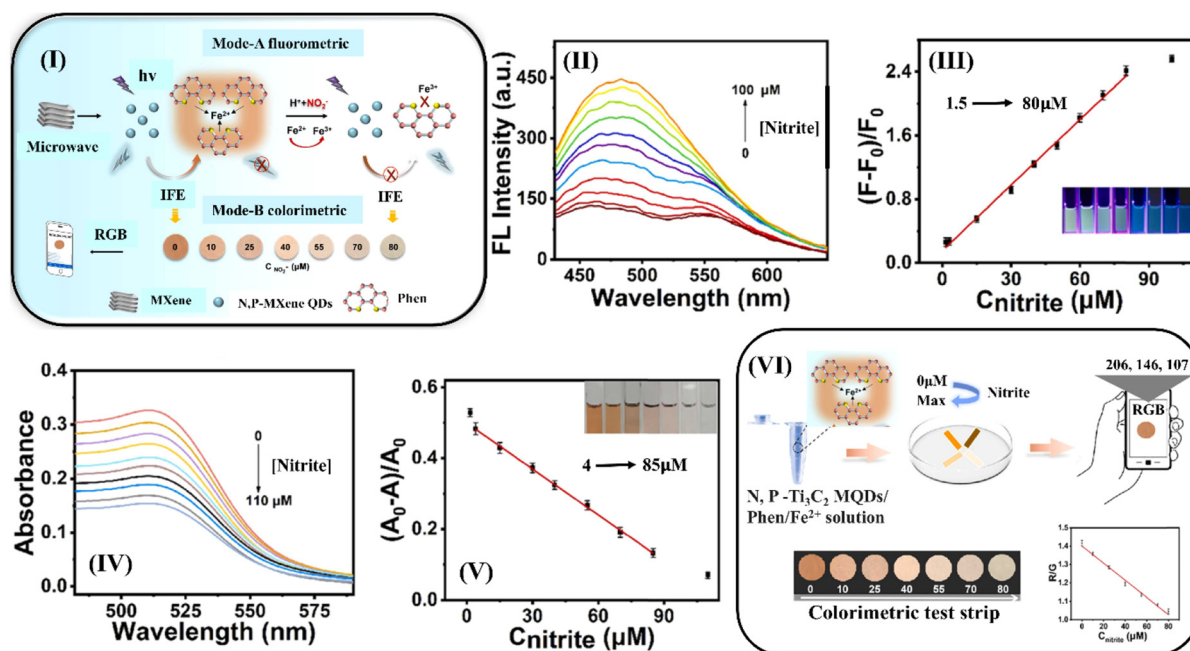
Fig. 15 (I) A schematic representation of N,P-MXene QD synthesis and their deployment for the detection of NO^{2-} employing a dual-mode strategy. (II) FL spectra of the developed probe with different concentrations of NO^{2-} (0–100 μM). (III) A linear plot of the FL intensity ratio $(F_0 - F)/F_0$ *versus* NO^{2-} concentration (1.5–80 μM); inset: a photograph of the developed probe with different concentrations of NO^{2-} (from left to right: 1.5, 15, 30, 40, 50, 60, 70, and 80 μM) taken under 395 nM UV light. (IV) Absorption spectra of the developed probe with different concentrations of NO^{2-} (0–110 μM). (V) A linear plot of the absorbance ratio $(A_0 - A)/A_0$ *versus* NO^{2-} concentration (4–85 μM); inset: corresponding photographs of the developed probe with different concentrations of NO^{2-} (from left to right: 4, 15, 30, 40, 55, 70, and 85 μM) taken under daylight. Developed probe: N,P-MXene QDs (0.1 mg mL^{-1}); Phen (225 μM); Fe^{2+} (75 μM); H^+ (40 μM). (VI) A schematic representation of a smartphone-assisted sensor for NO^{2-} with colorimetric paper strips over concentrations ranging from 0–80 μM; the inset graph represents the R/G intensity *versus* NO^{2-} concentration. Reproduced with permission from ref. 302; copyright 2022, ELSEVIER.

disrupts the metallic nature by oxidizing the "M" atoms into MO_x, which shows less conductivity. These limitations have encouraged researchers across the globe to explore newer strategies for monodisperse QDs with high structural and chemical stability.

5.3. Scalability and yields

Despite the huge interest in MXene QDs due to their remarkable optoelectronic properties, a major bottleneck in their practical commercialization is the low synthesis yields of currently explored fabrication methods. Hydrothermal, solvothermal, and ultrasonication approaches are the most commonly explored methods for MXene QD fabrication from the MAX phase. Among these, hydrothermal methods are the most widely used ones owing to their simplicity and ability to control surface functionality and morphology, but they show yields of <10% limiting their large-scale production compared to other QDs such as graphene QDs and carbon dots. This low-yield output per batch increases the overall cost of MXene QDs, limiting their real-world applications. Low yields involve significant precursor material loss during the synthesis process which makes processes expensive and also increases the environmental burden. This creates a niche for large scale production approaches for MXene QDs that fulfill the current needs. This limitation also presents an opportunity for innovation and advancements that could position these materials for real-world applications such as in commercial sensing devices and clinical diagnostics.

5.4. Toxicity and environmental concerns

MXene QDs are emerging next-generation nanomaterials. Their synthesis from MAX requires the etching agent HF which is highly corrosive, colorless and toxic, requiring extra attention during experiments and also posing environmental concern. Despite this, other organic solvents have also been explored for the exfoliation process that may also pose safety issues and show environmental instability, limiting the synthesis and scope of these QDs. Due to their enormously wide applications, these emerging materials can be a game-changing probe in the future for various sectors, including health care and diagnostics. Therefore, toxicity and environmental concerns are big hurdles, which require alternative approaches adopting green chemistry principles that can fulfil current needs and the wide potential, while leaving a negligible environmental footprint and minimizing health concerns.

5.5. Sensor fabrication

MXene QDs have shown exceptional potential for use in sensor due to their unique optoelectronic properties and large surface-area-to-volume ratios. However, certain challenges

such as intricate surface functionalization, limited stability, and batch-to-batch variability hinder their widespread deployment. Addressing these challenges presents a promising platform for budding researchers seeking new innovations in materials engineering.

Despite the remarkable advancements in MXene QDs and their application in sensor settings, several challenges must be addressed to enhance their practical applicability to fulfill current demands relating to healthcare diagnosis. The extensive exploration of the fundamental properties of MXene QDs, including electronic structures, surface chemistry, and interaction mechanisms, is required for gaining a better understanding. The exploration of newer and more sustainable synthetic routes following green chemistry principles that offer higher yields, lower toxicity, and enhanced stability and optoelectronic properties is also required. That could open up their widespread adoption for large-scale production and deployment in commercial settings, including sensor fabrication. The monodisperse size, defects, and distribution of functional groups in MXene QDs largely depend on the reaction conditions and formation mechanism of MXene QDs. Other areas like the mechanism behind the formation of MXene QDs and controlling the size of MXene QDs are less explored, which has limited the application of MXene QDs to a large extent. As MXene QDs are a recently explored material, their potential is yet to be recognized to the fullest. There are untraversed and emerging areas that can be explored in the future for MXene-QD-based sensors, of which a few are discussed in this article. This article aims to suggest necessary improvements that are awaited before the integration of MXene QDs into point-of-care next generation diagnostics, wearable sensors, and multi-mode detection platforms.

6. Conclusions

MXene QDs represent a transformative advancement and have emerged as a new class of zero-dimensional nanomaterial offering exceptional structural, electronic and optical properties. The distinctive advantages of the zero dimensionality of MXene QDs and the incorporation of unique structural and functional richness from 2D MXene precursors has attracted the attention of budding as well as established researchers. This immense focus has paved a foundation for remarkable developments in just a few years, highlighting MXene QDs and MXene-QD-based sensors due their unique optoelectronic properties. In this paper, the first part covers the crucial role of the MAX phase precursor, MXene nanosheets and their novel role in determining the composition, structure, and functionality of MXene QDs. This is further followed by a discussion of the diverse methods of MXene QD synthesis, each offering a unique opportunity to control particle size, crystallinity, and surface chemistry, which play crucial roles in the sensing behavior of MXene QDs. These strategies include ball milling, pyrolysis, molten salt, hydrothermal, and solvothermal synthesis, and ultrasonication. Each of these has its own pros and cons, so the selection of an appropriate method depends on the desired properties and applications of QDs. Furthermore, a later section includes extensive discussion on the unique properties of MXene QDs, including structural, electronic, and optical properties, which collectively contribute to sensor performance. After this, the most important part of the paper discusses a range of MXene-QD-based sensors, such as electrochemiluminescence, photoluminescence, and optical sensors, for a range of molecules including small molecules, macromolecules, and environmental pollutants. A later section includes insightful discussion on the limitations and future scope of MXene QDs. Another part of this paper comprehensively discusses sensor fabrication strategies, limits of detection (LODs), linear detection ranges (LDRs), synthetic routes, and the analysis of real samples, along with the detection techniques involved in sensor development in various studies. The aim of this article is to provide a holistic overview of MXene QDs, including their properties, synthesis, and applications in the field of sensors, attracting budding researchers towards these emerging MXene QDs.

Abbreviations

QDs	Quantum dots
LOD	Limit of detection
LDR	Linear dynamic range
D	Dimensional
PL	Photoluminescence
FL	Fluorescence
ECL	Electrochemiluminescence
SEM	Scanning electron microscopy
STEM	Scanning transmission electron microscopy
TEM	Transmission electron microscopy
XRD	X-ray diffraction
red-P	Red phosphorus
DOS	Density of states
EBS	Energy band structure
Vis	Visible
PLLTs	Photoluminescence lifetimes
PLQYs	Photoluminescence quantum yields
DMSO	Dimethyl sulfoxide
IFE	Inner filter effect
GSH	Glutathione
OPD	*o*-Phenylenediamine
UA	Uric acid
QC	Quercetin
DA	Dopamine
AA	Ascorbic acid
ARS	Alizarin red
PBS	Phosphate buffer saline
HRP	Horseradish peroxidase
TNBC	Triple negative breast cancer
HER2	Human epidermal growth factor 2
AuNBs	Gold nanobones
DNA	Deoxyribonucleic acid

mi-RNA	Micro-ribonucleic acid
GCE	Glassy carbon electrode
MUC1	Mucin 1
PNK	Polynucleotide kinase
HF	Hydrogen fluoride
LiF	Lithium fluoride
ATP	Adenosine triphosphate
GOD	Glucose oxidase
BSA	Bovine serum albumin
TMOAH	Tetramethyl ammonium hydroxide
PEI	Polyethylene imine
COF	Covalent organic framework
OTC	Over-the-counter

Conflicts of interest

The authors declare that they have no known competing financial interests or personal relationships that could have appeared to influence the work reported in this paper.

Data availability

No primary research results, software or code have been included and no new data were generated or analysed as part of this review.

Acknowledgements

References

1 A. Gnach, T. Lipinski, A. Bednarkiewicz, J. Rybka and J. A. Capobianco, *Chem. Soc. Rev.*, 2015, **44**, 1561–1584.

2 S. Bayda, M. Adeel, T. Tuccinardi, M. Cordani and F. Rizzolio, *Molecules*, 2019, **25**, 112.

3 R. Pisano and A. Durlo, in *Handbook for the Historiography of Science*, ed. M. L. Condé and M. Salomon, Springer International Publishing, Cham, 2023, pp. 441–478.

4 S. A. Ahire, A. A. Bachhav, T. B. Pawar, B. S. Jagdale, A. V. Patil and P. B. Koli, *Results in Chem.*, 2022, **4**, 100633.

5 P. Mulvaney, *ACS Nano*, 2015, **9**, 2215–2217.

6 L. Manna, *Nano Lett.*, 2023, **23**, 9673–9676.

7 C. B. Murray, D. J. Norris and M. G. Bawendi, *J. Am. Chem. Soc.*, 1993, **115**, 8706–8715.

8 D. Boufidis, R. Garg, E. Angelopoulos, D. K. Cullen and F. Vitale, *Nat. Commun.*, 2025, **16**, 1861.

9 C. (John) Zhang, Y. Ma, X. Zhang, S. Abdolhosseinzadeh, H. Sheng, W. Lan, A. Pakdel, J. Heier and F. Nüesch, *Energy Environ. Mater.*, 2020, **3**, 29–55.

10 Y. Gogotsi and Q. Huang, *ACS Nano*, 2021, **15**, 5775–5780.

11 N. Li, J. Huo, Y. Zhang, B. Ye, X. Chen, X. Li, S. Xu, J. He, X. Chen, Y. Tang, Y. Zhu, K. Ling and R. Zhu, *Sep. Purif. Technol.*, 2024, **330**, 125325.

12 E. Mari, M. Duraisamy, M. Eswaran, S. Sellappan, K. Won, P. Chandra, P.-C. Tsai, P.-C. Huang, Y.-H. Chen, Y.-C. Lin and V. K. Ponnusamy, *Microchim. Acta*, 2024, **191**, 212.

13 Y. Gogotsi and B. Anasori, *ACS Nano*, 2019, **13**, 8491–8494.

14 M. Shekhirev, C. E. Shuck, A. Sarycheva and Y. Gogotsi, *Prog. Mater. Sci.*, 2021, **120**, 100757.

15 M. Naguib, J. Come, B. Dyatkin, V. Presser, P.-L. Taberna, P. Simon, M. W. Barsoum and Y. Gogotsi, *Electrochem. Commun.*, 2012, **16**, 61–64.

16 Q. Xue, H. Zhang, M. Zhu, Z. Pei, H. Li, Z. Wang, Y. Huang, Y. Huang, Q. Deng, J. Zhou, S. Du, Q. Huang and C. Zhi, *Adv. Mater.*, 2017, **29**, 1604847.

17 S. K. Kailasa, D. J. Joshi, J. R. Koduru and N. I. Malek, *J. Mol. Liq.*, 2021, **342**, 117524.

18 V. Naresh and N. Lee, *Sensors*, 2021, **21**, 1109.

19 V. N. Mehta, M. L. Desai, H. Basu, R. Kumar Singhal and S. K. Kailasa, *J. Mol. Liq.*, 2021, **333**, 115950.

20 X. Cui, Q. Ruan, X. Zhuo, X. Xia, J. Hu, R. Fu, Y. Li, J. Wang and H. Xu, *Chem. Rev.*, 2023, **123**, 6891–6952.

21 A. T. Smith, A. M. LaChance, S. Zeng, B. Liu and L. Sun, *Nano Mater. Sci.*, 2019, **1**, 31–47.

22 Y. Zhu, L. Feng, R. Zhao, B. Liu and P. Yang, *ACS Appl. Nano Mater.*, 2024, **7**, 2546–2574.

23 G. P. Lim, C. F. Soon, N. L. Ma, M. Morsin, N. Nayan, M. K. Ahmad and K. S. Tee, *Environ. Res.*, 2021, **201**, 111592.

24 G. P. Lim, C. F. Soon, N. L. Ma, M. Morsin, N. Nayan, M. K. Ahmad and K. S. Tee, *Environ. Res.*, 2021, **201**, 111592.

25 H. Lin, S. Gao, C. Dai, Y. Chen and J. Shi, *J. Am. Chem. Soc.*, 2017, **139**, 16235–16247.

26 M. Naguib, M. W. Barsoum and Y. Gogotsi, *Adv. Mater.*, 2021, **33**, 2103393.

27 A. VahidMohammadi, J. Rosen and Y. Gogotsi, *Science*, 2021, **372**, eabf1581.

28 C. Zhou, K. B. Tan, W. Han, L. Wang and M. Lu, *Particuology*, 2024, **91**, 50–71.

29 A. Ali, S. M. Majhi, L. A. Siddig, A. H. Deshmukh, H. Wen, N. N. Qamhieh, Y. E. Greish and S. T. Mahmoud, *Biosensors*, 2024, **14**, 497.

30 F. Yang, Y. Ge, T. Yin, J. Guo, F. Zhang, X. Tang, M. Qiu, W. Liang, N. Xu, C. Wang, Y. Song, S. Xu and S. Xiao, *ACS Appl. Nano Mater.*, 2020, **3**, 11850–11860.

31 W. Cao, J. Nie, Y. Cao, C. Gao, M. Wang, W. Wang, X. Lu, X. Ma and P. Zhong, *Chem. Eng. J.*, 2024, **496**, 154097.

32 T. Koriukina, A. Kotronia, J. Halim, M. Hahlin, J. Rosen, K. Edström and L. Nyholm, *ACS Omega*, 2022, **7**, 41696–41710.

33 Y. Pang, J. Li, K. Lv, D. Tang and Q. Li, *New J. Chem.*, 2024, **48**, 12477–12495.

34 Y. Liu, W. Zhang and W. Zheng, *Chin. J. Catal.*, 2022, **43**, 2913–2935.

35 R. Akhter and S. S. Maktedar, *J. Materiomics*, 2023, **9**, 1196–1241.

36 U. U. Rahman, M. Humayun, U. Ghani, M. Usman, H. Ullah, A. Khan, N. M. El-Metwaly and A. Khan, *Molecules*, 2022, **27**, 4909.

37 Z. Li, L. Wang, D. Sun, Y. Zhang, B. Liu, Q. Hu and A. Zhou, *Mater. Sci. Eng., B*, 2015, **191**, 33–40.

38 B. Hu, J. Chen, Z. Gao, L. Chen, T. Cao, H. Li, Q. Yu, C. Wang and Z. Gan, *ACS Appl. Bio Mater.*, 2024, **7**, 4339–4351.

39 A. Dehingia, U. Das, D. Mandal and A. Roy, *Mater. Today Sustainability*, 2024, **25**, 100619.

40 S. Ghosh, S. Barg, S. M. Jeong and K. (Ken) Ostrikov, *Adv. Energy Mater.*, 2020, **10**, 2001239.

41 H. Wang, A. Abdussalam and G. Xu, *Bioelectrochemistry*, 2022, **148**, 108249.

42 J. Gou, L. Zhao, Y. Li and J. Zhang, *ACS Appl. Nano Mater.*, 2021, **4**, 12308–12315.

43 G. Rajapriya, R. Sangubotla and J. Kim, *Korean J. Chem. Eng.*, 2024, **41**, 1805–1813.

44 D. Chinemerem Nwobodo, M. C. Ugwu, C. Oliseloke Anie, M. T. S. Al-Ouqaili, J. Chinedu Ikem, U. Victor Chigozie and M. Saki, *J. Clin. Lab. Anal.*, 2022, **36**, e24655.

45 F. J. Tovar-Lopez, *Sensors*, 2023, **23**, 5406.

46 D. Chinemerem Nwobodo, M. C. Ugwu, C. Oliseloke Anie, M. T. S. Al-Ouqaili, J. Chinedu Ikem, U. Victor Chigozie and M. Saki, *J. Clin. Lab. Anal.*, 2022, **36**, e24655.

47 O. Gideon, H. S. Samuel and I. A. Okino, *Discov. Chem.*, 2024, **1**, 34.

48 C. Zhou, K. B. Tan, W. Han, L. Wang and M. Lu, *Particuology*, 2024, **91**, 50–71.

49 M. Mohkam, M. Sadraeian, A. Lauto, A. Gholami, S. H. Nabavizadeh, H. Esmaeilzadeh and S. Alyasin, *Microsyst. Nanoeng.*, 2023, **9**, 145.

50 Y. Wang, Y. Xu, M. Hu, H. Ling and X. Zhu, *Nanophotonics*, 2020, **9**, 1601–1620.

51 C. Guan, X. Yue, J. Fan and Q. Xiang, *Chin. J. Catal.*, 2022, **43**, 2484–2499.

52 A. Rafieerad, W. Yan, K. N. Alagarsamy, A. Srivastava, N. Sareen, R. C. Arora and S. Dhingra, *Adv. Funct. Mater.*, 2021, **31**, 2106786.

53 Y. Guo, Y. Cheng, X. Li, Q. Li, X. Li and K. Chu, *J. Hazard. Mater.*, 2022, **423**, 127053.

54 Y. Cheng, X. Li, P. Shen, Y. Guo and K. Chu, *Energy Environ. Mater.*, 2023, **6**, e12268.

55 G. Behzadi Pour and L. Fekri Aval, *Electrochem. Commun.*, 2025, **172**, 107874.

56 I. Ahmad, Y. Raharjo, A. Batool, A. Zakir, H. Manzoor, A. Arooj, J. Khalid, N. Ali and K. Rasool, *Trends Environ. Anal. Chem.*, 2023, **39**, e00210.

57 T. Amrillah, C. Abdullah, A. Hermawan, F. Sari and V. Alviani, *Nanomaterials*, 2022, **12**, 4280.

58 C. E. Shuck, K. Ventura-Martinez, A. Goad, S. Uzun, M. Shekhirev and Y. Gogotsi, *ACS Chem. Health Saf.*, 2021, **28**, 326–338.

59 A. Zhou, C.-A. Wang and Y. Hunag, *J. Mater. Sci.*, 2003, **38**, 3111–3115.

60 L. Gao, T. Han, Z. Guo, X. Zhang, D. Pan, S. Zhou, W. Chen and S. Li, *Adv. Powder Technol.*, 2020, **31**, 3533–3539.

61 X. H. Wang and Y. C. Zhou, *Acta Mater.*, 2002, **50**, 3143–3151.

62 G. Deysher, C. E. Shuck, K. Hantanasirisakul, N. C. Frey, A. C. Foucher, K. Maleski, A. Sarycheva, V. B. Shenoy, E. A. Stach, B. Anasori and Y. Gogotsi, *ACS Nano*, 2020, **14**, 204–217.

63 K. R. G. Lim, M. Shekhirev, B. C. Wyatt, B. Anasori, Y. Gogotsi and Z. W. Seh, *Nat. Synth.*, 2022, **1**, 601–614.

64 H. Zong, K. Yu and Z. Zhu, *Electrochim. Acta*, 2020, **353**, 136598.

65 C. E. Shuck, K. Ventura-Martinez, A. Goad, S. Uzun, M. Shekhirev and Y. Gogotsi, *ACS Chem. Health Saf.*, 2021, **28**, 326–338.

66 X. Li, F. Ran, F. Yang, J. Long and L. Shao, *Trans. Tianjin Univ.*, 2021, **27**, 217–247.

67 Y. Liu, Q. Tang, M. Xu, J. Ren, C. Guo, C. Chen, W. Geng, W. Lei, X. Zhao and D. Liu, *Chem. Eng. J.*, 2023, **468**, 143439.

68 J. E. Von Treifeldt, K. L. Firestein, J. F. S. Fernando, C. Zhang, D. P. Siriwardena, C.-E. M. Lewis and D. V. Golberg, *Mater. Des.*, 2021, **199**, 109403.

69 C. Zhao, L. Xiao, Z. Chen and Y. Zhang, *Acc. Mater. Res.*, 2024, **5**, 1583–1597.

70 Z. Chen, C. Zhao, X. Zhou, L. Xiao, Z. Li and Y. Zhang, *Small Sci.*, 2023, **3**, 2300086.

71 T. Zhang, X. Jiang, G. Li, Q. Yao and J. Y. Lee, *ChemNanoMat*, 2018, **4**, 56–60.

72 S. Tian, G. Cheng, Z. Tang, F. Sha, Z. Xuan and G. Ding, *Ceram. Int.*, 2020, **46**, 28949–28954.

73 N. Xue, X. Li, M. Zhang, L. Han, Y. Liu and X. Tao, *ACS Appl. Energy Mater.*, 2020, **3**, 10234–10241.

74 H. Cheng, L. Ding, G. Chen, L. Zhang, J. Xue and H. Wang, *Adv. Mater.*, 2018, **30**, 1803694.

75 Y. Wang, C. Li, X. Han, D. Liu, H. Zhao, Z. Li, P. Xu and Y. Du, *ACS Appl. Nano Mater.*, 2018, **1**, 5366–5376.

76 M. Z. Abid, K. Rafiq, A. Aslam, R. Jin and E. Hussain, *J. Mater. Chem. A*, 2024, **12**, 7351–7395.

77 D. D. Kruger, H. García and A. Primo, *Adv. Sci.*, 2024, 2307106.

78 Y. Iwadate, in *Handbook on the Physics and Chemistry of Rare Earths*, Elsevier, 2014, vol. 44, pp. 87–168.

79 M. U. Zahid, E. Pervaiz, A. Hussain, M. I. Shahzad and M. B. K. Niazi, *Mater. Res. Express*, 2018, **5**, 052002.

80 M. Devi, S. Rawat and S. Sharma, *Oxf. Open Mater. Sci.*, 2020, **1**, itab014.

81 J. Sun, B. S. Shengping Zhang, M. Alomar, A. S. Alqarni, M. S. Najla Alotaibi, M. S. Badriah Alshahrani, A. A. Alghamdi, Z. Kou, W. Shen, Y. Chen and J. Zhang, *Chem. Rec.*, 2023, **23**, e202200268.

82 W. Shi, S. Song and H. Zhang, *Chem. Soc. Rev.*, 2013, **42**, 5714.

83 E. Saita, M. Iwata, Y. Shibata, Y. Matsunaga, R. Suizu, K. Awaga, J. Hirotani and H. Omachi, *Front. Chem.*, 2022, **10**, 841313.

84 Y.-J. Kim, S. J. Kim, D. Seo, Y. Chae, M. Anayee, Y. Lee, Y. Gogotsi, C. W. Ahn and H.-T. Jung, *Chem. Mater.*, 2021, **33**, 6346–6355.

85 M. Kulkarni, A. Lalic, R. Balu, H. Zhang, N. K. Dutta and N. Roy Choudhury, *MRS Adv.*, 2024, **9**, 1310–1317.

86 W. Kong, Y. Niu, M. Liu, K. Zhang, G. Xu, Y. Wang, X. Wang, Y. Xu and J. Li, *Inorg. Chem. Commun.*, 2019, **105**, 151–157.

87 V. N. Mehta, M. L. Desai, H. Basu, R. Kumar Singhal and S. K. Kailasa, *J. Mol. Liq.*, 2021, **333**, 115950.

88 H. R. You, S. Lee, D. H. Lee, G. Murali, A. S. Nissimagoudar, Y. Kim, S. Park, J. Lee, S. J. Kim, J. Y. Park, B. J. Moon, Y. H. Park, S. Kim, H. N. Yu, H. J. Kim, W. Lee, G. Ham, H. Lee, S. Lee, H. Cha, J. Lim, Y. Gogotsi, T. K. An, I. In and J. Choi, *Adv. Energy Mater.*, 2023, **13**, 2301648.

89 W. Kong, Y. Niu, M. Liu, K. Zhang, G. Xu, Y. Wang, X. Wang, Y. Xu and J. Li, *Inorg. Chem. Commun.*, 2019, **105**, 151–157.

90 Q. Xue, H. Zhang, M. Zhu, Z. Pei, H. Li, Z. Wang, Y. Huang, Y. Huang, Q. Deng, J. Zhou, S. Du, Q. Huang and C. Zhi, *Adv. Mater.*, 2017, **29**, 1604847.

91 F. Ai, C. Fu, G. Cheng, H. Zhang, Y. Feng, X. Yan and X. Zheng, *ACS Appl. Nano Mater.*, 2021, **4**, 8192–8199.

92 Y. Li, L. Ding, Y. Guo, Z. Liang, H. Cui and J. Tian, *ACS Appl. Mater. Interfaces*, 2019, **11**, 41440–41447.

93 F. Yan, J. Sun, Y. Zang, Z. Sun, H. Zhang, J. Xu and X. Wang, *Dyes Pigm.*, 2021, **195**, 109720.

94 C. Wei, B. Xi, P. Wang, Z. Wang, X. An, K. Tian, J. Feng and S. Xiong, *Adv. Energy Sustain. Res.*, 2023, **4**, 2300103.

95 J. Sui, X. Chen, Y. Li, W. Peng, F. Zhang and X. Fan, *RSC Adv.*, 2021, **11**, 16065–16082.

96 C. Guan, X. Yue, J. Fan and Q. Xiang, *Chin. J. Catal.*, 2022, **43**, 2484–2499.

97 K. Yan, P. Wang, M. Wang, M. Zhang, W. Liu and Q. Ma, *Microchem. J.*, 2022, **179**, 107589.

98 A. S. Sharbirin, S. Akhtar and J. Kim, *Opto-Electron. Adv.*, 2021, **4**, 200077.

99 S. Munir, A. Rasheed, T. Rasheed, I. Ayman, S. Ajmal, A. Rehman, I. Shakir, P. O. Agboola and M. F. Warsi, *ACS Omega*, 2020, **5**, 26845–26854.

100 Z. Zhou, L. Li, X. Liu, H. Lei, W. Wang, Y. Yang, J. Wang and Y. Cao, *J. Mol. Liq.*, 2021, **324**, 115116.

101 I. J. Soní-Castro, A. B. López-Oyama, E. R. González, D. Del Ángel-López, M. A. Aguilar-Frutis and J. J. Reyes-Valdez, *Crystals*, 2024, **14**, 888.

102 Y. Feng, F. Zhou, Q. Deng and C. Peng, *Ceram. Int.*, 2020, **46**, 8320–8327.

103 S. Lu, L. Sui, Y. Liu, X. Yong, G. Xiao, K. Yuan, Z. Liu, B. Liu, B. Zou and B. Yang, *Adv. Sci.*, 2019, **6**, 1801470.

104 W. Zhang and X. Zhang, *Ultrason. Sonochem.*, 2022, **89**, 106122.

105 W. Feng, H. Luo, Y. Wang, S. Zeng, Y. Tan, H. Zhang and S. Peng, *Ceram. Int.*, 2018, **44**, 7084–7087.

106 A. E. Ghazaly, H. Ahmed, A. R. Rezk, J. Halim, P. O. Å. Persson, L. Y. Yeo and J. Rosen, *ACS Nano*, 2021, **15**, 4287–4293.

107 R. Ramírez, A. Melillo, S. Osella, A. M. Asiri, H. Garcia and A. Primo, *Small Methods*, 2023, **7**, 2300063.

108 S.-W. Ohl, E. Klaseboer and B. C. Khoo, *Interface Focus*, 2015, **5**, 20150019.

109 Q. Zhang, Y. Sun, M. Liu and Y. Liu, *Nanoscale*, 2020, **12**, 1826–1832.

110 Q. Xue, H. Zhang, M. Zhu, Z. Pei, H. Li, Z. Wang, Y. Huang, Y. Huang, Q. Deng, J. Zhou, S. Du, Q. Huang and C. Zhi, *Adv. Mater.*, 2017, **29**, 1604847.

111 G. Xu, Y. Niu, X. Yang, Z. Jin, Y. Wang, Y. Xu and H. Niu, *Adv. Opt. Mater.*, 2018, **6**, 1800951.

112 J. Zhu, E. Ha, G. Zhao, Y. Zhou, D. Huang, G. Yue, L. Hu, N. Sun, Y. Wang, L. Y. S. Lee, C. Xu, K.-Y. Wong, D. Astruc and P. Zhao, *Coord. Chem. Rev.*, 2017, **352**, 306–327.

113 X. Zhang, J. Lei, D. Wu, X. Zhao, Y. Jing and Z. Zhou, *J. Mater. Chem. A*, 2016, **4**, 4871–4876.

114 M. Pogorielov, K. Smyrnova, S. Kyrylenko, O. Gogotsi, V. Zahorodna and A. Pogrebnjak, *Nanomaterials*, 2021, **11**, 3412.

115 L. Song, S. Zhu, L. Tong, W. Wang, C. Ouyang, F. Xu and Y. Wang, *Mater. Adv.*, 2021, **2**, 5622–5628.

116 R. Lotfi, M. Naguib, D. E. Yilmaz, J. Nanda and A. C. T. Van Duin, *J. Mater. Chem. A*, 2018, **6**, 12733–12743.

117 Y. Qin, Z. Wang, N. Liu, Y. Sun, D. Han, Y. Liu, L. Niu and Z. Kang, *Nanoscale*, 2018, **10**, 14000–14004.

118 J.-C. Lei, X. Zhang and Z. Zhou, *Front. Phys.*, 2015, **10**, 276–286.

119 K. Hantanasirisakul and Y. Gogotsi, *Adv. Mater.*, 2018, **30**, 1804779.

120 M. Khazaei, A. Ranjbar, M. Arai, T. Sasaki and S. Yunoki, *J. Mater. Chem. C*, 2017, **5**, 2488–2503.

121 J. Liu, S. Chen, J. He, R. Huang, L. Tao, Y. Zhao and Y. Yang, *Nanomaterials*, 2022, **12**, 2043.

122 F. Ai, C. Fu, G. Cheng, H. Zhang, Y. Feng, X. Yan and X. Zheng, *ACS Appl. Nano Mater.*, 2021, **4**, 8192–8199.

123 Q. Xu, L. Ding, Y. Wen, W. Yang, H. Zhou, X. Chen, J. Street, A. Zhou, W.-J. Ong and N. Li, *J. Mater. Chem. C*, 2018, **6**, 6360–6369.

124 A. S. Sharbirin, S. Roy, T. T. Tran, S. Akhtar, J. Singh, D. L. Duong and J. Kim, *J. Mater. Chem. C*, 2022, **10**, 6508–6514.

125 K. Hantanasirisakul and Y. Gogotsi, *Adv. Mater.*, 2018, **30**, 1804779.

126 B. Vénosová and F. Karlický, *Nanoscale Adv.*, 2023, **5**, 7067–7076.

127 M. Khazaei, M. Arai, T. Sasaki, C. Chung, N. S. Venkataramanan, M. Estili, Y. Sakka and Y. Kawazoe, *Adv. Funct. Mater.*, 2013, **23**, 2185–2192.

128 R. M. Ronchi, J. T. Arantes and S. F. Santos, *Ceram. Int.*, 2019, **45**, 18167–18188.

129 P. Chakraborty, T. Das and T. Saha-Dasgupta, in *Comprehensive Nanoscience and Nanotechnology*, Elsevier, 2019, pp. 319–330.

130 Z. Zeng, Y. Yan, J. Chen, P. Zan, Q. Tian and P. Chen, *Adv. Funct. Mater.*, 2019, **29**, 1806500.

131 R. M. Ronchi, J. T. Arantes and S. F. Santos, *Ceram. Int.*, 2019, **45**, 18167–18188.

132 K. Hantanasirisakul and Y. Gogotsi, *Adv. Mater.*, 2018, **30**, 1804779.

133 R. M. Ronchi, J. T. Arantes and S. F. Santos, *Ceram. Int.*, 2019, **45**, 18167–18188.

134 M. Khazaei, M. Arai, T. Sasaki, M. Estili and Y. Sakka, *Phys. Chem. Chem. Phys.*, 2014, **16**, 7841–7849.

135 R. Ramírez, A. Melillo, S. Osella, A. M. Asiri, H. Garcia and A. Primo, *Small Methods*, 2023, **7**, 2300063.

136 Y. Xu, X. Wang, W. L. Zhang, F. Lv and S. Guo, *Chem. Soc. Rev.*, 2018, **47**, 586–625.

137 S. Zhu, Y. Song, J. Wang, H. Wan, Y. Zhang, Y. Ning and B. Yang, *Nano Today*, 2017, **13**, 10–14.

138 Y. Cao, T. Wu, K. Zhang, X. Meng, W. Dai, D. Wang, H. Dong and X. Zhang, *ACS Nano*, 2019, **13**(2), 1499–1510.

139 R. Li, L. Zhang, L. Shi and P. Wang, *ACS Nano*, 2017, **11**, 3752–3759.

140 Z. Guo, J. Zhou, L. Zhu and Z. Sun, *J. Mater. Chem. A*, 2016, **4**, 11446–11452.

141 Q. Xu, L. Ding, Y. Wen, W. Yang, H. Zhou, X. Chen, J. Street, A. Zhou, W.-J. Ong and N. Li, *J. Mater. Chem. C*, 2018, **6**, 6360–6369.

142 Q. Guan, J. Ma, W. Yang, R. Zhang, X. Zhang, X. Dong, Y. Fan, L. Cai, Y. Cao, Y. Zhang, N. Li and Q. Xu, *Nanoscale*, 2019, **11**, 14123–14133.

143 S. Zhu, Y. Song, J. Wang, H. Wan, Y. Zhang, Y. Ning and B. Yang, *Nano Today*, 2017, **13**, 10–14.

144 H. Ding, S.-B. Yu, J.-S. Wei and H.-M. Xiong, *ACS Nano*, 2016, **10**, 484–491.

145 L. Zhang, L. Yin, C. Wang, N. Lun, Y. Qi and D. Xiang, *J. Phys. Chem. C*, 2010, **114**, 9651–9658.

146 G. Xu, Y. Niu, X. Yang, Z. Jin, Y. Wang, Y. Xu and H. Niu, *Adv. Opt. Mater.*, 2018, **6**, 1800951.

147 D. Huang, Y. Xie, D. Lu, Z. Wang, J. Wang, H. Yu and H. Zhang, *Adv. Mater.*, 2019, **31**, 1901117.

148 Z. Guo, X. Zhu, S. Wang, C. Lei, Y. Huang, Z. Nie and S. Yao, *Nanoscale*, 2018, **10**, 19579–19585.

149 Q. Xu, L. Ding, Y. Wen, W. Yang, H. Zhou, X. Chen, J. Street, A. Zhou, W.-J. Ong and N. Li, *J. Mater. Chem. C*, 2018, **6**, 6360–6369.

150 Y. Liu, W. Zhang and W. Zheng, *Nano-Micro Lett.*, 2022, **14**, 158.

151 Y. Qin, Z. Wang, N. Liu, Y. Sun, D. Han, Y. Liu, L. Niu and Z. Kang, *Nanoscale*, 2018, **10**, 14000–14004.

152 Y. Xu, J. Liu, C. Gao and E. Wang, *Electrochem. Commun.*, 2014, **48**, 151–154.

153 B. Shao, Z. Liu, G. Zeng, H. Wang, Q. Liang, Q. He, M. Cheng, C. Zhou, L. Jiang and B. Song, *J. Mater. Chem. A*, 2020, **8**, 7508–7535.

154 A. A. Alothman, M. R. Khan, M. D. Albaqami, S. Mohandoss, Z. A. Alothman, N. Ahmad and K. N. Alqahtani, *Nanomaterials*, 2023, **13**, 3026.

155 X. Yu, X. Cai, H. Cui, S.-W. Lee, X.-F. Yu and B. Liu, *Nanoscale*, 2017, **9**, 17859–17864.

156 P. Makuła, M. Pacia and W. Macyk, *J. Phys. Chem. Lett.*, 2018, **9**, 6814–6817.

157 D. J. Joshi, S. Jha, N. I. Malek, T. J. Park and S. K. Kailasa, *Microchim. Acta*, 2024, **191**, 621.

158 H. Yang, L. Wang, W. Ren, D. Fan, J. Wang and X. Zhang, *Microchem. J.*, 2025, **209**, 112791.

159 J. Mohammadi, A. Hheidari, S. Sardari, M. Nouri, S. Ebrahimi, A. Rahdar and E. Pishbin, *Biomed. Mater.*, 2024, **19**, 052004.

160 D. Huang, Y. Xie, D. Lu, Z. Wang, J. Wang, H. Yu and H. Zhang, *Adv. Mater.*, 2019, **31**, 1901117.

161 G. Xu, Y. Niu, X. Yang, Z. Jin, Y. Wang, Y. Xu and H. Niu, *Adv. Opt. Mater.*, 2018, **6**, 1800951.

162 X. Chen, X. Sun, W. Xu, G. Pan, D. Zhou, J. Zhu, H. Wang, X. Bai, B. Dong and H. Song, *Nanoscale*, 2018, **10**, 1111–1118.

163 B. Hu, J. Chen, Z. Gao, L. Chen, T. Cao, H. Li, Q. Yu, C. Wang and Z. Gan, *ACS Appl. Bio Mater.*, 2024, **7**, 4339–4351.

164 L. Chen, X. Dai, W. Feng and Y. Chen, *Acc. Mater. Res.*, 2022, **3**, 785–798.

165 W. Dai, H. Dong and X. Zhang, *Materials*, 2018, **11**, 1776.

166 T. R. Kyriakides, A. Raj, T. H. Tseng, H. Xiao, R. Nguyen, F. S. Mohammed, S. Halder, M. Xu, M. J. Wu, S. Bao and W. C. Sheu, *Biomed. Mater.*, 2021, **16**, 042005.

167 M. I. H. Protyai and A. Bin Rashid, *Heliyon*, 2024, **10**, e37030.

168 J. Serafin, B. Dziejarski, G. Oindo Achieng, X. Vendrell, S. Chaitoglou and R. Amade-Rovira, *J. Ind. Eng. Chem.*, 2025, **142**, 18–33.

169 L. Chen, X. Dai, W. Feng and Y. Chen, *Acc. Mater. Res.*, 2022, **3**, 785–798.

170 Y. Zhu, L. Feng, R. Zhao, B. Liu and P. Yang, *ACS Appl. Nano Mater.*, 2024, **7**, 2546–2574.

171 J. Huang, J. Su, Z. Hou, J. Li, Z. Li, Z. Zhu, S. Liu, Z. Yang, X. Yin and G. Yu, *Chem. Res. Toxicol.*, 2023, **36**, 347–359.

172 B. Singh, R. Bahadur, D. Rai and R. Srivastava, *Adv. Ther.*, 2024, **7**, 2300268.

173 T. Li, W. Qiang and B. Lei, *Nanoscale*, 2025, **17**, 4854–4891.

174 Y. Cai, T. Chai, W. Nguyen, J. Liu, E. Xiao, X. Ran, Y. Ran, D. Du, W. Chen and X. Chen, *Signal Transduction Targeted Ther.*, 2025, **10**, 115.

175 C. B. Wilson, *Br. Med. J.*, 1999, **319**, 1288–1288.

176 Y. Kim, Y. Jeon, M. Na, S.-J. Hwang and Y. Yoon, *Sensors*, 2024, **24**, 431.

177 S. Malik, K. Muhammad and Y. Waheed, *Molecules*, 2023, **28**, 6624.

178 N. Bardhan, *MRS Commun.*, 2022, **12**, 1119–1139.

179 I. Nandi, V. Patel, R. Srivastava and P. Chandra, *Microchem. J.*, 2024, **205**, 111360.

180 E. Ito, K. Iha, T. Yoshimura, K. Nakaishi and S. Watabe, in *Advances in Clinical Chemistry*, Elsevier, 2021, vol. 101, pp. 121–133.

181 P. Croft, D. G. Altman, J. J. Deeks, K. M. Dunn, A. D. Hay, H. Hemingway, L. LeResche, G. Peat, P. Perel, S. E. Petersen, R. D. Riley, I. Roberts, M. Sharpe, R. J. Stevens, D. A. Van Der Windt, M. Von Korff and A. Timmis, *BMC Med.*, 2015, **13**, 20.

182 M. B. Kulkarni, N. H. Ayachit and T. M. Aminabhavi, *Biosensors*, 2022, **12**, 543.

183 L. Mou, K. Mandal, M. M. Mecwan, A. L. Hernandez, S. Maity, S. Sharma, R. D. Herculano, S. Kawakita, V. Jucaud, M. R. Dokmeci and A. Khademhosseini, *Lab Chip*, 2022, **22**, 3801–3816.

184 Y. Gogotsi and B. Anasori, *ACS Nano*, 2019, **13**, 8491–8494.

185 J. Huang, Z. Li, Y. Mao and Z. Li, *Nano Select*, 2021, **2**, 1480–1508.

186 B. Shao, Z. Liu, G. Zeng, H. Wang, Q. Liang, Q. He, M. Cheng, C. Zhou, L. Jiang and B. Song, *J. Mater. Chem. A*, 2020, **8**, 7508–7535.

187 B. Vénosová and F. Karlický, *Nanoscale Adv.*, 2023, **5**, 7067–7076.

188 C. Mariani, S. Bogialli, F. Paolucci, P. Pastore, A. Zanut and G. Valenti, *Electrochim. Acta*, 2024, **489**, 144256.

189 P. Bertoncello and P. Ugo, *ChemElectroChem*, 2017, **4**, 1663–1676.

190 L. Gao and C. He, *Anal. Methods*, 2024, **16**, 1718–1735.

191 D. Liu, J. Cui, X. Xu, X. Deng and G. Nie, *Sens. Actuators, B*, 2023, **394**, 134397.

192 X. Gou, Z. Xing, C. Ma and J.-J. Zhu, *Chem. Biomed. Imaging*, 2023, **1**, 414–433.

193 M. Li, Z. Li, P. Wang and Q. Ma, *Biosens. Bioelectron.*, 2023, **228**, 115225.

194 D. Lu, X. Zhou, L. Lin, X. Zhang, Y. Chen and L. Feng, *J. Electroanal. Chem.*, 2024, **962**, 118285.

195 T. Wang, Y. Wang, Y. Zeng, X. Tian and X. Xu, *Food Chem.*, 2024, **460**, 140519.

196 J. Gu, X. Lu, G. Li, B. Shan, J. Liu, Y. Qu, H. Ye, K. Xi and H. Wu, *Chem. Eng. J.*, 2023, **467**, 143445.

197 S. D. Nehate, A. K. Saikumar, A. Prakash and K. B. Sundaram, *Mater. Today Adv.*, 2020, **8**, 100106.

198 K. James Singh, T. Ahmed, P. Gautam, A. S. Sadhu, D.-H. Lien, S.-C. Chen, Y.-L. Chueh and H.-C. Kuo, *Nanomaterials*, 2021, **11**, 1549.

199 L. Gao and C. He, *Anal. Methods*, 2024, **16**, 1718–1735.

200 A. M. Amani, L. Tayebi, E. Vafa, A. Jahanbin, M. Abbasi, A. Vaez, H. Kamyab, L. Gnanasekaran and S. Chelliapan, *Sens. Bio-Sens. Res.*, 2025, **47**, 100732.

201 Q. Lu, J. Wang, B. Li, C. Weng, X. Li, W. Yang, X. Yan, J. Hong, W. Zhu and X. Zhou, *Anal. Chem.*, 2020, **92**, 7770–7777.

202 Y. Bai, Y. He, M. Wang and G. Song, *Sens. Actuators, B*, 2022, **357**, 131410.

203 D. Gu, K. Andreev and M. E. Dupre, *China CDC Wkly*, 2021, **3**, 604–613.

204 N. Jain, I. Kourampi, T. P. Umar, Z. R. Almansoor, A. Anand, M. E. Ur Rehman, S. Jain and A. Reinis, *AIMS Public Health*, 2023, **10**, 849–866.

205 S. M. Mousavi, M. Y. Kalashgrani, M. Binazadeh, Y. Mazaheri, N. Omidifar, V. Rahmanian, M. Riazi, C. W. Lai, R. H. Althomali, M. M. Rahman, A. Gholami and W.-H. Chiang, *Mater. Today Chem.*, 2024, **38**, 102097.

206 S. Tang, K. Yuan and L. Chen, *Fundam. Res.*, 2022, **2**, 894–902.

207 S. Qiu, Y. Cai, H. Yao, C. Lin, Y. Xie, S. Tang and A. Zhang, *Signal Transduction Targeted Ther.*, 2023, **8**, 132.

208 H. Beck, M. Härter, B. Haß, C. Schmeck and L. Baerfacker, *Drug Discovery Today*, 2022, **27**, 1560–1574.

209 D. Bhatia, S. Paul, T. Acharjee and S. S. Ramachairy, *Sens. Int.*, 2024, **5**, 100257.

210 R. Kumari, D. S. Dkhar, S. Mahapatra, Divya, S. P. Singh and P. Chandra, *Biosensors*, 2022, **12**, 1062.

211 S. A. Mohammed, M. H. Kahissay and A. D. Hailu, *PLoS One*, 2021, **16**, e0259160.

212 R. Rajamanikandan, K. Sasikumar and H. Ju, *Anal. Chim. Acta*, 2024, **1322**, 343069.

213 G. Rajapriya, R. Sangubotla and J. Kim, *Korean J. Chem. Eng.*, 2024, **41**, 1805–1813.

214 D. Ren, X. Cheng, Q. Chen, G. Xu, F. Wei, J. Yang, J. Xu, L. Wang, Q. Hu and Y. Cen, *Microchem. J.*, 2023, **187**, 108397.

215 D. Huang, Y. Wu, F. Ai, X. Zhou and G. Zhu, *Sens. Actuators, B*, 2021, **342**, 130074.

216 M. Liu, Y. Bai, Y. He, J. Zhou, Y. Ge, J. Zhou and G. Song, *Microchim. Acta*, 2021, **188**, 15.

217 F. Yan, J. Sun, Y. Zang, Z. Sun, H. Zhang, J. Xu and X. Wang, *Dyes Pigm.*, 2021, **195**, 109720.

218 Q. Lu, J. Wang, B. Li, C. Weng, X. Li, W. Yang, X. Yan, J. Hong, W. Zhu and X. Zhou, *Anal. Chem.*, 2020, **92**, 7770–7777.

219 X. Zhou, J. Zhang, D. Huang, Y. Yi, K. Wu and G. Zhu, *Spectrochim. Acta, Part A*, 2023, **293**, 122484.

220 D. Pasalic, N. Marinkovic and L. Feher-Turkovic, *Biochem. Med.*, 2012, 63–75.

221 G. Ragab, M. Elshahaly and T. Bardin, *J. Adv. Res.*, 2017, **8**, 495–511.

222 M. Liu, Y. He, J. Zhou, Y. Ge, J. Zhou and G. Song, *Anal. Chim. Acta*, 2020, **1103**, 134–142.

223 S. Karimi and M. Amjadi, *Microchem. J.*, 2024, **207**, 112068.

224 C. Gaucher, A. Boudier, J. Bonetti, I. Clarot, P. Leroy and M. Parent, *Antioxidants*, 2018, 7, 62.

225 G. Wu, J. R. Lupton, N. D. Turner, Y.-Z. Fang and S. Yang, *J. Nutr.*, 2004, **134**, 489–492.

226 N. Ballatori, S. M. Krance, S. Notenboom, S. Shi, K. Tieu and C. L. Hammond, *Biol. Chem.*, 2009, **390**, 191–214.

227 W. Luo, H. Liu, X. Liu, L. Liu and W. Zhao, *Colloids Surf., B*, 2021, **201**, 111631.

228 H. Yang, L. Wang, W. Ren, D. Fan, J. Wang and X. Zhang, *Microchem. J.*, 2025, **209**, 112791.

229 A. T. Kessler and A. Raja, in *StatPearls*, StatPearls Publishing, Treasure Island, FL, 2025.

230 M. Holeček, *Nutrients*, 2020, **12**, 848.

231 J. W. Peterson, I. Boldogh, V. L. Popov, S. S. Saini and A. K. Chopra, *Lab. Invest.*, 1998, **78**, 523–534.

232 M. Singhal, M. Agrawal, K. Bhavna, N. K. Sethiya, S. Bhargava, K. S. Gondkar, K. Joshi, V. S. Rana, J. Sahoo and M. K. Arora, in *Antibiotics - Therapeutic Spectrum and Limitations*, Elsevier, 2023, pp. 155–165.

233 X. Dou, Q. Wu, S. Luo, J. Yang, B. Dong, L. Wang, H. Qu and L. Zheng, *Talanta*, 2024, **271**, 125702.

234 S. I. Polianciuc, A. E. Gurzău, B. Kiss, M. G. Ștefan and F. Loghin, *Med. Pharm. Rep.*, 2020, **93**(3), 231–240.

235 A. Shahid, M. A. Ali, S. Muzammil, B. Aslam, M. Shahid, M. Saqalein, M. S. H. Akash, A. Almatroudi, K. S. Allemailem and M. Khurshid, *Appl. Ecol. Environ. Res.*, 2021, **19**, 3959–3977.

236 Y. Bai, Y. He, Y. Wang and G. Song, *Microchim. Acta*, 2021, **188**, 401.

237 V. T. Nguyen, T. N. A. Nguyen, R. Doong and K.-K. Liu, *Microchem. J.*, 2025, **208**, 112427.

238 Y. Sun, X. Li, R. Chen, F. Liu and S. Wei, *Front. Nutr.*, 2022, **9**, 1039762.

239 M. Liu, J. Zhou, Y. He, Z. Cai, Y. Ge, J. Zhou and G. Song, *Microchim. Acta*, 2019, **186**, 770.

240 Z. Guo, X. Zhu, S. Wang, C. Lei, Y. Huang, Z. Nie and S. Yao, *Nanoscale*, 2018, **10**, 19579–19585.

241 Y. Nie, Z. Liang, P. Wang, Q. Ma and X. Su, *Anal. Chem.*, 2021, **93**, 17086–17093.

242 X. Jiang, H. Wang, Y. Shen, N. Hu and W. Shi, *Sens. Actuators, B*, 2022, **350**, 130891.

243 R. Chen, L. Kan, F. Duan, L. He, M. Wang, J. Cui, Z. Zhang and Z. Zhang, *Microchim. Acta*, 2021, **188**, 316.

244 M. Ensenyat-Mendez, P. Llinàs-Arias, J. I. J. Orozco, S. Íñiguez-Muñoz, M. P. Salomon, B. Sesé, M. L. DiNome and D. M. Marzese, *Front. Oncol.*, 2021, **11**, 681476.

245 K. Aysola, A. Desai, C. Welch, J. Xu, Y. Qin, V. Reddy, R. Matthews, C. Owens, J. Okoli, D. J. Beech, C. J. Piyathilake, S. P. Reddy and V. N. Rao, *Hereditary Genet.*, 2013, (Suppl 2), DOI: 10.4172/2161-1041.S2-001.

246 A. Mandapati and K. E. Lukong, *J. Cancer Res. Clin. Oncol.*, 2023, **149**, 3701–3719.

247 Z. Li, Z. Wang, Y. Nie, P. Wang and Q. Ma, *Chem. Eng. J.*, 2022, **448**, 137636.

248 X. Xi, J. Wang, Y. Qin, W. Huang, Y. You and J. Zhan, *Cell Death Dis.*, 2022, **13**, 708.

249 W. Chen, Z. Zhang, S. Zhang, P. Zhu, J. K.-S. Ko and K. K.-L. Yung, *Int. J. Mol. Sci.*, 2021, **22**, 6567.

250 M. Yousefi, S. Dehghani, R. Nosrati, H. Zare, M. Evazalipour, J. Mosafer, B. S. Tehrani, A. Pasdar, A. Mokhtarzadeh and M. Ramezani, *Biosens. Bioelectron.*, 2019, **130**, 1–19.

251 N. K. Bernstein, R. S. Williams, M. L. Rakovszky, D. Cui, R. Green, F. Karimi-Busheri, R. S. Mani, S. Galicia, C. A. Koch, C. E. Cass, D. Durocher, M. Weinfeld and J. N. M. Glover, *Mol. Cell*, 2005, **17**, 657–670.

252 M. Weinfeld, R. S. Mani, I. Abdou, R. D. Aceytuno and J. N. M. Glover, *Trends Biochem. Sci.*, 2011, **36**, 262–271.

253 L. C. Dumitrache and P. J. McKinnon, *Mech. Ageing Dev.*, 2017, **161**, 121–129.

254 V. Tiwari and D. M. Wilson, *Am. J. Hum. Genet.*, 2019, **105**, 237–257.

255 H. Zhang, L. Wang, T. Zhuang, Z. Wei, J. Xia and Z. Wang, *Anal. Bioanal. Chem.*, 2022, **414**, 6753–6760.

256 K. Makris, C. Mousa and E. Cavalier, *Calcif. Tissue Int.*, 2022, **112**, 233–242.

257 J. H. Wang, K. Wang, B. Bartling and C.-C. Liu, *Sensors*, 2009, **9**, 8709–8721.

258 M. A. Kalas, L. Chavez, M. Leon, P. T. Taweesedt and S. Surani, *World J. Hepatol.*, 2021, **13**, 1688–1698.

259 L. M. Demers, L. Costa and A. Lipton, *Cancer*, 2000, **88**, 2919–2926.

260 Z. Guo, X. Zhu, S. Wang, C. Lei, Y. Huang, Z. Nie and S. Yao, *Nanoscale*, 2018, **10**, 19579–19585.

261 S. S. Shetty, D. D. , H. S. , S. Sonkusare, P. B. Naik, S. Kumari N and H. Madhyastha, *Heliyon*, 2023, **9**, e19496.

262 Vandana, M. Priyadarshanee, U. Mahto and S. Das, in *Microbial Biodegradation and Bioremediation*, Elsevier, 2022, pp. 33–53.

263 M. Tudi, H. Daniel Ruan, L. Wang, J. Lyu, R. Sadler, D. Connell, C. Chu and D. T. Phung, *Int. J. Environ. Res. Public Health*, 2021, **18**, 1112.

264 J. J. Steffan, E. C. Brevik, L. C. Burgess and A. Cerdà, *Eur. J. Soil Sci.*, 2018, **69**, 159–171.

265 I. Manisalidis, E. Stavropoulou, A. Stavropoulos and E. Bezirtzoglou, *Front. Public Health*, 2020, **8**, 14.

266 F. H. M. Tang, M. Lenzen, A. McBratney and F. Maggi, *Nat. Geosci.*, 2021, **14**, 206–210.

267 P. B. Tchounwou, C. G. Yedjou, A. K. Patlolla and D. J. Sutton, in *Molecular, Clinical and Environmental Toxicology*, ed. A. Luch, Springer Basel, Basel, 2012, vol. 101, pp. 133–164.

268 R. Teschke, *Int. J. Mol. Sci.*, 2024, **25**, 6662.

269 M. Moustakas, *Materials*, 2021, **14**, 549.

270 K. Peters, S. Staehlke, H. Rebl, A. Jonitz-Heincke and O. Hahn, *Int. J. Mol. Sci.*, 2024, **25**, 10127.

271 F. Bernheim, *Enzymologia*, 1954, **16**, 351–354.

272 A. L. Lehninger, *Physiol. Rev.*, 1950, **30**, 393–429.

273 S. Zhang, Z. Qi and Y. Li, *Ceram. Int.*, 2022, **48**, 21118–21124.

274 Q. Guan, J. Ma, W. Yang, R. Zhang, X. Zhang, X. Dong, Y. Fan, L. Cai, Y. Cao, Y. Zhang, N. Li and Q. Xu, *Nanoscale*, 2019, **11**, 14123–14133.

275 X. Wang, X. Zhang, H. Cao and Y. Huang, *J. Mater. Chem. B*, 2020, **8**, 10837–10844.

276 G. Cai, Z. Yu, P. Tong and D. Tang, *Nanoscale*, 2019, **11**, 15659–15667.

277 J. Yang, L. Chen, J. Qi, F. Luo, L. Li, H. Wu, F. Cao and J. Gu, *Food Chem.*, 2024, **430**, 137007.

278 P. Jin, P. Wan, C. Zhang, X. Li, Y. Wang, J. Luo and K. Li, *Anal. Chim. Acta*, 2024, **1303**, 342517.

279 Nikkey, S. Swami, N. Sharma and A. Saini, *RSC Adv.*, 2024, **14**, 18907–18941.

280 H. Shuai, C. Xiang, L. Qian, F. Bin, L. Xiaohui, D. Jipeng, Z. Chang, L. Jiahui and Z. Wenbin, *Dyes Pigm.*, 2021, **187**, 109125.

281 W. F. Fitzgerald, D. R. Engstrom, R. P. Mason and E. A. Nater, *Environ. Sci. Technol.*, 1998, **32**, 1–7.

282 World Health Organization, *Guidelines for drinking-water quality [electronic resource]: incorporating 1st and 2nd addenda, Vol.1, recommendations*, World Health Organization, Geneva, 3rd edn, 2008.

283 M. Jaishankar, T. Tseten, N. Anbalagan, B. B. Mathew and K. N. Beeregowda, *Interdiscip. Toxicol.*, 2014, **7**, 60–72.

284 Z. Emami and R. Mohammad-Rezaei, *J. Mater. Sci.: Mater. Electron.*, 2024, **35**, 2113.

285 H. Tapiero, D. M. Townsend and K. D. Tew, *Biomed. Pharmacother.*, 2003, **57**, 386–398.

286 Z. Shabbir, A. Sardar, A. Shabbir, G. Abbas, S. Shamshad, S. Khalid, Natasha, G. Murtaza, C. Dumat and M. Shahid, *Chemosphere*, 2020, **259**, 127436.

287 S. Mitra, A. J. Chakraborty, A. M. Tareq, T. B. Emran, F. Nainu, A. Khusro, A. M. Idris, M. U. Khandaker, H. Osman, F. A. Alhumaydhi and J. Simal-Gandara, *J. King Saud Univ., Sci.*, 2022, **34**, 101865.

288 A. C. Ross, *Modern nutrition in health and disease*, LWW, 2012.

289 M. Bost, S. Houdart, M. Oberli, E. Kalonji, J.-F. Huneau and I. Margaritis, *J. Trace Elem. Med. Biol.*, 2016, **35**, 107–115.

290 M. J. Morales-Cruz, D. MejiasMorales, P. Hunsaker, E. Butler and M. Tassone, *Cureus*, 2023, **15**(6), DOI: **10.7759/cureus.40103**.

291 P. Chugh and Y. Lhamo, *Indian J. Pharm. Sci.*, 2012, **74**, 469.

292 V. I. Gavrilov, *Acta Virol.*, 1975, **19**, 510.

293 Z. Wang, Y. Zhu, Y. Wu, W. Ding and X. Li, *Nanoscale*, 2022, **14**, 9498–9506.

294 G. Ziwa, R. Crane and K. A. Hudson-Edwards, *Minerals*, 2020, **11**, 22.

295 S. Mahey, R. Kumar, M. Sharma, V. Kumar and R. Bhardwaj, *SN Appl. Sci.*, 2020, **2**, 1279.

296 L. Leyssens, B. Vinck, C. Van Der Straeten, F. Wuyts and L. Maes, *Toxicology*, 2017, **387**, 43–56.

297 X. Wang, X. Zhang, H. Cao and Y. Huang, *Microchem. J.*, 2022, **180**, 107629.

298 E. J. Yang, O. S. Jeon, J. U. Yang, M. K. Shin, Y. J. Yoo and S. Y. Park, *Carbon*, 2020, **167**, 863–869.

299 R. Cammack, C. L. Joannou, X.-Y. Cui, C. Torres Martinez, S. R. Maraj and M. N. Hughes, *Biochim. Biophys. Acta, Bioenerg.*, 1999, **1411**, 475–488.

300 Z. Kalaycıoğlu and F. B. Erim, *J. Agric. Food Chem.*, 2019, **67**, 7205–7222.

301 IARC Working Group on the Evaluation of Carcinogenic Risks to Humans and International Agency for Research on Cancer, *Ingested nitrate and nitrite, and cyanobacterial peptide toxins*, International Agency for Research on Cancer, Lyon, France Geneva, 2010.

302 Y. Bai, Y. He, M. Wang and G. Song, *Sens. Actuators, B*, 2022, **357**, 131410.

303 A. Y. El-Moghazy, E. A. Soliman, H. Z. Ibrahim, J.-L. Marty, G. Istamboulie and T. Noguer, *Talanta*, 2016, **155**, 258–264.

304 M. M. Sibanda, W. W. Focke, F. J. Labuschagne, L. Moyo, N. S. Nhlapo, A. Maity, H. Muiambo, P. Massinga, N. A. Crowther, M. Coetzee and G. W. Brindley, *Malar. J.*, 2011, **10**, 307.

305 M. B. Colovic, D. Z. Krstic, T. D. Lazarevic-Pasti, A. M. Bondzic and V. M. Vasic, *CN*, 2013, **11**, 315–335.

306 World Health Organization, 2008, WHO/HSE/AMR/08.03/15.

307 Z. Ding, X. Zhan, Y. Zhang, K. Chu and Y. Guo, *Microchem. J.*, 2024, **207**, 111951.